



POLITECNICO
MILANO 1863

School of Industrial and Information Engineering
Master of Science in Engineering Physics

**Light sheet microscopy with
adaptive optical elements:
implementation, control and
characterization**

Candidate: **Gianmaria Calisesi**

Student ID: 836813

Thesis advisor: **Prof. Andrea Bassi**

Academic year 2016/2017

"It is only in the microscope that our life looks so big. It is an indivisible point, drawn out and magnified by the powerful lenses of Time and Space."

Arthur Schopenhauer

Abstract

One of the main challenges in optical imaging is the development of microscopy techniques able to observe fast dynamic processes, over a large field of view, at high spatio-temporal resolution and over a long period of time. A microscopy technique that exhibits these peculiarities is Light Sheet Fluorescence Microscopy (LSFM). In this technique a fluorescent sample is illuminated by a thin “light sheet” that can be created using a laser beam focused by cylindrical lens, and fluorescence light emitted by the light sheet is collected by an objective lens in the direction perpendicular to the illumination axis. A 3D reconstruction of the sample can be achieved by translating the sample through the light sheet in the imaging chamber.

The goal of this thesis work was to develop a light sheet microscope that could be used to study mm-scaled objects, at high resolution, avoiding the need to translate the sample in the imaging chamber.

In order to achieve these goals, first, a new microscope was constructed, incorporating a galvo-scanner to move the light sheet within the sample and an adaptive (electrically tunable) lens to keep the image in focus on the detector.

Second, a software to control the instrument was fully developed (using Labview code), able to trigger the scan of the galvo, the tunable lens and camera acquisition simultaneously. A state machine was implemented to run the software and to provide the user with the ability to rapidly calibrate the setup and acquire a full stack of images during the sample scan.

Finally, the system was validated using different reference targets, the specifications of the system were assessed and measurements of various fluorescent specimens were performed, including *Arabidopsis thaliana* roots and *Danio rerio* (zebrafish), expressing fluorescent proteins in different cellular compartments.

Sommario

Una delle principali sfide nell'imaging ottico è lo sviluppo di tecniche di microscopia in grado di osservare processi dinamici veloci, in un ampio campo visivo, ad alta risoluzione temporale e per un lungo periodo di tempo. Una tecnica di microscopia che mostra queste peculiarità è la microscopia di fluorescenza a foglio di luce (in inglese LSFM). In questa tecnica, un campione fluorescente viene illuminato da un sottile "foglio di luce", che può essere prodotto facendo focalizzare un fascio laser collimato da una lente cilindrica, mentre il segnale di fluorescenza emesso dalla zona illuminata dal foglio di luce viene raccolto da un obiettivo ottico in direzione perpendicolare all'asse di illuminazione. Una ricostruzione 3D del campione può essere quindi ottenuta traslando il campione stesso attraverso il foglio di luce nella camera del campione.

L'obiettivo di questa tesi è quello di sviluppare un microscopio a foglio di luce che può essere utilizzato per studiare oggetti su scala millimetrica, ad alta risoluzione, evitando di traslare il campione nella camera del microscopio.

Per raggiungere questi obiettivi, in primo luogo, è stato costruito un nuovo apparato, incorporando uno specchio galvanometrico per spostare il foglio di luce all'interno del campione e una lente adattativa (tunabile elettricamente), per mantenere l'immagine a fuoco sul rivelatore.

In secondo luogo, un software per controllare lo strumento è stato completamente sviluppato (in ambiente Labview), in grado di attivare contemporaneamente la scansione dello specchio motorizzato, della lente tunabile e l'acquisizione del sensore. Il software è stato implementato come una macchina a stati per fornire all'utente la possibilità di calibrare rapidamente il setup e acquisire una stack completa di immagini durante la scansione del campione.

Infine, il sistema è stato avvalorato utilizzando diversi target ottici di riferimento, sono state quindi valutate le specifiche del sistema e sono state eseguite misure

su diversi campioni fluorescenti, tra cui radici *Arabidopsis thaliana* e *Danio rerio* (zebrafish), che esprimono proteine fluorescenti in diversi compartimenti cellulari.

Acknowledgements

Finally I am here and that is only thanks to all of the people I came across during my short but yet intense life. Honestly I met so many people worth to be mentioned that it is hard for me to choose where to start. First of all I would like to thanks my supervisor, Andrea, for all of the time I made him waste on explaining me optics things; Gianluca as well, that together with Alessia helped me a lot in this final work of my Master.

In second place my friends from Romagna, ch'i burdel ad Furle', Strocchino, Charnardi, Dido, Ivan, Carolina, Gram, Versa, Nicola "il paccaro" e Marco; ch'i burdel dla Frata, Elia, Ion, Varo and many other, you really helped me going through hard times and the boredom of my everyday life.

And then my handsome engineering friends, with which classes weren't so bad after all: Michele and Aurelio, Alberto, Riccardo, Stefano, Beppe, Stella, Mavio, Giaggia, Perri, Giorgio, Gazzi, Ruschino, Carlo and Thunder, you are wonderful and I love you more than an analytic solution of a partial derivative equation.

Then the erasmus, an experience that deprived me of much, but gave me more: my flatmates Sebastian, Boris "the nazi ginger", Mia and Ericcu; all of the amazing people from MDR, Gianluca, Alessio, Ana and Francisco; and then my teammate Maurizio, Damiano, Jaime, Matte, Germa and all of the people I don't even recall the name of, you made it something unforgettable that I will carry in my heart for the rest of my life.

Then I would like to thank my fantastic family from my amazing parents, brothers, uncles, grandparents (nonni vi voglio tanto bene), cousins, without which I wouldn't be here now, graduating at Politecnico di Milano for the second time; even if there were some moments where we haven't really got along, you will always have my love.

Finally, it is with my heart thank I would like to thank Edoardo, Enrico, Federica, Martina, Michele and Tudor, you are more than brothers and sisters to me, you really are amazing and I know it doesn't matter in what part of the world our paths will take us to, I can always count on you. I love you more than a free Duvel pint in front of Juventus winning the champions league.

And last, thank You, God, I don't have any clue if you are there, if you are ignoring us or you are just a flawless try to justify our worst actions, but if you exists then thank You for surrounding me with these amazing people.

Vale

Contents

Abstract	iii
Sommario	iv
Acknowledgements	vii
List of Figures	xi
1 Fundamentals	1
1.1 Fluorescence	1
1.1.1 Two-level Molecule: Rate Equations	2
1.1.2 Three-level Molecule: Triplet State	5
1.1.3 Photobleaching	7
1.2 Optics and Theory	8
1.2.1 Fundamentals	8
1.2.2 Optical functions	11
1.2.3 Circular Pupil	15
1.2.4 Frequency Support	18
1.3 Selective Plane Illumination Microscopy	21
1.3.1 Introduction	21
1.3.2 Working Principles	22
1.3.3 Optical and speed performances	22
1.3.4 Light-sheet engineering	25
1.3.5 Fast volume imaging	27
2 Optical design and implementation	30
2.1 Optical Design	30
2.1.1 Bright Field Illumination	30
2.1.2 Köhler Illumination	31
2.1.3 Light Sheet Illumination	34
2.1.4 Detection	37
2.1.5 Numerical Aperture and Depth of field	38
2.2 Implementation of the Experimental Setup	40

2.3	System imaging and optical characteristics	45
2.3.1	Scanning range	45
2.3.2	Specifications of the developed system	49
3	Software and Acquisition	53
3.1	Introduction	53
3.2	Software Environment	53
3.2.1	Device interface	54
3.2.2	Code Compiling	55
3.3	Tools	55
3.3.1	Electotrunable Lens: Optotune EL-16-40-TC	55
3.3.2	Galvanometric Mirror: Thorlabs GVS001	56
3.3.3	DAQ: National Instrument USB 6221	58
3.3.4	Electron Multiplier CCD: Luca-r	58
3.4	Software	60
3.4.1	Initialization states and wait for command	62
3.4.1.1	CRC algorithm	67
3.4.2	Initialization and Calibration	70
3.4.2.1	ETL Analog	71
3.4.2.2	Voltage Calibration	73
3.4.2.3	Current Calibration	75
3.4.2.4	ETL get Temperature and Restart	76
3.4.3	Scan and Imaging	77
3.4.3.1	Volume scan	77
3.4.3.2	Static Acquisition	79
3.5	State Machine full Analysis	79
3.5.1	Classification	79
3.5.2	Encoding	80
4	Calibration and Measurements	82
4.1	Sampling Theory	83
4.2	System Calibration Tools	84
4.3	System Calibration: Positioning and Stability test	86
4.4	System Calibration: Magnification and Scanning range	89
4.5	In vivo Measurements	90
4.5.1	Optical Sectioning	91
4.5.2	Axial Resolution	96
4.6	Conclusions	98

List of Figures

1.1	Two level system energy diagram and Stokes shift	2
1.2	Three-level molecule energy diagram.	5
1.3	Energy diagram for a three-level system with photobleaching	7
1.4	Numerical Aperture of an optical system	9
1.5	Imaging by a lens of focal f	12
1.6	4f configuration	13
1.7	Coordinate system used for OTF definition.	15
1.8	Basic imaging functions for a pupil of circular aperture [1]	18
1.9	Frequency Support for the Coherent Spread Function from energy momentum relation	19
1.10	3D Frequency Support of a circular pupil OTF within the Fresnel approximation	21
1.11	Epifluorescence and Light Sheet Fluorescence Microscopy typical illumination and detection setup	23
1.12	Light focusing in confocal microscopy and light sheet microscopy	24
1.13	Gaussian beam width $w(z)$ as a function of the distance z along the beam profile.	24
1.14	Depth of Field extension with adaptive lenses and difference of refractive indices	28
2.1	Köhler illumination standard setup	32
2.2	Throughput calculation for a two apertures system	33
2.3	Throughput calculation for a system made by two apertures at a distance $2f$, with a lens of focal f in the center.	34
2.4	Kohler illumination setup implemented.	35
2.5	Light sheet generated in a typical SPIM setup	37
2.6	General detection scheme for fluorescence microscopy.	38
2.7	Depth of field variation at different numerical apertures.	39
2.8	Depth of field and depth of focus variation.	39
2.9	General view of a telecentric system.	41
2.10	Whole SPIM setup, including bright field illumination.	41
2.11	Top and side view of the light ray bundle in the illumination path.	42
2.12	SPIM setup implementation.	42
2.13	Vertical subsystem.	43
2.14	Detection schema	47
2.15	f-theta system.	52

3.1	Lens driver without its cage.	56
3.2	Galvanometric mirror driver without its cage.	57
3.3	DAQ working scheme.	58
3.4	Software User Interface.	60
3.5	Machine state diagram.	61
3.6	DAQ initialisation state	62
3.7	Electrotunable Lens initialization state.	63
3.8	Write and read function. This sub VI allows communication with the lens driver.	65
3.9	Different cases depending on the input command.	66
3.10	Six Different cases depending on the input command.	66
3.11	CRC checksum in Labview, with overlapped block diagram and user interface.	68
3.12	CRC checksum XOR circuit implementation for a polynomial divi- sor of $1 + x + x^2 + x^8$	68
3.13	Set Current sub VI.	71
3.14	Case structure for different inputs.	72
3.15	Block diagram of the state "ETL analog".	73
3.16	Block diagram of the state "Voltage Calibration".	74
3.17	Block diagram of the state "Calibration".	75
3.18	Block diagram of the state "ETL get Temperature and Restart".	76
3.19	Block diagram of the state "Volume Scan".	77
3.20	"Volume Scan" state particular.	77
3.21	Block diagram particular of the state "Volume Scan" regarding the parameters retrieval for the generation of both signals.	78
3.22	Block diagram particular of the state "Volume Scan" regarding the delay mechanism between the generation of the analog signals and the digital trigger to be sent to the EMCCD.	79
3.23	Block diagram of the state "Static Acquisition".	79
3.24	Complete State Transition Diagram.	80
3.25	Binary state encoding	80
3.26	Output Table with state encoding	81
3.27	Moore state transition with state encoding.	81
4.1	Image acquisition onto a CCD sensor	83
4.2	Image of two point sources onto a pixelated sensor.	84
4.3	USAF-1951 resolution target.	85
4.4	Micrometric ruler.	86
4.5	Magnification test.	87
4.6	Stability test for the electrotunable optical power in time.	88
4.7	Micrometer at different distances.	89
4.8	Zebrafish head stack.	92
4.10	Zebrafish tail single plane.	93
4.11	Zebrafish tail stack.	94
4.12	Zebrafish head maximum intensity projection.	95

4.13 Zebrafish tail maximum intensity projection.	95
4.14 Arabidopsis Thaliana stack.	97
4.15 Orthogonal projection of the bust of an Arabidopsis Thaliana.	98

To all those who love me

Chapter 1

Fundamentals

1.1 Fluorescence

It is called fluorescence the emission of light by a molecule that has absorbed electromagnetic radiation. In the vast majority of cases, the emitted light has longer wavelength, therefore lower energy, than the absorbed radiation. In order to describe this process in the simplest way, we first consider a two level fluorescent molecule. When a wave is impinging on the system, the energy absorption rate is determined by a namesake cross-section in the following way:

$$W_{abs} = \sigma_{abs} I_i \quad (1.1)$$

where I_i is the light intensity and σ_{abs} is function of the radiation wavelength. After the energy absorption, not all of it is then released as fluorescent radiation but only a fraction according to the molecule radiative quantum yield q_r . As for the absorption process, so for the fluorescence emission we can write the relation between the emitted energy rate, the fluorescence cross-section and the illumination intensity:

$$W_f = \sigma_f I_i \quad (1.2)$$

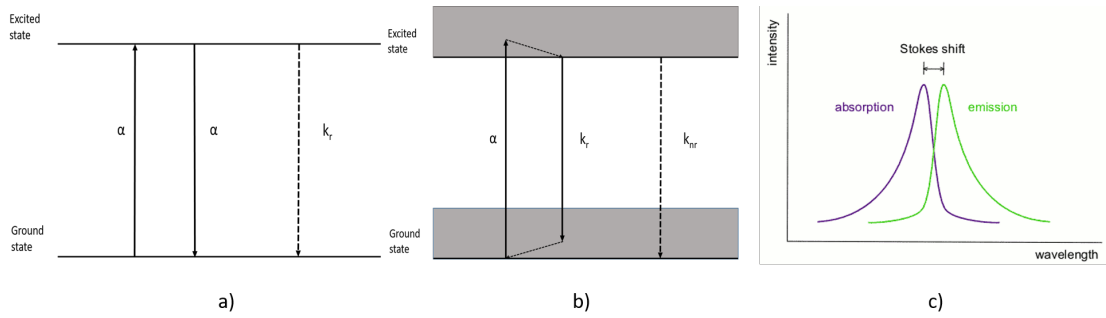


FIGURE 1.1: a) Two level system stimulated and spontaneous emission. b) Two level system exhibiting non radiative decay and Stokes shift. c) Red shift in fluorescent molecules.

We can now relate 1.1 to 1.2 through the quantum yield of the process:

$$W_f = \sigma_f I_i = q_r \sigma_{abs} I_i \quad (1.3)$$

So as it is suggested by eq. 1.3, the fluorescence power should scale linearly with illumination intensity, which is true only for low light intensities; therefore a description that takes into account the internal dynamics of a fluorescent molecules is needed.

1.1.1 Two-level Molecule: Rate Equations

The simplest way of modelling a fluorescent molecule is thinking of it as a two level-system consisting of a ground state g and an excited state e , with $E(e) - E(g) = \Delta E$ the two levels energy difference, with $\Delta E \gg k_B T_{room}$ in order to ensure that at room temperature the molecule for sure resides in the ground state. When a molecule in the ground state is perturbed by an electromagnetic radiation of energy $h\nu$, with h being the Planck's constant and ν the radiation frequency, iff $\Delta E = h\nu$ the molecule can be promoted to the excited state by absorption of a photon. Once in the e state, the molecule can then relax back to its former state by emission of a photon of same energy as the one absorbed.

Let us now consider the time varying probability functions of finding a molecule in either its ground or excited state, $g(t)$ and $e(t)$ respectively. It must hold, by

conservation of probability that

$$g(t) + e(t) = 1. \quad (1.4)$$

According to Einstein's equations [2] we can write the rate equations for the previous probabilities

$$\frac{dg(t)}{dx} = -\frac{de(t)}{dx} = -\alpha(g(t) - e(t)) + k_r e(t) \quad (1.5)$$

where $\alpha = \sigma_{abs} \frac{I_i}{h\nu}$ corresponds to the energy absorption rate given that the molecule is in its ground state and k_r is the so called radiative decay constant. While the excitation rate is simply given by the parameter α , the rate constant for the decay back to the ground state involves two decay channels with different rates : α and k_r . the first of these parameters depends on the illumination intensity and is referred to as stimulated; the latter, which is not dependent on the illumination intensity, is referred to as spontaneous. This radiative decay is what is called fluorescence.

A molecule behaving as a perfect two level system is an oversimplification. A real molecule in solution in fact possesses many vibrational and rotational sublevels that spread the electronic energy level into a multilevel structured band. Therefore, a molecule promoted from a ground energy state to an excited state is possible with an impinging radiation of energy spread over an extended energy range, with an efficiency characterized by σ_{abs} , that is as said before strongly dependent on the radiation wavelength. Once promoted, the molecule relaxes very quickly to the bottom of the excited state band due to collisions with the environment; usually this relaxation is so rapid (10^{-15} seconds) that there is no possibility for stimulated emission to happen [3].

We mentioned before that the molecular environment plays some role in molecule relaxation: in fact it introduces another decay channel to the ground state band [4]. This new decay channel, unlike the one we have treated so far, it is nonradiative and it is characterized by the rate k_{nr} . Keeping this in mind and considering $g(t)$

and $e(t)$ as instantaneous probability of finding a molecule in the ground or excited band respectively, then eq. 1.5 becomes

$$\frac{dg(t)}{dx} = -\frac{de(t)}{dx} = -\alpha g(t) + (k_r + k_{nr})e(t) \quad (1.6)$$

which is still satisfying the conservation of probability. The difference with eq. 1.5 is that now the excitation energy differs from the emission energy. The energy balance is lost due to the heat exchange with the molecular environment. This loss of energy is translated in a red shift of the fluorescence spectrum with respect to the absorption spectrum, known as Stoke shift. This shift turns out to be convenient in imaging applications since one can easily separate the two light component by the simple mean of spectral filtering.

Since we have introduced a non radiative decay channel, what is called quantum yield is now defined as

$$q_r = \frac{k_r}{k_r + k_{nr}} \quad (1.7)$$

giving the probability of radiative emission and therefore a fluorescent transition. We can now define a new quantity named *radiativelifetime*, which corresponds to the average lifetime of a molecule in the excited state.

$$\tau_e = \frac{1}{k_r + k_{nr}}. \quad (1.8)$$

From 1.6 the molecule is found in its excited state at $t = 0$, while for $t \geq 0$ the probability for it to be still in the excited state is given a Poissonian probability distribution $e^{-\frac{t}{\tau_e}}$ [1]. Keeping the excitation rate α constant with time, then the steady state solution of 1.6 is

$$\langle e \rangle = \frac{\alpha}{\alpha + k_r + k_{nr}} = \frac{\alpha\tau_e}{1 + \alpha\tau_e}, \quad (1.9)$$

from which we can easily derive the steady-state emission rate after the molecule is illuminated with radiation at frequency ν_f

$$\frac{W_f}{h\nu_f} = k_r \langle e \rangle. \quad (1.10)$$

Both quantities of 1.10 consist of a number of photons per second.

Let us now compare 1.2 to 1.10, the latter is more precise than the first since it also takes into account the red shift. Writing $\alpha = \alpha_{abs} \frac{I_i}{h\nu_i}$, with the subscript i standing for illumination, given the condition $\alpha \ll k_r + k_{nr}$ i.e. low illumination intensity, 1.2 becomes

$$W_f = \left(\frac{\nu_f}{\nu_i}\right) q_r \sigma_{abs} I_i = \sigma_f I_i. \quad (1.11)$$

Finally, it is worth mentioning that 1.10 includes the possibility of a non linear relation between W_f and I_i therefore in the high illumination intensity limit; so that for $\alpha \gg k_r + k_{nr}$, w_f tends to $h\nu_f k_r$ instead of being unbounded.

1.1.2 Three-level Molecule: Triplet State

A first step towards real molecules energy dynamics consist in introducing an intermediate state band, called triplet state. This triplet state is most likely to be not luminous but gives the molecule an alternative path to relax from the excited state as shown in Fig. 1.2. The *isc* subscript stands for intersystem crossing, indicating the transition from the excited state, to a level of lower energy (the triplet state) which is not the ground state. Thanks to Quantum mechanics one can derive the probability of intersystem transition, probability that happens to be quite small, usually less than one percent.

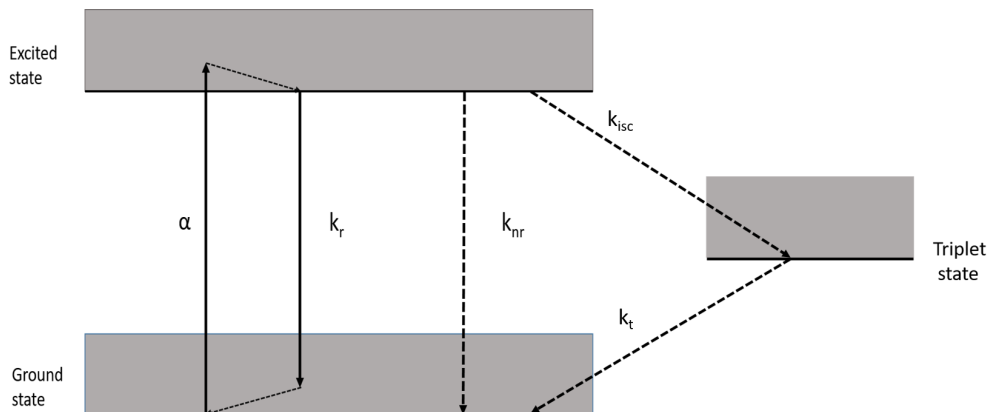


FIGURE 1.2: Three-level molecule energy diagram.

Nevertheless, despite such a low probability, the triplet state can critically affect fluorescence imaging performances.

How does this triplet state modify the transition dynamics in between the energy level of a molecule?

$$\frac{d}{dt} \begin{pmatrix} g \\ e \\ t \end{pmatrix} = \begin{pmatrix} -\alpha & k_r + k_{nr} & kt \\ \alpha & -(k_r + k_{nr} + k_{isc}) & 0 \\ 0 & k_{isc} & -k_t \end{pmatrix} \begin{pmatrix} g \\ e \\ t \end{pmatrix} = \mathcal{M} \begin{pmatrix} g \\ e \\ t \end{pmatrix} \quad (1.12)$$

with t being the instantaneous probability of finding a molecule in the triplet state, k_{isc} being the intersystem crossing rate constant, and k_t the triplet state decay rate constant. The fact that we are dealing with a molecule that can reside in only one of the three bands involved is reflected in $\text{Det}[\mathcal{M}] = 0$.

Similarly to what we have done for the two-level system, we can define a new quantum yield

$$q_r = \frac{k_r}{k_r + k_{nr} + k_{isc}}, \quad (1.13)$$

a new lifetime

$$\tau_e = \frac{1}{k_r + k_{nr} + k_{isc}}, \quad (1.14)$$

an intersystem crossing quantum yield parameter

$$q_{isc} = \frac{k_{isc}}{k_r + k_{nr} + k_{isc}}, \quad (1.15)$$

and a triplet state lifetime

$$\tau_t = \frac{1}{k_t}. \quad (1.16)$$

From what has been stated above, it follows that the more infrequent the transition from the excited to the triplet state, the longer the molecule remains trapped in the t state and therefore at low excitation rates (e.g. $\alpha \ll k_t$, the fluorescence intensity reduction caused by intersystem crossing is quite negligible; however, at very high excitation rates, the maximum fluorescence reduction factor is $\langle e \rangle / (\langle e \rangle + \langle t \rangle)$.

Most likely, the decay of a molecule from the triplet state to the ground state is nonradiative, in the rare case where it produces light, the radiation emitted takes the name of *phosphorescence*. It follows that a first difference between

fluorescence and *phosphorescence* is the state from which radiation is emitted: the excited state for the first, the triplet state for the latter.

1.1.3 Photobleaching

Once a molecule is removed from its singlet manifold due to intersystem crossing, it is not able to radiatively emit. However this removal from the excited singlet state is not permanent and it only lasts on average the duration of the triplet state lifetime given by eq. 1.16. When one wants to exploit imaging using fluorescence, aside intersystem crossing he also has to face another, tedious problem which permanently removes the molecule from its singlet manifold: photobleaching. The physical explanation of photobleaching varies from molecule to molecule and it is strongly dependent on the molecular environment. We take into account the pos-

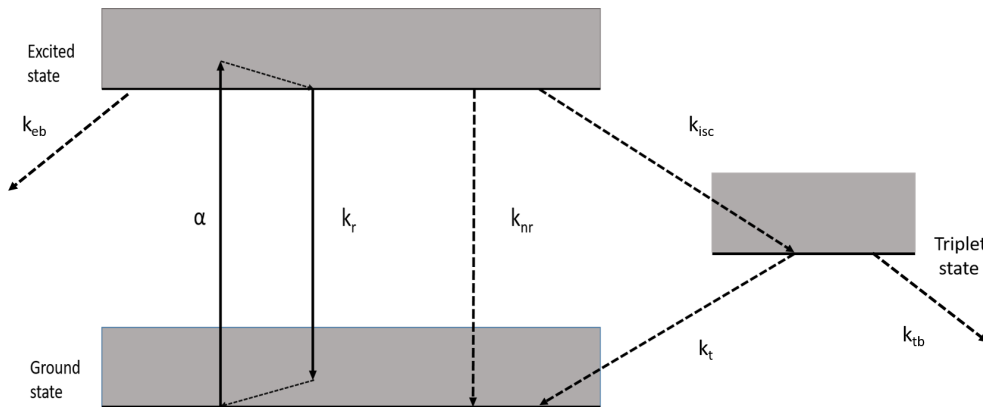


FIGURE 1.3: Energy diagram for a three-level system with photobleaching

sibility of permanent photobleaching by introducing two non radiative pathways from the excited and the ground state to the photobleached state b , with rate respectively k_{eb} and k_{tb} . Then again upgrading equation 1.12 we obtain

$$\frac{d}{dt} \begin{pmatrix} g \\ e \\ t \end{pmatrix} = \begin{pmatrix} -\alpha & (k_r + k_{nr}) & kt \\ \alpha & -(k_r + k_{nr} + k_{isc} + k_{eb}) & 0 \\ 0 & k_{isc} & -(k_t + k_{tb}) \end{pmatrix} \begin{pmatrix} g \\ e \\ t \end{pmatrix} = \mathcal{M} \begin{pmatrix} g \\ e \\ t \end{pmatrix}. \quad (1.17)$$

We are now dealing with an open system (due to the photobleached state) and therefore $Det[\mathcal{M}] \neq 0$. In nature many physical mechanism are known to somehow

affect (most likely to decrease) the light emitted by a fluorescent molecule. This phenomena, such as fluorescence resonant energy transfer or intersystem crossing are two of these mechanisms but are relatively well understood. Photobleaching in fact has still many questions to be answered but from experimental observations it is clear how the decreasing number of photons emitted by a fluorescent molecule depends both on the energy level and rate coefficients of the molecule itself and on its environment. With environment it has to be pointed out that also an overexposure to laser radiation of the sample may end up in a smaller fluorescence yield that is permanent. Many ways of reducing photobleaching have been proposed, such as using a two photons excitation or lowering the intensity of the excitation beam but all of these are likely to end up in a reduction of the fluorescence signal itself.

1.2 Optics and Theory

1.2.1 Fundamentals

It is well known that the resolution of an optical imaging system such as cameras or microscopes is limited by diffraction. This limit takes name after Ernst Karl Abbe which stated that an optical system characterized by a given *numerical aperture* NA and working at a certain wavelength λ cannot resolve two light sources closer than

$$d = \frac{\lambda}{2NA} \quad (1.18)$$

The numerical aperture of an optical system is a measure of its ability to gather light and resolve fine specimen detail at a fixed object distance and it is equal to $NA = n * \sin(\theta)$, with n being the refractive index of the medium in which light propagates and θ being the half numerical aperture of the system, as shown in Fig. 1.4.

From this picture we can see that every non ideal imaging system will not collect light rays outside the angular sector defined by θ . Let us now consider an

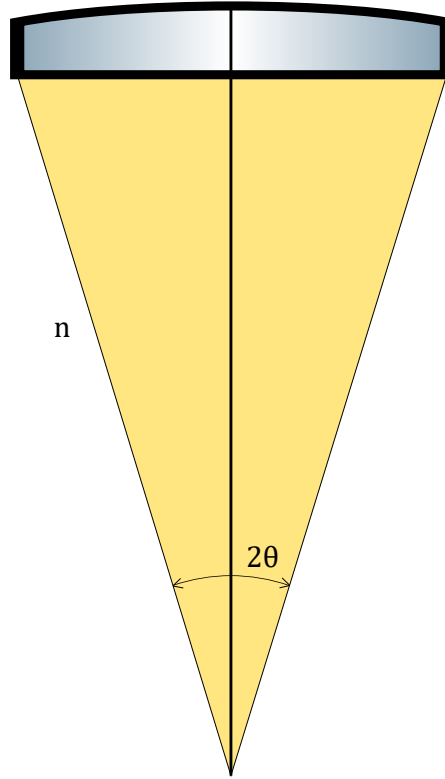


FIGURE 1.4: Numerical Aperture of an optical system

electromagnetic wave propagating in a medium of refractive index n , this wave is characterized as a field $E(\vec{r}, t)$ that varies in space and time; therefore we can turn these variations into spatial frequencies $\vec{\kappa}$ and temporal frequencies ν , respectively. Using the conventions adopted in [1], we can relate the quantities mentioned before in

$$E(\vec{r}, t) = \int \mathcal{E}(\boldsymbol{\kappa}, \nu) e^{i2\pi(\boldsymbol{\kappa} \cdot \vec{r} - \nu t)} d^3 \boldsymbol{\kappa} d\nu \quad (1.19)$$

$$\mathcal{E}(\vec{r}, t) = \int E(\vec{r}, t) e^{-i2\pi(\boldsymbol{\kappa} \cdot \vec{r} - \nu t)} d^3 \vec{r} dt \quad (1.20)$$

Where we will address to $\mathcal{E}(\boldsymbol{\kappa}, \nu)$ as radiant field and $\boldsymbol{\kappa} = (\kappa_x, \kappa_y, \kappa_z)$ will be called wave vector. We highlight the relation $\vec{k} = 2\pi\boldsymbol{\kappa}$. To each temporal frequency ν is associated a wave number κ defined as $\kappa = \frac{n}{c}\nu$, with c being the speed of light in the free space ($c = 3.0 * 10^8 m/s$); we can also define an associated wavelength $\lambda = \frac{c}{\nu}$.

To image an object means that a two dimensional plane (called object plane) is mapped onto a plane with the same characteristics and therefore called image

plane. Due to the symmetry of an imaging process, it is easier to consider $\vec{r} = (x, y, z) = (\boldsymbol{\rho}, z)$, with $\boldsymbol{\rho}$ lying in a 2D plane. We can now rewrite equations 1.19 and 1.20 in function of the only $\boldsymbol{\rho}$

$$E(\boldsymbol{\rho}) = \int \mathcal{E}(\boldsymbol{\kappa}_\perp) e^{i2\pi\boldsymbol{\rho}\cdot\boldsymbol{\kappa}_\perp} d^2\boldsymbol{\kappa}_\perp \quad (1.21)$$

$$\mathcal{E}(\boldsymbol{\kappa}_\perp) = \int E(\boldsymbol{\rho}) e^{-i2\pi\boldsymbol{\kappa}_\perp\cdot\boldsymbol{\rho}} d^2\boldsymbol{\rho} \quad (1.22)$$

Where it holds the energy-momentum relation

$$\kappa^2 = \kappa_\perp^2 + \kappa_z^2 = \left(\frac{n\nu}{c}\right)^2 \quad (1.23)$$

given that

$$\boldsymbol{\kappa} = (\kappa_x + \kappa_y + \kappa_z) = (\boldsymbol{\kappa}_\perp + \kappa_z). \quad (1.24)$$

The full wave vector representation of the radiant field in three dimensions, also presented in [5], is defined by a 3D Fourier transform as follows

$$\mathcal{E}(\boldsymbol{\kappa}_\perp, \kappa_z) = \iint E(\boldsymbol{\rho}, z) e^{-i2\pi\boldsymbol{\kappa}_\perp\cdot\boldsymbol{\rho}} e^{-i2\pi\kappa_z\cdot z} d^2\boldsymbol{\rho} dz \quad (1.25)$$

where the radiant field in three dimensions is related to the field on a given plane by

$$\mathcal{E}(\boldsymbol{\kappa}_\perp, \kappa_z) = \mathcal{E}(\boldsymbol{\kappa}_\perp) \delta(\kappa - \sqrt{\kappa^2 - \kappa_\perp^2}) \quad (1.26)$$

with the field traveling in the positive z direction only.

What does it mean for a field to propagate? How does it change with space and time? The spatiotemporal evolution of an electric field $E_x(\vec{r}, t)$ is determined by the Maxwell's equations. Applying these equations to a single field component, we obtain a time-dependent, inhomogeneous scalar wave equation

$$\left(\nabla^2 - \frac{\kappa^2}{\nu^2} \frac{\partial^2}{\partial t^2}\right) E(\vec{r}, t) = -S(\vec{r}, t) \quad (1.27)$$

with $S(\vec{r}, t)$ standing for the light source term. From eq. 1.27, one can retrieve the spatial and temporal evolution solving it with the proper source term and proper

boundary conditions.

1.2.2 Optical functions

In this paragraph, functions will be introduced that may be useful to understand the performances of an optical system. The first function we are going through is the so called *Coherent Spread Function (CSF)*. As anticipated before, real optical systems introduce non idealities that have to be taken into account. The pupil function $P(\mathbf{r})$ is a mathematical tool that characterizes not only the lens size but also the deviation from the ideal phase transmission. The pupil function or aperture function describes how a wave is affected once transmitted through an optical imaging system such as a microscope, a camera or the human eye. More specifically, it is a complex function of the position in the aperture that indicates the relative change in amplitude and phase of the wave itself. For example, a simple pupil function could be

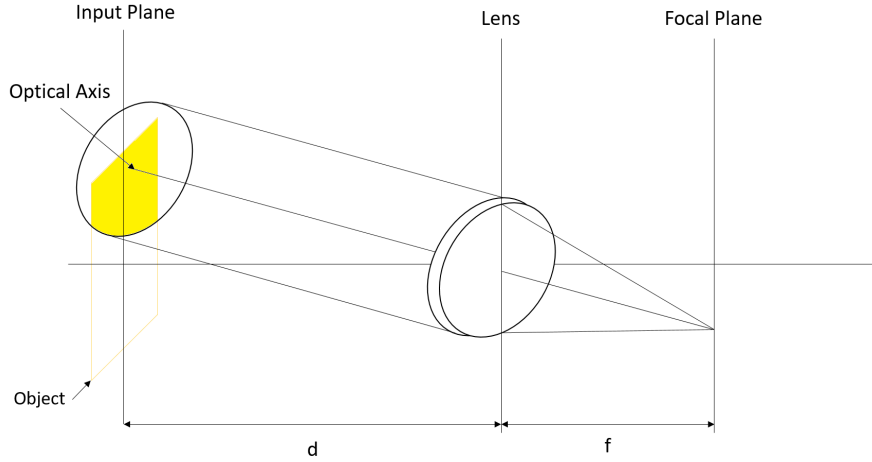
$$P(x, y) = \begin{cases} 1 & \text{inside the lens aperture} \\ 0 & \text{otherwise} \end{cases} \quad (1.28)$$

Its Fourier transform is defined as follows

$$\mathcal{P}(\boldsymbol{\kappa}_{\perp}) = \iint P(\boldsymbol{\xi}) e^{-i2\pi\boldsymbol{\kappa}_{\perp} \cdot \boldsymbol{\xi}} d^2\xi \quad (1.29)$$

being $\boldsymbol{\xi}$ the lateral coordinates in the lens plane. At this point we want to image our object plane and characterize the performance of our imaging system which will be depending both on the system itself and on the pupil function. Let us consider the case of a single lens imaging as depicted in Fig. 1.5. It is well known that the general field transfer through a lens is represented by

$$\frac{1}{s_0} + \frac{1}{s_1} = \frac{1}{f} \quad (1.30)$$

FIGURE 1.5: Imaging by a lens of focal f

being s_0 and s_1 the object and the image plane distances from the lens axis and f its focal length. Unfortunately, despite being achievable ideally, perfect imaging with a single lens cannot be performed in reality due to its finite radius.

We can simplify our approach by introducing the well known Fresnel approximation, which finds its importance when considering the electric field diffraction pattern integral:

$$E(\boldsymbol{\rho}, z) = -i \frac{\kappa}{z} \int E(\boldsymbol{\rho}_0, 0) e^{i2\pi\kappa R} d^2\boldsymbol{\rho}_0. \quad (1.31)$$

Anyway, analytically solving this integral happens to be difficult because of the presence of the R variable in the exponential. We can consider a shift of the variable ρ , determined by

$$\rho^2 = (x - x_0)^2 + (y - y_0)^2, \quad (1.32)$$

For geometrical reason, it is straight forward that

$$R = \sqrt{\rho^2 + z^2} = z \sqrt{1 + \left(\frac{\rho}{z}\right)^2}, \quad (1.33)$$

now, thanks to Taylor expansion we obtain:

$$R = \sqrt{\rho^2 + z^2} = z \sqrt{1 + \left(\frac{\rho}{z}\right)^2} = z \left[1 + \frac{1}{2} \left(\frac{\rho}{z}\right)^2 - \frac{1}{8} \left(\frac{\rho}{z}\right)^4 + \dots \right], \quad (1.34)$$

further, considering $\kappa \frac{\rho^4}{8z^3} \ll 2\pi$, we can get

$$\frac{\rho^4}{\lambda} \ll 8z^3, \quad (1.35)$$

which is called Fresnel Approximation. Along with the finite radius, Fresnel approximation also plays a role in single lens imaging due to the fact that perfect imaging implies to be in the Fresnel regime, as shown in [6].

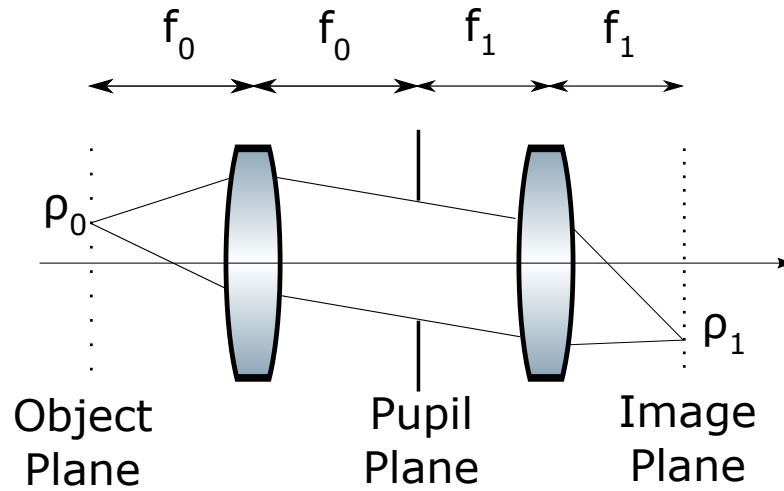


FIGURE 1.6: 4f configuration

That is why it is going to be considered the case where an imaging system with two lenses of focal f_0 and f_1 are such that the distance between their main planes is $f_0 + f_1$, as shown in Fig. 1.6.

With this in mind, we call Coherent spread function the quantity

$$CSF(\boldsymbol{\rho}) = \left(\frac{\kappa}{f_0}\right)^2 \int P(\boldsymbol{\xi}) e^{-i2\pi \frac{\kappa}{f_0} \boldsymbol{\rho} \cdot \boldsymbol{\xi}} d^2 \boldsymbol{\xi}. \quad (1.36)$$

Combining equation 1.29 with 1.36 we finally obtain the relation between the CSF and the Fourier transform of the pupil function

$$CSF(\boldsymbol{\rho}) = \left(\frac{\kappa}{f_0}\right)^2 \mathcal{P}\left(-\frac{\kappa}{f_0} \boldsymbol{\rho}\right). \quad (1.37)$$

From a simple comparison with 1.29, it is clear how the CSF is nothing more than a scaled version of the Fourier transform of the Pupil function.

Starting with 1.36 and applying a Fourier transform, another important optical functions is derived

$$CTF(\boldsymbol{\kappa}_\perp) = \int CSF(\boldsymbol{\rho}) e^{-i2\pi\boldsymbol{\kappa}_\perp \cdot \boldsymbol{\rho}} d^2\boldsymbol{\rho} \quad (1.38)$$

referred to as the coherent transfer function (CTF). Again it easy to infer how CTF is simply a scaled version of the Pupil function.

$$CTF(\boldsymbol{\kappa}_\perp) = P\left(\frac{f_0}{\kappa} \boldsymbol{\kappa}_\perp\right). \quad (1.39)$$

Thanks to all of what it has been defined up to now, two of the most important functions in incoherent imaging theory can be introduced, the Point Spread Function and its Fourier transform, the Optical Transfer Function.

The first is analytically defined as

$$PSF(\boldsymbol{\rho}) = \frac{|CSF(\boldsymbol{\rho})|^2}{\int |CSF(\boldsymbol{\rho})|^2 d^2\boldsymbol{\rho}}, \quad (1.40)$$

while a further excursus on the coordinate system is needed before showing the expression of the latter. The OTF is in fact easier to comprehend if we put ourselves in a two dimensional plane, as the one depicted in Fig. 1.7. We have two points determined by the two vectors $\boldsymbol{\rho}$ and $\boldsymbol{\rho}'$ departing from the same origin, now we can define new coordinates in the following way:

$$\boldsymbol{\rho}_c = \frac{1}{2}(\boldsymbol{\rho} + \boldsymbol{\rho}'); \quad (1.41)$$

$$\boldsymbol{\rho}_d = \boldsymbol{\rho} - \boldsymbol{\rho}'. \quad (1.42)$$

Respectively, $\boldsymbol{\rho}_c$ and $\boldsymbol{\rho}_d$ denote the mean and the difference vector between a pair of point pointed by $\boldsymbol{\rho}$ and $\boldsymbol{\rho}'$. We finally have all of what it is needed to mathematically define the Optical Transfer Function of a system:

$$OTF(\boldsymbol{\kappa}_{\perp d}) = \frac{\int CTF(\boldsymbol{\kappa}_{\perp c} + \frac{1}{2}\boldsymbol{\kappa}_{\perp d}) CTF^*(\boldsymbol{\kappa}_{\perp c} - \frac{1}{2}\boldsymbol{\kappa}_{\perp d}) d^2\boldsymbol{\kappa}_{\perp c}}{\int |CTF(\boldsymbol{\kappa}_{\perp c})|^2 d^2\boldsymbol{\kappa}_{\perp c}} \quad (1.43)$$

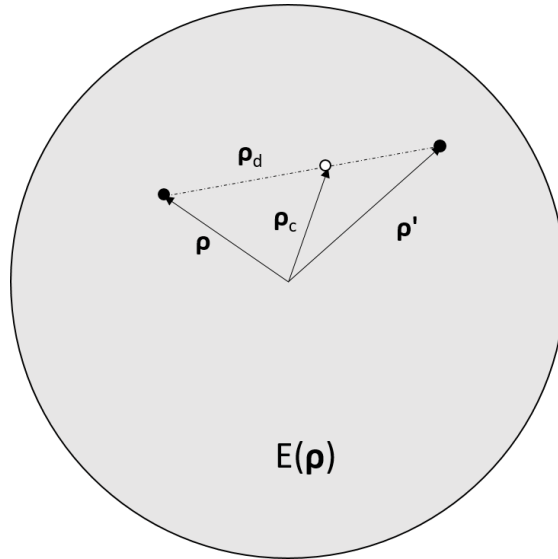


FIGURE 1.7: Coordinate system used for OTF definition.

1.2.3 Circular Pupil

In this section, we are going to exploit the concept introduced in the section 1.2.2 in order to examine the imaging performance of a system with an unobstructed circular aperture pupil. For this kind of aperture of given radius a , the pupil function is written as

$$P(\boldsymbol{\xi}) = \begin{cases} 1 & \xi \leq a \\ 0 & \textit{otherwise} \end{cases} \quad (1.44)$$

Thanks to equation 1.39 we can derive the coherent spread function right away

$$CTF(\boldsymbol{\kappa}_\perp) = \begin{cases} 1 & \kappa_\perp \leq \frac{1}{2}\Delta\kappa_{\perp 0} \\ 0 & \kappa_\perp > \frac{1}{2}\Delta\kappa_{\perp 0} \end{cases} \quad (1.45)$$

where it has been taken into account the full span of $\boldsymbol{\kappa}_\perp$, which is found to be:

$$\Delta\kappa_{\perp 0} = 2\kappa \frac{a}{f_0} = \kappa\Delta\theta. \quad (1.46)$$

Once obtained the Coherent Transfer function, one can retrieve the Coherent Spread function associated with the imaging system by simply applying a Fourier

transform to eq. 1.45; this gives as result:

$$CSF(\rho) = \frac{\pi}{4} \Delta\kappa_{\perp 0}^2 jinc(\pi \Delta\kappa_{\perp 0} \rho). \quad (1.47)$$

For the expression of the Coherent Spread function it has been used the *jinc* function, which is defined as

$$jinc(2\pi\kappa_{\perp}\rho) = \frac{J_1(2\pi\kappa_{\perp}\rho)}{\pi\kappa_{\perp}\rho}. \quad (1.48)$$

What has been called J_1 in eq. 1.48 is the first order cylindrical Bessel function; with Bessel function one means all of the canonical solution of the Bessel's differential equation, from which they are named after. An integral representation of this family of cylindrical functions is found in equation 1.49, where n is an integer parameter also called order of the function

$$J_n(x) = \frac{1}{\pi} \int_0^{\pi} \cos(n\tau - x\sin(\tau)) d\tau. \quad (1.49)$$

Now, with the help of definition 1.40 and the Parseval's theorem, it is easy to retrieve the PSF for a 4f imaging system. In particular, Parseval's theorem states that the sum of the squares of the Fourier coefficients of a function equals the integral of the function itself squared. It means that in one dimension, for a function $f \in L^2(\text{Re})$ it is true that

$$\int_{-\infty}^{\infty} |F(X)|^2 dx = \int_{-\infty}^{\infty} |\mathcal{F}(\kappa_x)|^2 d\kappa_x. \quad (1.50)$$

With this in mind, equation 1.40 can be modified as follows

$$\int |CSF(\boldsymbol{\rho})|^2 d^2\boldsymbol{\rho} = \int |CSF(\boldsymbol{\kappa}_{\perp})|^2 d^2\boldsymbol{\kappa}_{\perp} = \left(\frac{\kappa}{f_0}\right)^2 \int |P(\boldsymbol{\xi})|^2 d^2\boldsymbol{\xi} = \kappa^2 \Omega_0 \quad (1.51)$$

where Ω_0 is the pupil solid angle referred to the object plane in the case of a circular pupil

$$\Omega_0 = \frac{1}{f_0^2} \int |P(\boldsymbol{\xi})|^2 d^2\boldsymbol{\xi} = \frac{\pi}{4} \left(\frac{\Delta\kappa_{\perp 0}}{\kappa}\right)^2. \quad (1.52)$$

Further, the definitions for PSF and OTF can be recast in a simpler form

$$PSF(\boldsymbol{\rho}) = \frac{1}{\kappa^2 \Omega_0} \quad (1.53)$$

and

$$OTF(\boldsymbol{\kappa}_{\perp d}) = \frac{1}{\kappa^2 \Omega_0} \int CTF(\boldsymbol{\kappa}_{\perp c} + \frac{1}{2}\boldsymbol{\kappa}_{\perp d}) CTF^*(\boldsymbol{\kappa}_{\perp c} - \frac{1}{2}\boldsymbol{\kappa}_{\perp d}) d^2 \boldsymbol{\kappa}_{\perp c}. \quad (1.54)$$

Finally, using equations 1.47 and 1.53 these last two equalities become

$$PSF(\rho) = \frac{\pi}{4} \Delta \kappa_{\perp 0}^2 \text{jinc}^2(\pi \Delta \kappa_{\perp 0} \rho) \quad (1.55)$$

and

$$OTF(\boldsymbol{\kappa}_{\perp}) = \begin{cases} \frac{2}{\pi} \left(\cos^{-1} \left(\frac{\kappa_{\perp}}{\Delta \kappa_{\perp 0}} \right) - \frac{\kappa_{\perp}}{\Delta \kappa_{\perp 0}} \sqrt{1 - \frac{\kappa_{\perp}^2}{\Delta \kappa_{\perp 0}^2}} \right) & \kappa_{\perp} \leq \Delta \kappa_{\perp 0} \\ 0 & \kappa_{\perp} > \Delta \kappa_{\perp 0} \end{cases} \quad (1.56)$$

These last two imaging functions together with the CTF and the CSF presented in equations 1.45 and 1.47 respectively and their mutual relations are shown in Fig. 1.8. Due to its definition, it is clear how the Optical Transfer Function has a frequency support twice as large as that of the Coherent Transfer Function; however OTF response is not constant over its larger bandwidth, in particular lower spatial frequencies are more efficiently transferred by the system to the image plane than higher κ_{\perp} values. The well known Point Spread Function Full Width at Half Maximum is defined to be

$$\Delta \rho_0 = \frac{\lambda}{2NA_0}, \quad (1.57)$$

as already anticipated in 1.2.1. This leads to

$$\frac{\pi}{n^2} NA_0^2 = \Omega_0 = \frac{\pi}{4} \left(\frac{\Delta \kappa_{\perp 0}}{\kappa} \right), \quad (1.58)$$

which links the spatial frequencies resolution to the pupil solid angle referred to the object plane.

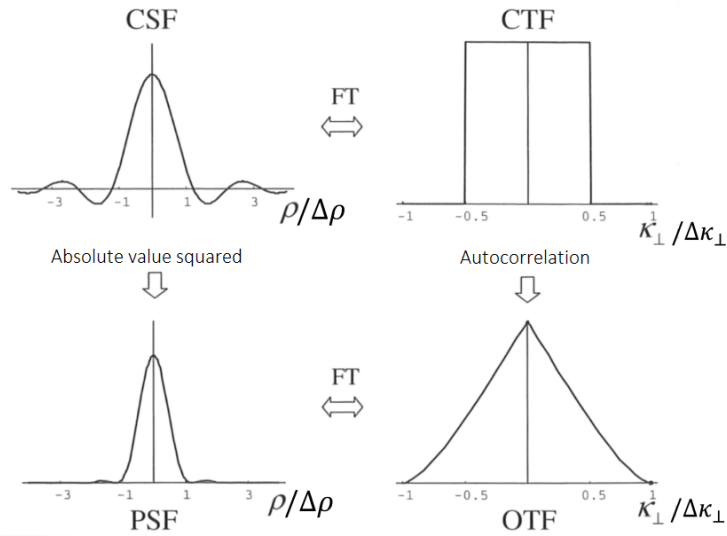


FIGURE 1.8: Basic imaging functions for a pupil of circular aperture [1]

1.2.4 Frequency Support

Up to this section, only a separated representation of fields given from Fourier Transform has been considered. What is called *Angular Spectrum* representation, i.e. the full wavevector picture of radiant fields is on the other hand defined by a three dimensional Fourier Transform

$$\mathcal{E}(\boldsymbol{\kappa}_{\perp}, \kappa_z) = \iint E(\boldsymbol{\rho}, z) e^{-i2\pi\boldsymbol{\kappa}_{\perp}\boldsymbol{\rho} - i\kappa_z z} d^2\boldsymbol{\rho} dz, \quad (1.59)$$

provided that

$$\mathcal{E}(\boldsymbol{\kappa}_{\perp}, \kappa_z) = \mathcal{E}(\boldsymbol{\kappa}_{\perp}) \delta\left(\kappa_z - \sqrt{\kappa^2 - \kappa_{\perp}^2}\right) \quad (1.60)$$

with the z component of the $\boldsymbol{\kappa}$ vector being limited by eq. 1.23 and with fields traveling only towards the positive z direction.

A definition for the full vector representation of the Coherent Spread Function can be given in an analogous way

$$CTF(\boldsymbol{\kappa}_{\perp}, \kappa_z) = CTF(\boldsymbol{\kappa}_{\perp}) \delta\left(\kappa_z - \sqrt{\kappa^2 - \kappa_{\perp}^2}\right). \quad (1.61)$$

Taking a look at the definition of the CTF full vectorial representation, the delta function (and in particular its argument) defines regions of the support for κ_z ,

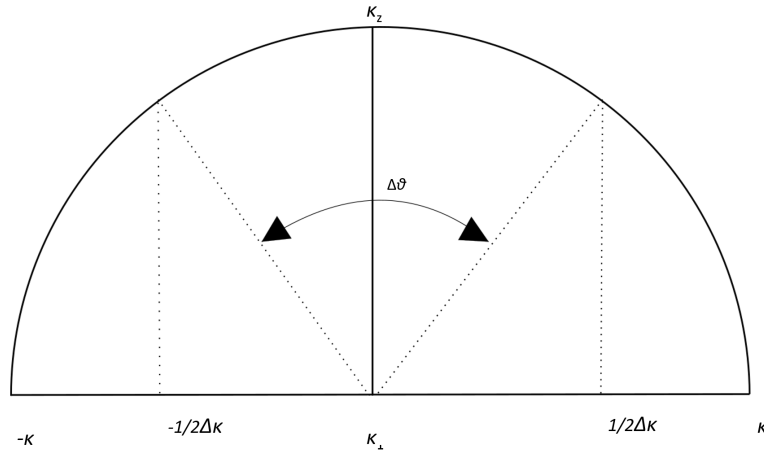


FIGURE 1.9: Frequency Support for the Coherent Spread Function from energy momentum relation

which can be represented thanks to the so called Ewald sphere. In Fig. 1.9 we see how, at a given angular interval $\Delta\theta$, it corresponds to a spatial frequency interval both for the z and the radial direction. These intervals are equal to

$$\Delta\kappa_z = \kappa - \kappa \cdot \cos(\Delta\theta) = \frac{n}{\lambda} \left(1 - \sqrt{1 - \frac{NA^2}{n^2}} \right) \simeq \frac{NA^2}{2n\lambda} \quad (1.62)$$

and

$$\Delta\kappa_{\perp} = 2\kappa \cdot \sin(\Delta\theta) = \frac{2NA}{\lambda} \quad (1.63)$$

respectively; with NA being the numerical aperture of the optical system, λ the radiation wavelength, n the medium refractive index and $\Delta\theta$ the angle spanned by the aperture. As a further remark, the final step in eq. 1.62 has been performed thanks to the assumption that the $\frac{NA^2}{n^2}$ ratio is much smaller than 1.

Let us now consider an incoherent intensity imaging system, all of what has been said in three dimensions for the Coherent Spread Function, can be extended to the Optical Transfer Function, defined in the case of a circular pupil as displayed in eq. 1.56. Up to now, except for the energy-momentum relation, no other constraint was imposed on the spatial frequencies; here we put ourselves in the case where $\kappa_{\perp}^2 \ll \kappa^2$, also known as Fresnel approximation, such that it is possible to consider valid the substitution

$$\sqrt{\kappa^2 - \kappa_{\perp}^2} \rightarrow \kappa \left(1 - \frac{\kappa_{\perp}^2}{2\kappa^2} \right). \quad (1.64)$$

With all this in mind, it is easy to find that

$$OTF(\boldsymbol{\kappa}_\perp, \kappa_z) = \frac{1}{\kappa^2 \Omega} \int CTF(\boldsymbol{\kappa}_{\perp c} + \frac{1}{2}\boldsymbol{\kappa}_\perp) CTF^*(\boldsymbol{\kappa}_{\perp c} - \frac{1}{2}\boldsymbol{\kappa}_\perp) \delta(\kappa_z + \frac{1}{\kappa} \boldsymbol{\kappa}_{\perp c} \cdot \boldsymbol{\kappa}_\perp) d^2 \boldsymbol{\kappa}_{\perp c}. \quad (1.65)$$

Where again the delta function dictates the support region for κ_z but with a significant difference: for the OTF support is no longer as strictly defined as it was for the CTF support since κ_z can in principle span a wider range of value for a given spatial frequency $\boldsymbol{\kappa}_\perp$. Let us now demonstrate this last statement. From the definition of the circular Coherent Transfer Function, it can be easily estimated the maximum value of the dot product $\boldsymbol{\kappa}_{\perp c} \cdot \boldsymbol{\kappa}_\perp$

$$|\boldsymbol{\kappa}_{\perp c} \cdot \boldsymbol{\kappa}_\perp|_{max} = \frac{1}{2} \kappa_\perp (\Delta \kappa_\perp - \kappa_\perp), \quad (1.66)$$

as well as the upper bound on $|\kappa_z|$

$$|\kappa_z| = \frac{\kappa_\perp}{2\kappa} (\Delta \kappa_\perp - \kappa_\perp). \quad (1.67)$$

In Fig. 1.10 it is shown an illustration of the supported values of the axial spatial frequencies as function of the radial spatial frequencies in the 3 dimensions. From a geometrical consideration, the full angle that encloses all of the frequency support is

$$\Delta \theta = \frac{\Delta \kappa_\perp}{\kappa}, \quad (1.68)$$

whereas in Fig. 1.10 it is highlighted its half. This angular interval corresponds to the imaging optics collection angle, so that its complementary is the so called "missing cone", indicating the spatial frequencies components that cannot be imaged at all; the larger this cone, the narrower the imaging bandwidth. The existence of this missing cone of spatial frequencies is the reason why a 4f wide field microscope is unable to image different planes deep in a thick sample. Optical sectioning however, can be exploited in many different techniques and with different optical setups, among which "Selective Plane Illumination Microscopy" will be analyzed in the following section.

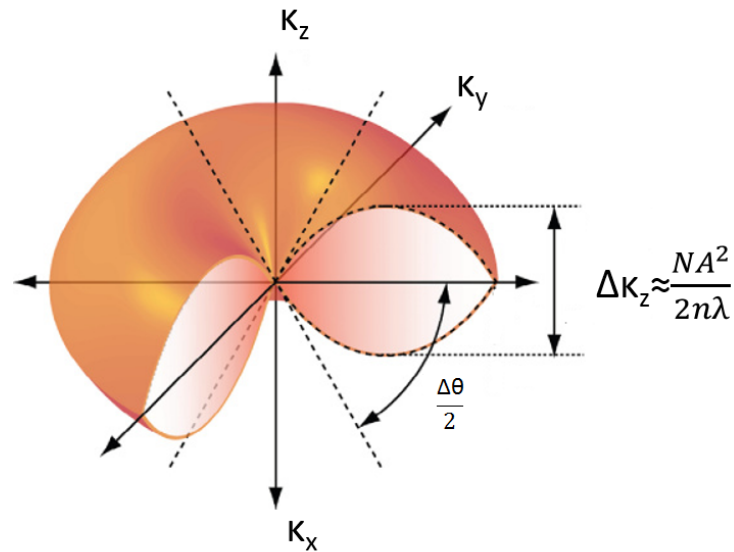


FIGURE 1.10: 3D Frequency Support of a circular pupil OTF within the Fresnel approximation

1.3 Selective Plane Illumination Microscopy

1.3.1 Introduction

After its birth in 2004 [7], selective plane illumination microscopy (SPIM) or light-sheet fluorescence microscopy (LSFM) has been proved to have very interesting in vivo imaging properties also in large samples over extended time periods and easy way of handling these samples, making this technique a powerful tool to investigate a various range of phenomena both in single cell samples [8] and entire organisms [9]. This paragraph aims to introduce the working principle of the single plane illumination microscopy and why one should prefer this technique among others. To exploit this, a quantitative analysis of optical performances will be given together with LSFM intrinsic advantages in analyzing in vivo specimens.

1.3.2 Working Principles

One of the main differences that stand out when comparing a LSFM optical setup or a conventional epifluorescence microscope (confocal or multiphoton) is the absence of overlapping of the illumination and detection paths. In fact, a setup for LSFM is of the kind depicted in Fig. 1.11: two objectives are placed orthogonally to each other so that the sample chamber is centered with respect to the illumination and detection path. Single Plane Illumination Microscopy also implies that fluorescence is only excited on a narrow sheet of light coming from the cylindrical lens; this is a major difference with wide field microscopy or confocal microscopy, where the sample was entirely illuminated or point-by-point scanned. The light sheet illumination is such that the detection field of view is entirely illuminated as the same time; this, together with the use of a fast camera (hundreds of frames per second), ends up with large volumes fast scanning.

1.3.3 Optical and speed performances

In this section, mechanical and optical performances will be analyzed to give the reader an overall picture of what are the potentiality of the single illumination plane microscopy. Thanks to the separation of the illumination and the detection optical paths, higher imaging speeds can be achieved with respect to setup like 1.11, setup A). As shown in [10], for a sample of roughly 1 mm of volume, with a camera exposure time of 50 ms and with 500 planes recorded, the time taken for such a measure would be of 1us/pixel, against the 20-30us/pixel achieved with a confocal approach to the same sample, obtaining a factor of 20 in the acquisition speed. For what said above, the LSFM is excellent at recording the activity of large biological samples with frequent time acquisitions. Let us now focus on the optical achievement of light sheet microscopy. Since this technique does not need in its simplest implementation anything more than a regular wide field setup (Fig. 1.11), the lateral resolution will be the same as wide field microscopy, which is given by Abbe diffraction limit $d_{lateral} = 0.5 \frac{\lambda}{NA}$, as already discussed in section

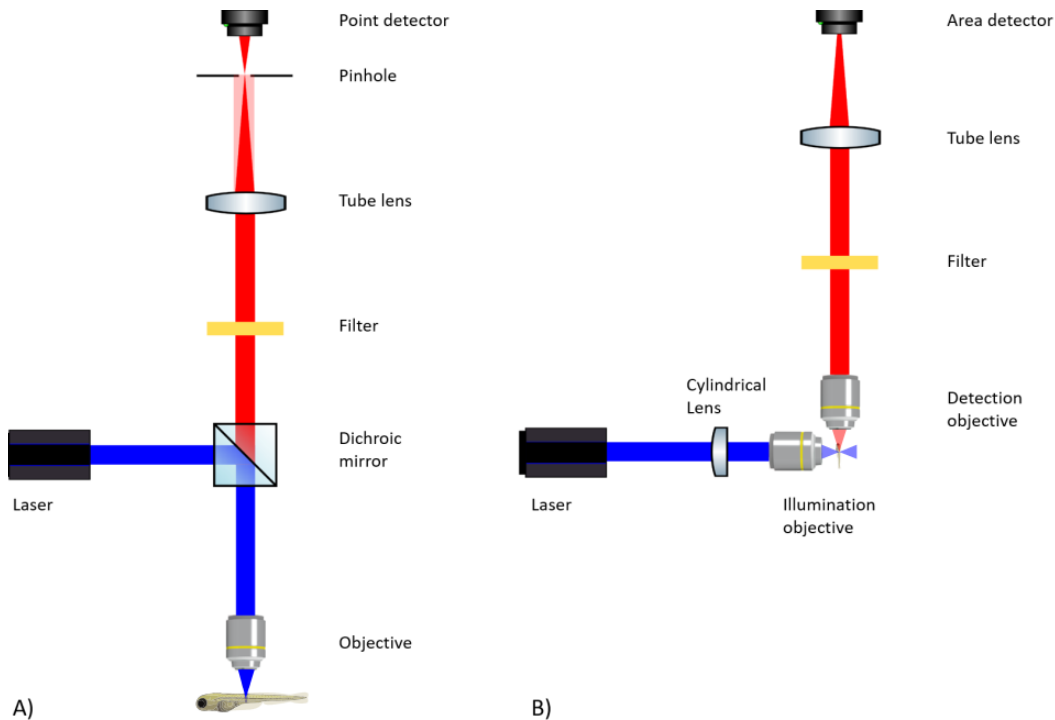


FIGURE 1.11: (A) In a conventional epifluorescence microscope the laser source provides radiation at a given wavelength (blue in figure, this radiation is then reflected by a dichroic mirror into the rear of the objective which focuses the light onto the specimen. The illumination radiation excites the fluorophores of the sample so that fluorescence radiation is emitted at a lower energy (red in figure). Once the radiation is transmitted by the dichroic mirror, it is focused by the tube lens onto the detector with the purpose of forming a point image. In front of the point detector, a pinhole is placed in order to prevent scattered light from non in focus planes to be imaged. (B) In the second part of the picture a simple SPIM setup is shown. The first difference with an epifluorescence setup is the presence of a cylindrical lens used to form a light-sheet in the back focal plane of the detection objective. The illumination sheet impinges on the specimen that responds to excitation with the emission of fluorescence. The fluorescence signal is spectrally separated from the laser light with the help of a filter for than being focused by a tube lens onto the area detector.

1.2.1. Let us now consider how optical sectioning is performed: for LSFM this is performed solely thanks to plane illumination exciting the fluorophores exclusively in the back focal plane of the detection objective; while for confocal case this was done only with the pinhole placed in front of the detector. Let us take now the case where the laser beam has a Gaussian shape as the one displayed in picture 1.13, this is in fact the most common intensity profile in the direction perpendicular to the propagation axis. The function $w(z)$ which gives half of the thickness in function of the distance from the minimum waist point, it can be expressed as

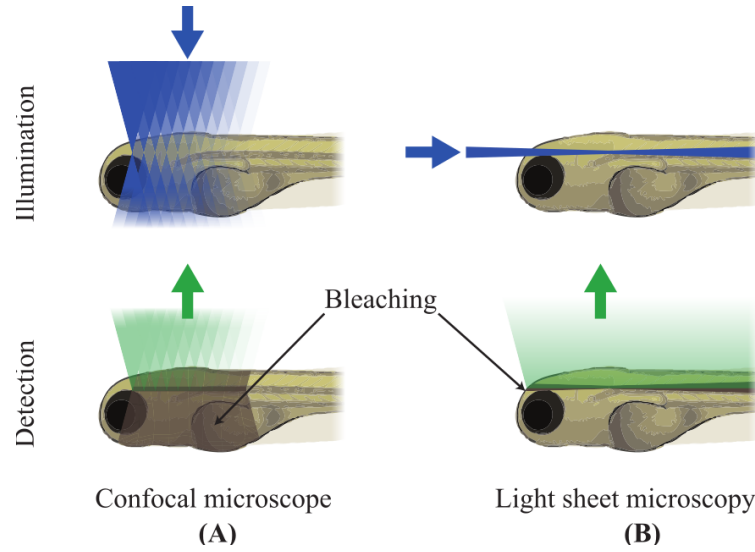


FIGURE 1.12: Focusing of illumination light in a) confocal microscopy and b) light sheet microscopy [9]

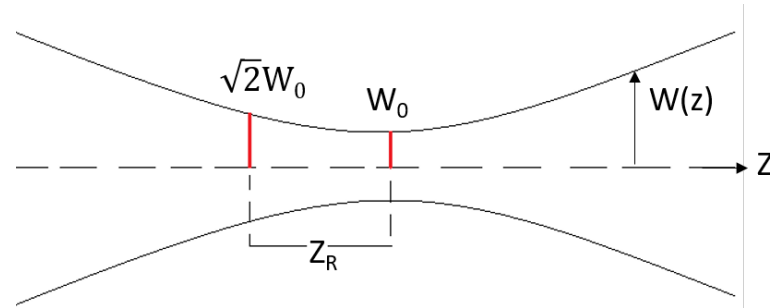


FIGURE 1.13: Gaussian beam width $w(z)$ as a function of the distance z along the beam profile.

follows:

$$w(z) = w_0 \sqrt{1 + \left(\frac{z}{z_R}\right)^2}. \tag{1.69}$$

Where z_R is the so called Rayleigh range and it can be calculated once knowing the waist size w_0 and the wavelength λ thanks to the following relation

$$z_R = \frac{\pi w_0^2}{\lambda}, \tag{1.70}$$

holding for in vacuum beam propagation and beam waist being expressed as follows

$$w_0 \simeq \frac{\lambda}{2NA_{ill}}. \tag{1.71}$$

From the analysis made in the previous sections, a possible resolution improvement could be determined by a reduction in the beam profile, since the total PSF is determined by the multiplication of the illumination profile with the detection PSF. It has to be kept in mind that the smaller the waist minimum, the faster the beam will diverge respect to the z axis, making the light sheet crafting critical to the requested performances to the system. Usually eq. 1.70 is taken as a resolution criterion for an optical system since it defines the excited part of the sample that is imaged by a general detection scheme. That is why it is often compared to the axial resolution of the illumination system, so that

$$z_R \simeq \frac{n\lambda}{NA_{ill}^2}. \quad (1.72)$$

Since the optical sectioning is done thanks to the light sheet, it is straight forward that its thickness is responsible for the axial resolution. This intrinsic optical sectioning is reflected in the fact that for SPIM a better axial resolution is achieved with respect to wide field microscopy [11]. On top of that, SPIM gives the possibility of merging different images of the same part of the sample but with light coming from different direction, further improving the wide field axial resolution. A final remark is made for the signal to noise ratio in LSFM: due to larger amount of photons available in fact it has been demonstrated that a contrast of one order of magnitude better can be achieved with reference to confocal-scanning microscopy [12].

1.3.4 Light-sheet engineering

A big challenge in selective illumination plane microscopy is to achieve a high axial resolution imaging over a large field of view. As it was previously said, the overall system point spread function is given by the overlap between the illumination and the detection PSF, therefore a better axial resolution can be obtained by increasing the axial confinement of the light sheet. The fact that high NA Gaussian beams rapidly diverge away from the propagation axis however limits the axial

resolution to a best of $1\mu m$; such a resolution can be adequate for imaging at a cellular scale level, but it can be a bottleneck in subcellular analysis in a large field of view. Several solutions to overcome this limit has been proposed, all of them using non-diffracting beam modes, such as Bessel beams, whose amplitude profile is described by Bessel function of the first kind. The peculiarity of non-diffracting beams is that they maintain a constant beam minimum waist over several Rayleigh length with respect to a Gaussian beam at the same NA.

A question may rise: how do the side lobes of the Bessel beam affect the imaging capability? Of course side illumination compromises optical sectioning, degrading contrast and overexposing the sample to radiation that is not needed, having the chance of permanently damaging the sample. A solution can be found for example in two-photon illumination, with the main drawback of increasing photobleaching due to the additional exposure or to pulsed light excitation [13]; another solution can be found by the mean of multiple Bessel beams in parallel, with a consequent reduction in each beam peak intensity, further decreasing the hazard of photodamage. Aside Bessel beams, in principle one can use the so called Airy mode, a propagation mode that has been is characterized by a thinner light sheet over a larger field of view with respect to Gaussian beams at comparable NA; the main drawback in this illumination technique does not surface so much in optical hardware complications but rather in an increased data reconstruction, together with the need for the side lobes to remain in focus. Alongside the non-diffractive beam approach, both high axial resolution and large field of view can be obtained using a moderate NA Gaussian beam along the z-axis, given that lower NA beams imply than several planes are in focus at a given time. Again, illuminating such a large region might result in unnecessary photodamage to the sample. The last approach that is presented in this section is the one involving molecular dark states to produce thin, propagating invariant light sheets. To illustrate this process, let us now consider a stimulated emission depletion microscopy (STED), in which the diffraction limit is bypassed thanks to the nonlinear relationship that occurs between the intensity of the illumination light and fluorescence signal. The STED beam depletes the fluorescent state of the molecule in every part of the focus region

through stimulated emission (SE), except at the zero intensity point and its nearby, confining the spatial molecular excitation zone and hence fluorescence radiation. The depletion is achieved through stimulated emission while the saturation of this transition gives rise to the non-linear response allowing the manipulation of the effective fluorescent spot shape and size beyond the Abbe limit. Similarly for light sheet fluorescence microscopy one can exceed the resolution limit given that the degree of parallelization, i.e. the number of beams impinging on the sample at a time, limits the number of axes on which super-resolution can be achieved. Despite the similar approach, STED and SPIM does not require the same amount of power to be working, in fact light sheet fluorescence microscopy needs much lower beam intensities. This lower need for energy reflects in molecular states design, in fact lower energies imply slower switching time, which is more suitable in an in-vivo context. This approach led to a resulting super-resolved light sheet activable region from 5 to 12 times better than the diffraction limited [14].

1.3.5 Fast volume imaging

One of the main attributes of light fluorescence microscopy is speed. In fact, together with a modern sensor (like sCMOS cameras) it can end up with an imaging rate of several hundreds of frames per second. With this in mind, volumetric scanning rates of some Hz are optically achievable, but then a problem arises: together with image acquisition, a mechanical movement of the sample is also needed; this mechanical movement results in a shocking event for the sample, making the displacement of the latter a limiting factor in acquisition speed. This is one of the main challenges in selective plane microscopy and it is one of the reasons for this whole work: a fully working fast selective plane illumination microscope, with scanning performed with the means of dynamic elements such as galvanometric mirrors and adaptive optics, which does not require any sample movement. For this reason, a novel approach to the problem is to insert an electrically tunable lens into the light detection path, such to make it possible to image different object planes in a well determined range [15]. This need for an adaptive element to

reposition the object plane comes after the limitation in depth of field (DOF) and low NA illumination. Different approaches can be followed to extend the DOF, for example by introducing a known phase shift in the detection PSF at the back focal plane of the detection objective lens through deformable mirrors. Instead of using a phase mask to extend to depth of field, the latter can also be performed through the spherical aberrations introduced by SPED microscopy like shown by Tomer et al. [16].

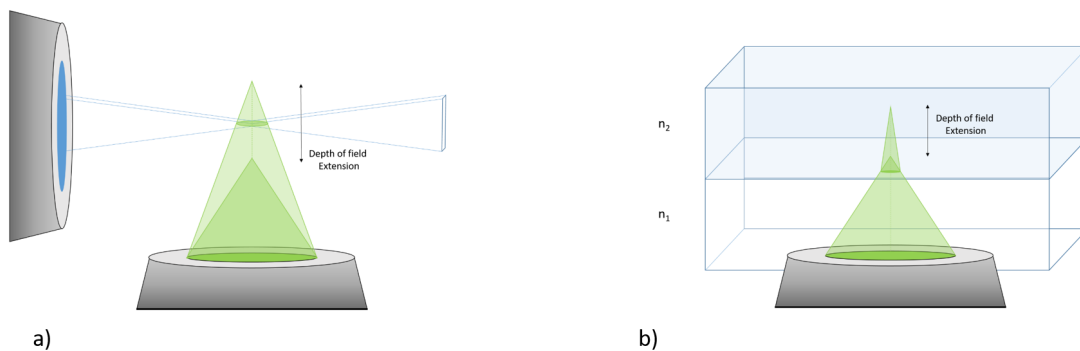


FIGURE 1.14: a) Generic illumination and detection scheme for light sheet imaging. In the extended DOF obtained through an electro-tunable lens and a galvanometric mirror, imaging is performed by defocusing of the adaptable lens. b) Phase coding in order to modify DOF thanks to different media with different refraction index, n_1, n_2 respectively, with $n_2 > n_1$

Instead of performing imaging directly into the sample immersed in a medium with properly corrected immersion objectives, as depicted in fig. 1.14 is shown how DOF extension can be exploited also providing a different optical path length through the immersion medium to produce a deeper focus plane for highly inclined rays. As the reader may expect, a larger mismatch between the two media refractive indices results on one hand in a larger DOF extension while on the other hand it worsens aberrations at the media interface. So far, the DOF extensions approaches to LSFM can be summed up as a trade off between optical efficiency and flexibility. A final remark is worth to be made on the drawbacks of defocus-based methods, for this techniques in fact detection point spread function is delocalised along to light propagation axis, therefore optical efficiency is drastically reduced; furthermore, the larger the extension in the DOF, the more spatial frequencies information is lost, in particular the ones corresponding to higher divergence rays, resulting in a

loss of resolution.

Due to its characteristics, a SPIM microscope exploiting an augmented depth of field through rotating mirrors and adaptive lenses is ideal to perform in vivo imaging, since this technique offers good optical sectioning properties, low phototoxicity for the sample and high achievable image acquisition speed; furthermore, due to the flexibility of a standard SPIM setup, multichannel acquisition is also easy to be implemented. This is why to the goal of this thesis project, a Light Sheet Fluorescence Microscopy setup is implemented (as the one presented in [15]) and a software is written to synchronize the operations of the dynamic elements, to finally acquire frames of living samples to analyze and then extract the system imaging properties.

Chapter 2

Optical design and implementation

In this chapter the structure of the developed microscope, following the general Light Sheet Fluorescence Microscopy scheme given in the previous chapter. In first place, the setup will be broken up into three parts: bright field illumination, fluorescence excitation path and detection; for each of these parts it will be shown both the concept of the path standalone and the part inserted in the whole structure, and how each setup section is placed on the optical table. After this part, a final section is given, to show how the single optical component, together with the CCD sensor, affects the imaging capability of the system, exploiting the concept of numerical aperture and frequency support of an optical element seen in the previous chapter.

2.1 Optical Design

2.1.1 Bright Field Illumination

It is called bright illumination an illumination path such that it allows a rapid inspection of a large part of the sample minimizing the damage induced by light; in fact, bright field light sources are way less powerful than laser sources implied in fluorescence microscopy for example, permitting long exposure. In this project,

bright field illumination is exploited in order to facilitate sample positioning in the microscope chamber, task that would be extremely tedious relying only on a fluorescence signal excited on a single plane. Bright field illumination systems usually share optics with the excitation path of the microscope, whereas in this project the two parties do not share anything except for the sample [17]. Furthermore, this kind of illumination implies the use of telecentric optics, in which the light from the source is collimated and another requirement for it is to be transmitted as uniform as possible over the larger part of the sample achievable. In bright field illumination, the light source (a LED for example) is usually positioned in a sensor conjugated plane lying on the optical axis before or below the sample. Light then impinges and propagates through the sample, for then being collected by an appropriate imaging lens and an imaging sensor (a CCD sensor for example). Therefore, the image formed is thanks to light transmission, that is why the darker the sample, the denser it happens to be, due to the simple fact that denser specimens, due to Lambert-Beer law, absorb more light [18].

As suggested by [1], it is presented the so called Köhler illumination, which is the type of illuminator which has been in point of fact assembled.

2.1.2 Köhler Illumination

A Köhler illuminator has been assembled as bright field illuminator. To belong to this class of setup, an illumination system must be such that the source plane is a Fourier plane with respect to the sample plane as shown in Fig. 2.1.

By convention, each of these three lenses can be referred to with a proper name, in particular they are called collector lens, for the lens which is the closest to the lamp ; base lens for the lens that stands in an intermediate position between light source and sample (f_{base}); condenser lens, which converges light onto the sample (f_{cond}). In the majority of cases, the illuminated area on the sample is determined by either a field stop or by the base lens diameter; at a practical level, the former is the most implemented since it is much more flexible in term of illumination area setting. Furthermore, in order to maintain a known magnification of the

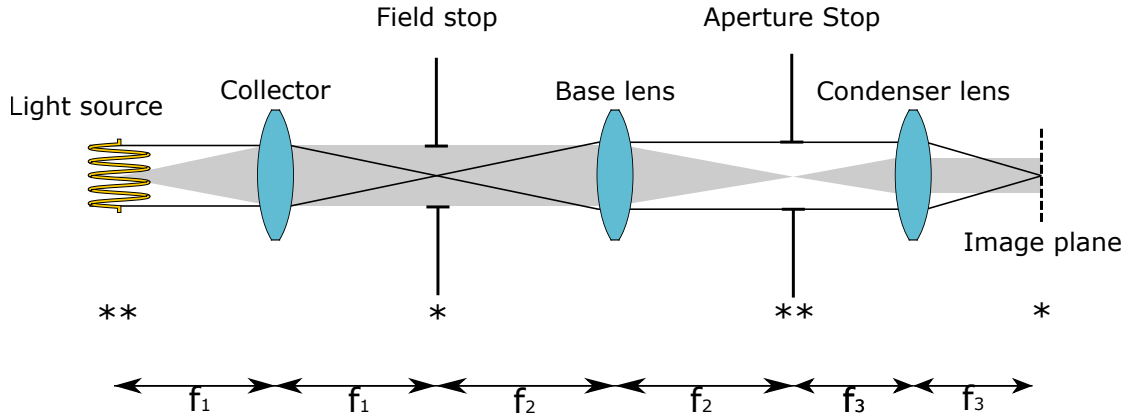


FIGURE 2.1: Köhler illumination standard setup. Same symbols indicates conjugated planes.

illumination beam equal to $M = -\frac{f_{cond}}{f_{base}}$, the condenser and the base lenses are arranged in a $4f$ configuration, such that the aperture stop is found to be at the Fourier plane of both base lens and condenser lens, in a plane usually referred to as the back focal plane of the condenser lens.

For the sake of simplicity, for an analysis of the setup in Fig. 2.1, the whole system will be divided into a series of three smaller parts, that are, starting from the source: a single lens (collector lens) with a field stop, a $2f$ system in between the field and the aperture stop, and yet $2f$ system with the condenser lens at its center. Usually, the latter is characterized by a smaller length since $f_{cond} < f_{base}$. Before proceeding with our analysis, a new quantity called optical throughput has to be defined. It is called throughput of an optical system the product between the pupil area (A_0) and the solid angle coupled to the pupil (Ω_0) through the window area (A_1). Let us now consider the simple situation displayed in Fig. 2.2, given that the solid angle subtended by an aperture of a given area A , with a certain angular aperture and at a certain distance d is $\Omega = \frac{A}{z^2}$, the throughput of a two aperture subsystem is

$$G = \frac{A_0 A_1}{z^2} = A_0 \Omega_0 = A_1 \Omega_1 \quad (2.1)$$

with the system throughput depending only on the system parameters such as the two aperture areas A_0 and A_1 , their distance and with the constraints of an

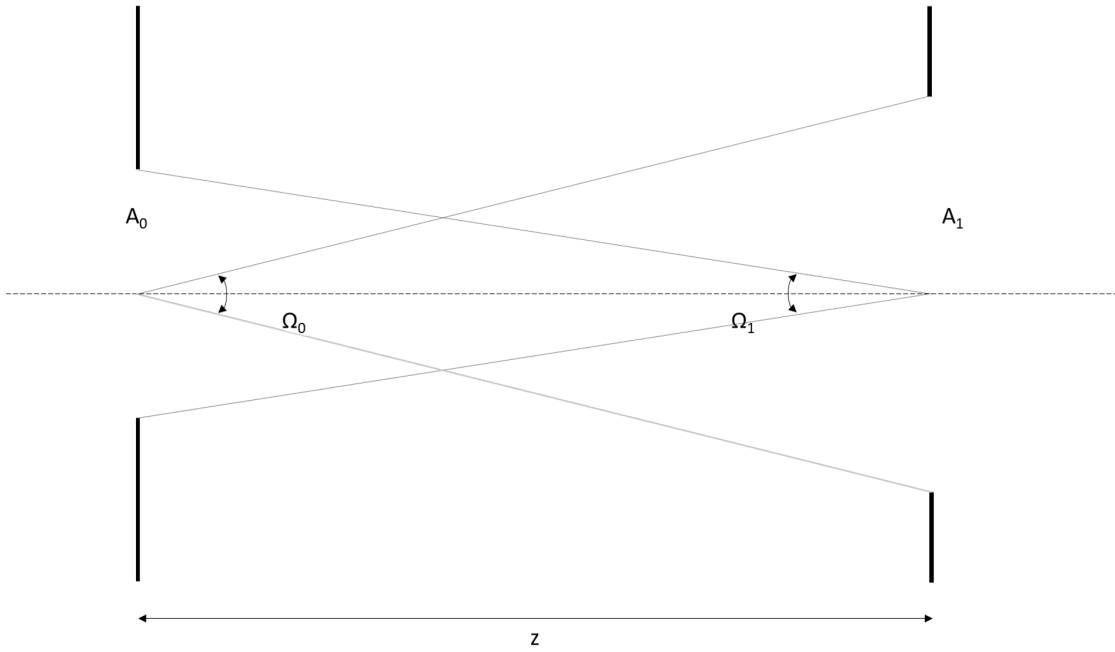


FIGURE 2.2: Throughput calculation for a two apertures system

incoherent, large light input beam. Let us now go a step further and consider a slightly more complicated system as the one shown in Fig. 2.3.

For a symmetric $2f$ system, $z = 2f$ and therefore the throughput is given by

$$G = \frac{A_0 A_1}{f^2}. \quad (2.2)$$

At this point, to ease the analysis of the illumination performance of the system we can divide the latter into smaller, simpler parts and examine one at a time. Following this reasoning, it is found that a Köhler illuminator throughput is

$$G = \frac{A_{as} A_{fs}}{f_{base}^2}, \quad (2.3)$$

meaning that, notwithstanding the change of configuration, at the sample plane the two geometries exploit equal illumination area, convergence angle and power distribution [1].

To the aim of this project, the Köhler illumination geometry has been used, due to the fact that the conjugation between the sample plane and the aperture field

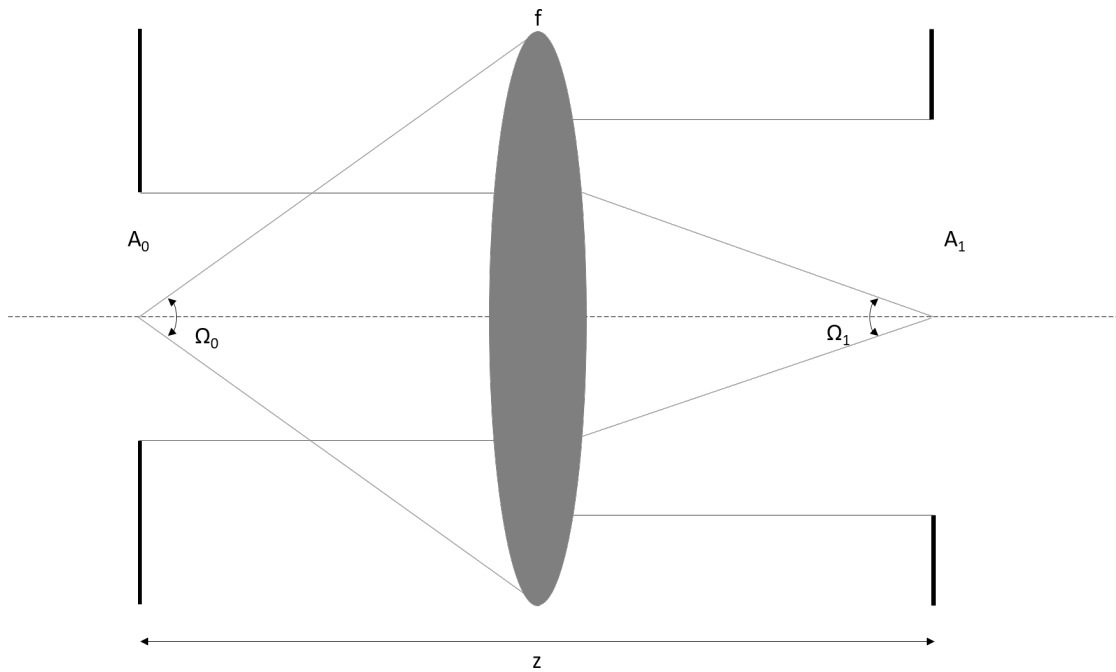


FIGURE 2.3: Throughput calculation for a system made by two apertures at a distance $2f$, with a lens of focal f in the center.

stop plane allows the user, once installed a settable iris in place of a fixed diameter aperture, to regulate at desire the illumination intensity and, with the help of another iris, to analogously set the illumination area by opening or closing the aperture iris, since it is placed in the back focal plane of the condenser lens.

Summing up, a Köhler illuminator guarantees an even illumination of the specimen, resulting in higher contrast images and reducing artifacts. Furthermore, by opening or closing the aperture stop, it can be set the image contrast together with the depth of field of the illumination, by modifying the input NA to the condenser. By adjusting the field stop area instead, due to conjugation of its plane with the sample plane, it can be set the FOI, increasing or decreasing the illuminated area of the sample.

2.1.3 Light Sheet Illumination

As already presented in the previous chapter, the idea standing behind light sheet fluorescence microscopy is to excite fluorescence in the sample, thanks to a laser

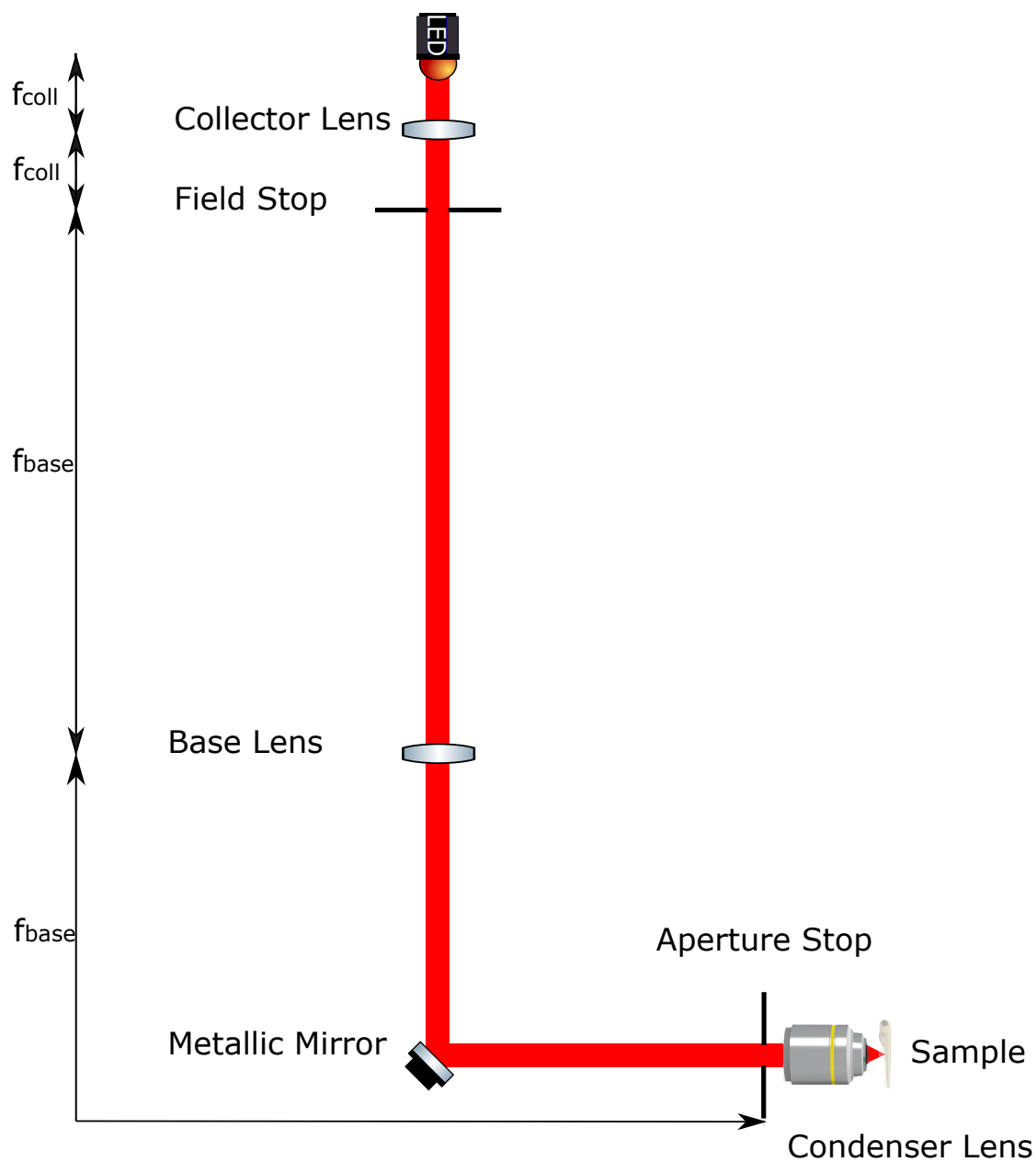


FIGURE 2.4: Köhler illumination setup implemented.
In the figure are not reported the distances equal to f_{cond} , since, in a scaled diagram, it results too small with respect to f_{base}

sheet coming to its side, only in a well determined volume (since the sheet is some μm thick), around the detection optics ideal focal plane. Ideally, the illumination path product would be a two dimensional light sheet impinging exclusively onto the illumination objective back focal plane. This is not achievable in reality, so that it should be preferable to have a sheet of course as thin as possible, but also as uniform as possible over the field of view determined by the optical objective. Light sheet generation is most likely to happen thanks to the use of cylindrical optics [19], which are nonetheless affected by Abbe's diffraction limit, limiting the minimum thickness achievable depending on the illumination beam wavelength and the optics numerical aperture. After having encountered on its path a cylindrical lens, the light beam converges in a distance determined by the lens focal in the direction of the sample and then rapidly diverges away. Since the persistence of the minimum beam waist is limited, to achieve symmetrical excitation volume the center of the sheet is overlying the center of the specimen and therefore of the field of view. Depending on the excitation spectrum of the fluorophores implied, on the optics used and on the sample to investigate, different light sheet thicknesses are made, varying from a minimum of 1 μm , to a maximum of 10 μm [19]. Other methods of light sheet generation have been investigated, but to the aim of this project, the latter approach will be exploited since it guarantees a faster image acquisition and lower photodamages to the sample [20].

For what has been said in the first chapter, the light sheet thickness affects the system optical sectioning capability of the system, also defining the axial resolution of the system. In a normal widefield microscope the axial resolution (referred to as depth of field), is given by

$$DOF = \frac{n\lambda}{NA_{det}^2}, \quad (2.4)$$

with λ being the emission beam wavelength and NA_{det} the numerical aperture of the detection lens (see Paragraph 2.1.5 for more details). Due to the presence not of the simple NA but of its square, axial resolution tremendously suffers from

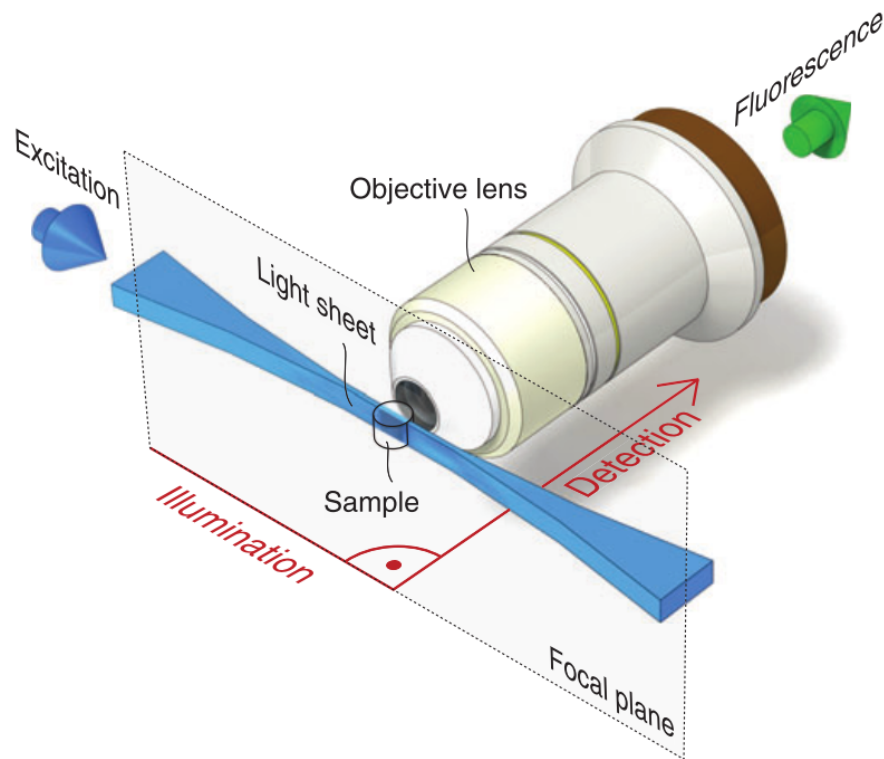


FIGURE 2.5: Light sheet generated in a typical SPIM setup. Light sheet excites fluorescence in a very well determined plane centered with the FOI of the objective lens, so that illumination and detection paths are orthogonal to each other [19]

low numerical aperture detection objectives, hindering optical sectioning. Anyway this problem can be bypassed thanks to light sheet illumination: this technique provides a limited volume illumination, increasing axial resolution in a significant way [11]. According to chapter 1, the axial resolution of the system is given by the beam waist of the laser beam

$$R_A \simeq \frac{\lambda}{2NA_{ill}}. \quad (2.5)$$

2.1.4 Detection

Let us now address our attention to lateral resolution. This, has been said to be equal to

$$R_L = \frac{\lambda}{2NA_{det}}, \quad (2.6)$$

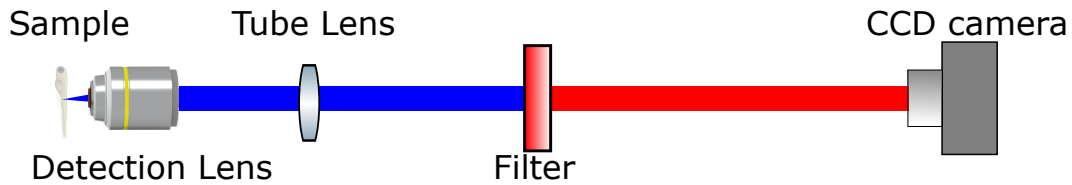


FIGURE 2.6: General detection scheme for fluorescence microscopy. In the detection path a filter has to be inserted in order to cut out the excitation photons that might be reflected and transmitted into the sensor.

being determined again by the NA of the detection objective and by the beam wavelength, analogously to epifluorescence microscopy, not leading to any improvement in resolution. Eq. 2.6 is in accordance to Abbe limit, furthermore it is the same resolution as for a normal widefield microscope.

In Fig.2.6, a typical detection setup for fluorescence microscopy is shown. As depicted, it consists in an objective, a tube lens and a camera (usually a charge coupled device camera) to enable fast image acquisition. On top of that, a single channel detection subsystem is shown, even if due to its characteristics SPIM suits multicolor acquisition. To exploit the latter, a dichroic mirror as well as other filters and cameras are needed, in a number equal to the number of colours to detect. Also an additional bright field path can be implemented as described in 2.1.2 to watch over the sample health and overall status. Another simpler way to exploit multichannel acquisition is to use a filter wheel coupled with a single camera. In this project, single colour acquisition is exploited.

2.1.5 Numerical Aperture and Depth of field

Axial resolution is determined by the detection objective numerical aperture. Their relation imply that to high NA corresponds a low axial resolution and vice versa, as depicted in Fig. 2.7. Due to terminology, one may think that image plane corresponds to a geometrical 2 dimensional plane with no extension along the optical axis but in reality, even in the condition of ideal optical elements (therefore no aberrations of any kind), each point of the image gives rise to a diffraction pattern which extends about the source point itself.

Axial resolution in reality is not simply defined by the wave optics but it is also

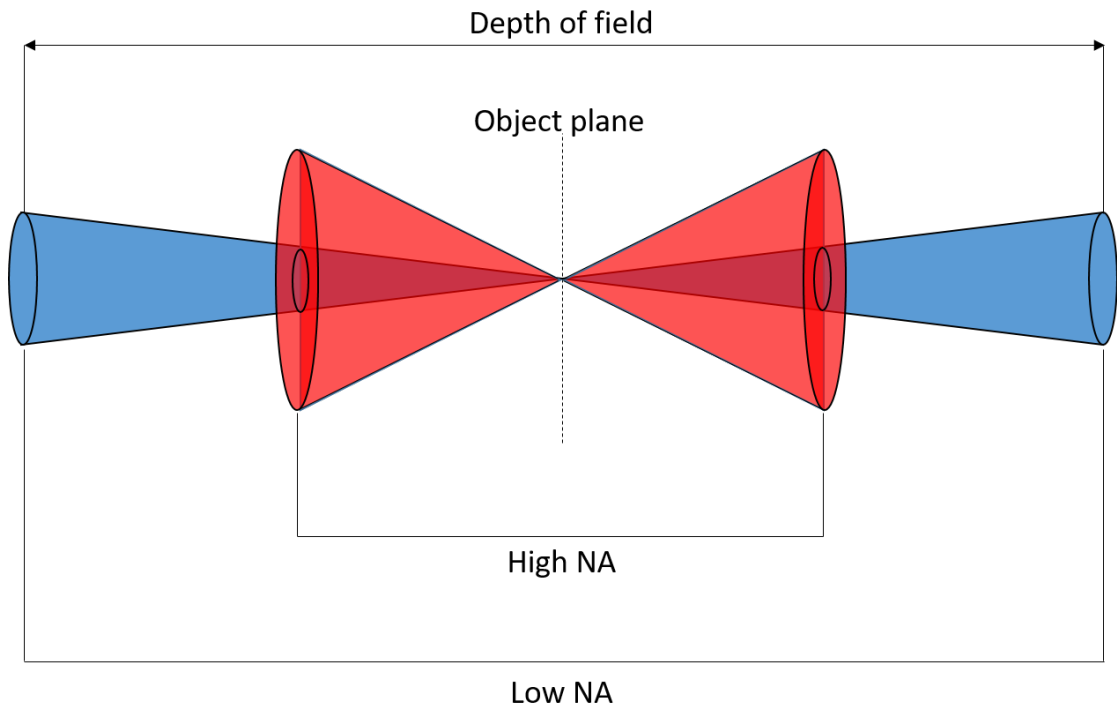


FIGURE 2.7: Depth of field variation at different numerical apertures.

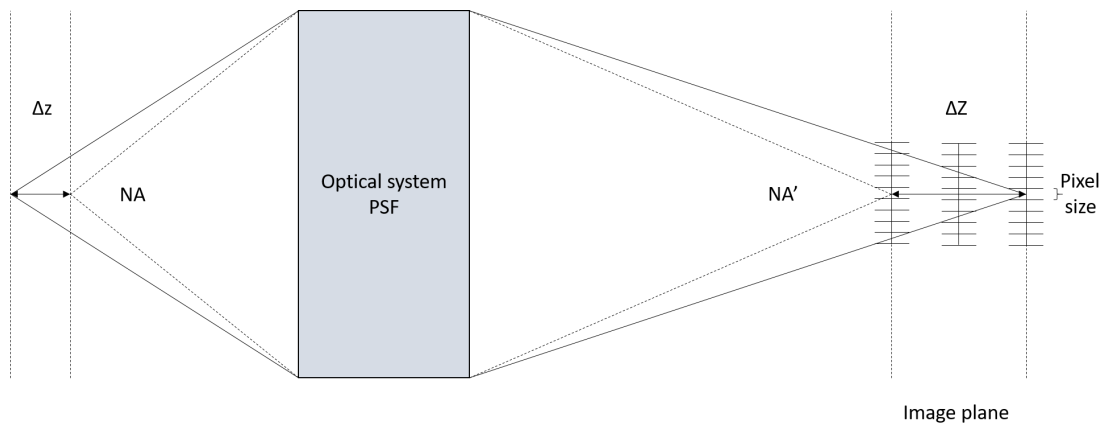


FIGURE 2.8: Depth of field and depth of focus variation. Here Δz is the depth of field, ΔZ is the depth of focus, NA the numerical aperture of the objective lens, NA' the numerical aperture of the tube lens, M the magnification and e the detector pixel length.

determined by the detector geometrical factor. This two components are respectively predominant at high and low numerical aperture, as it is described by the formula

$$DOF = \frac{n \cdot \lambda}{NA^2} + \frac{n}{M \cdot NA} e, \quad (2.7)$$

with DOF being the depth of field, λ the light wavelength, NA the objective numerical aperture, M its lateral magnification and e the smallest resolvable distance by the detector [21].

2.2 Implementation of the Experimental Setup

In the end of the first chapter, different approaches were presented to expand the depth of field of an imaging system; in this work this has been achieved thanks to the mean of dynamical optical elements, such a galvanometric mirror and an elettrotunable lens (ETL). All of what has been said in the previous sections about bright illumination, illumination for fluorescence excitation and detection subsystem has been then applied and such subsystems have been all put together on an optical table; in this section an overview of the developed SPIM setup is given, presenting its theoretical features such as maximum light sheet displacement on the optical axis such that correct imaging is still possible thanks to elettrotunable lens change of shape.

With respect to a standard LSFM setup, as the one shown in 2.6, few changes were made in order to guarantee the ETL and the galvanometric mirror the correct working conditions. In particular, to avoid to introduce optical coma due to the fluid inside of it, the ETL must be hold in the detection path with its principal plane parallel to the optical table. In addition, in the illumination subsystem, a 4f lenses configuration has to be inserted to assure telecentricity of the illumination sheet, i.e. beam waist in the same plane for different angular position of the input beam, as shown in Fig. 2.9.

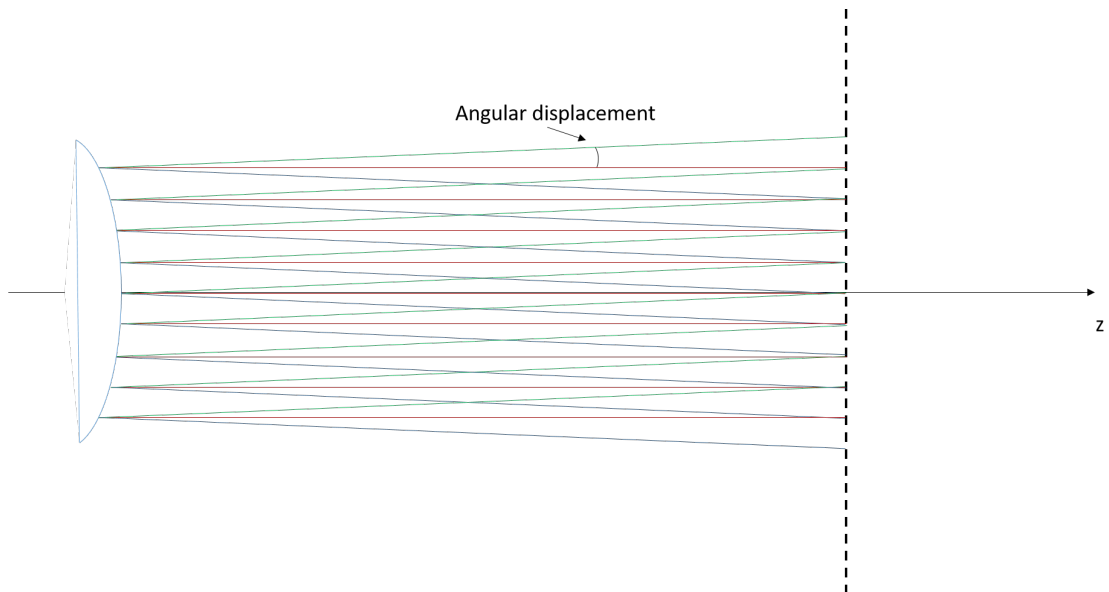


FIGURE 2.9: General view of a telecentric system. Despite the input angular displacement, all of the light rays coming from the principal lens plane are focused on the same plane.

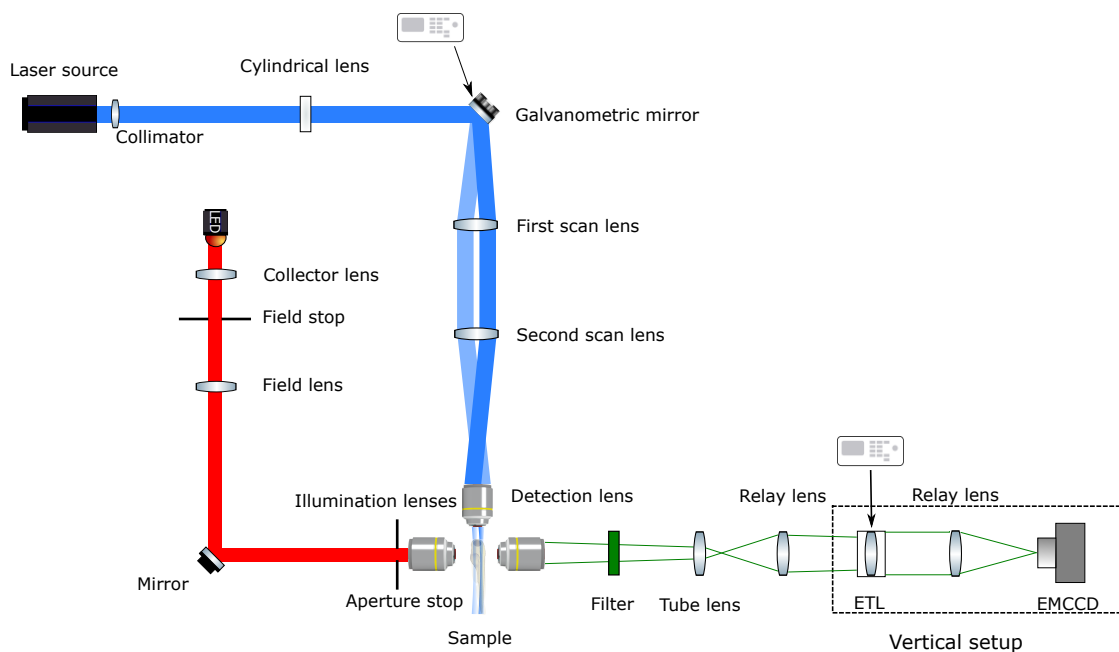


FIGURE 2.10: Whole SPIM setup, including bright field illumination. The light sheet is formed thanks to the laser source and the cylindrical lens which focuses the beam, with the help of a $4f$ system, onto the back focal plane of the illumination objective. The scanning is performed thanks to a galvanometric mirror, a motorized mirror controlled by a DAQ board, which makes imaging on subsequent planes possible. This is achievable with an element that can modify its optical properties such as optical power, ETL lens, which is placed in the vertical part of the setup (contained in the dashed area). This 90° rotation is exploited through a one inch mirror, which is not displayed in figure.

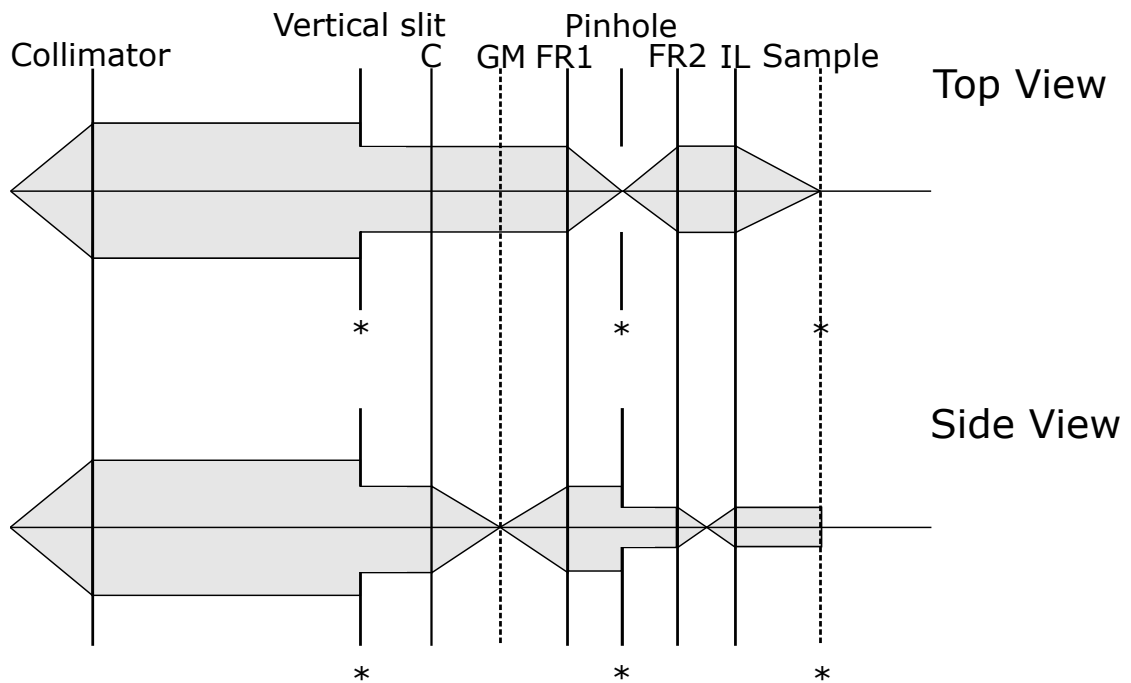


FIGURE 2.11: Top and side view of the light ray bundle in the illumination path. The cylindrical lens that provides focusing into one direction is here indicated with C, while the galvanometric mirror is pointed out with GM. In this figure the final setup is shown, also illustrating the position of the pin hole and the vertical slit added in the end of the project to control the thickness of the light sheet and its vertical dimension. FR1 and FR2 respectively indicate the first and the second scanning relay lens, while IL stands for illumination objective. The symbol "*" shows the conjugate planes in the optical illumination path.

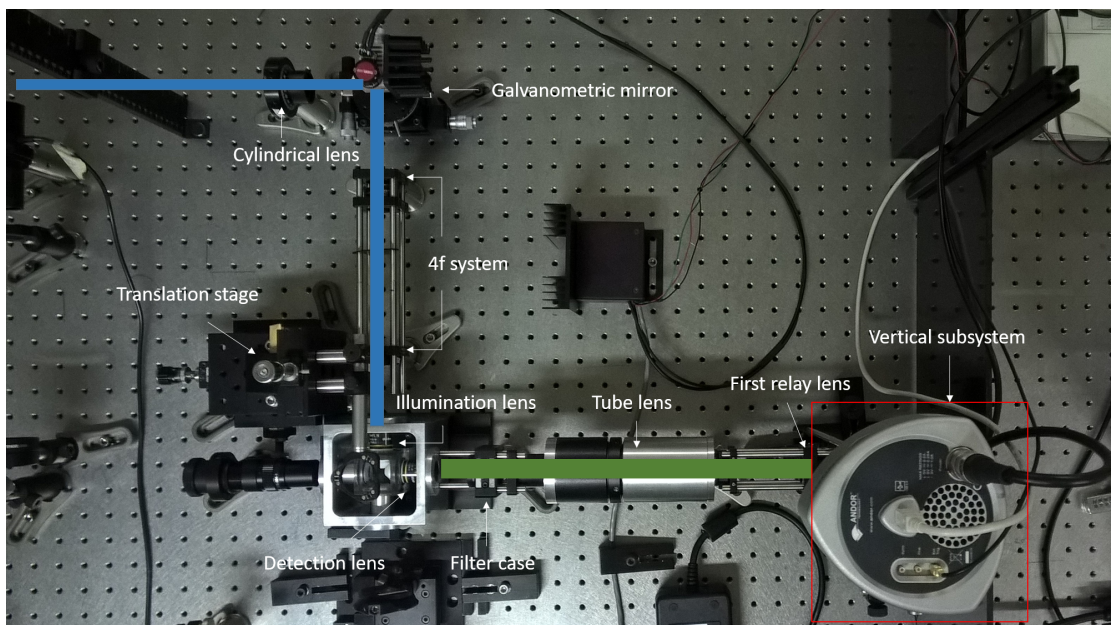


FIGURE 2.12: SPIM setup implementation. In blue and green can be found respectively the excitation beam and fluorescence signal. In the red square is contained the vertical part of the system, containing the elettrotunable lens.

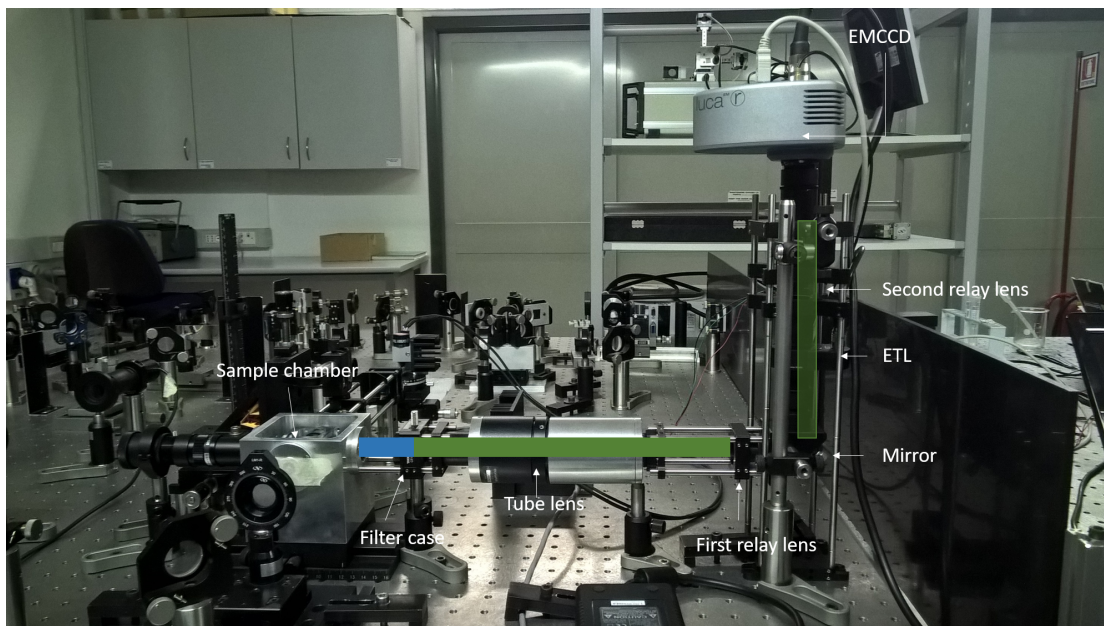


FIGURE 2.13: Vertical subsystem. In green it is shown the detected fluorescence signal.

The setup begins with a blue laser diode emitting at 442nm (MDL-III-442,PSU-A-D), which is, after a brief propagation in a single mode fiber, collimated by a short focal lens ($f=15\text{mm}$). The collimated beam then propagates and impinges on the cylindrical lens (LJ4878RM) mounted on a rotating support (Newport RM25A), to form a line onto the galvanometric mirror (Thorlabs GPS011). This laser diode will be used in this thesis work to excite molecules such as Cyan Fluorescent Protein (CFP) [22] or Green Fluorescent Protein [23], that will be used to mark different samples such as Arabidopsis Thaliana or Zebrafish. The mirror plane is conjugated with the sample chamber; in particular the rest position of the mirror should be such that the light sheet illuminates a plane which is in focus with respect to the camera, with the ETL lens turned off. This conjugation between the motorized mirror and the sample chamber is done with a $4f$ system, as shown in Fig. 2.12. The lenses constituting this $4f$ system have focal $f=75\text{mm}$ (AC254-075-A). After the $4f$ system, excitation light is collected by the illumination lens, an optical objective provided by Mitutoyo, 10X for immersion imaging and suited for long working distances (Olympus Water Immersion Plan Apo Infinity Corrected Long WD Objective).

For what it concerns the detection side, once got out the sample chamber, the

radiation travels along the path shown in green in 2.12, before entering a low pass filter to separate the fluorescence signal from the reflected excitation light it is collected by a detection objective twin with the illumination lens. After being filtered, light travels through a tube lens coupled with the detection lens such that the output magnification is known. After this stage, the fluorescence signal is collected by a 4f system made by two achromatic lenses of $f=100\text{mm}$ (Thorlabs AC254-100-A-ML). With the term achromatic is intended a lens (or a doublet) which is corrected with respect to chromatic and spherical aberrations. At a distance $2f$ from the input plane of the 4f system, an ETL has been placed (Optotune EL-16-40-TC), this plane is in fact a conjugate of the back focal plane of the detection objective. All of the lenses previously mentioned have a diameter of 1 inch and are treated with anti reflection coating in the range going from 400-700nm.

What has not been mentioned but is clearly shown in Fig. 2.12 and Fig. 2.13 is that in between the two relay lenses in the detection path a mirror has been mounted to rotate the symmetry axis of the system by 90° . As specified by its manual, the Optotune lens must be mounted on a horizontal plane in order to avoid strong gravity induced coma (Fig. 2.13).

The focal length of the elettrotunable lens determines the position of plane imaged onto the sensor, therefore, since the lens can vary its optical power from -2 to 3 dpt (where a $[\text{dpt}] = [\frac{1}{m}]$), this will lead to a range of different plane that can be conjugated to the imaging sensor plane. In the next subsection, it will be calculated the maximum displacement of the input plane.

For what it concerns the Köhler illuminator, the first lens on the optical axis after the light source has a 1 inch diameter and a focal length of 25 mm and it is treated with AR coating in the range 400-700 nm (LA1951-D - N-BK7); the field lens instead has a 2 inches diameter to collect as more light as possible (for the first lens this was not necessary due to its proximity with the light source), a $f=200\text{mm}$ with same AR coating (AC508-200-A-ML).

Once put everything mentioned before on the optical table, further modifications were made in order to the user to be in control of the light sheet persistence length

and shape. This has been performed in an analogous way as the one shown for the Köhler in 2.1.2. The persistence length control has been obtained with the mean of a pin hole in a plane before the cylindrical lens: in this region in fact the laser beam is collimated, so that every plane has no particular optical properties; with a pin hole in such a region, by opening and closing it, it can be controlled the diameter of the beam impinging onto the motorized mirror, yet modifying the input NA to the illumination objective and therefore, from what it has been said in chapter 1, modifying the light sheet persistence length; decreasing the NA in fact makes the minimum beam waist persists over a longer length along the optical illumination axis. Finally another pin hole has been placed in the focus of the 4f system displayed in 2.12, so that it is possible to cut higher spatial frequency components along the collimated direction and therefore reducing the vertical length of the light sheet at the sample plane, but yet keeping unperturbed the persistence length (the input NA in this case remains untouched).

2.3 System imaging and optical characteristics

2.3.1 Scanning range

In this subsection it will be derived the maximum imaging range given by a lens of variable focal length, placed in the middle of the detection telescope, as displayed in Fig. 2.10. This calculation will be performed in the optical matrix formalism [24], in which to every optical element such as lenses or free propagation, it corresponds a 2x2 matrix describing the relation between the input and the output system rays:

$$\begin{pmatrix} y_0 \\ \alpha_0 \end{pmatrix} = M \cdot \begin{pmatrix} y_1 \\ \alpha_1 \end{pmatrix}, \quad (2.8)$$

where the pedices 0 and 1 indicate the input and output rays respectively, and M the matrix correspondent to the system taken in exam. This matrix M, for a complex optical system made by several elements, is given by the multiplication of

the single elements matrices, in an order that is opposite to the light propagation direction, i.e. starting from the output plane and going backward to the input plane. From the M matrix of a certain system, several informations are available:

$$M = \begin{pmatrix} A & B \\ C & D \end{pmatrix}, \quad (2.9)$$

so that

$$\begin{pmatrix} y_0 \\ \alpha_0 \end{pmatrix} = \begin{pmatrix} A & B \\ C & D \end{pmatrix} \cdot \begin{pmatrix} y_1 \\ \alpha_1 \end{pmatrix}. \quad (2.10)$$

From eq. 2.10 and the related system of equations, it can be retrieved for example the magnification of the optical system through the matrix element A; in fact, defining the magnification as the ratio of the input and output position, if the coefficient B=0 then A is exactly equal to this ratio. The simplest optical elements, which are also the only elements used in these calculations, are described by the following optical matrices:

$$M = \begin{pmatrix} 1 & L \\ 0 & 1 \end{pmatrix}, \quad (2.11)$$

for simple in air translation, and

$$M = \begin{pmatrix} 1 & 0 \\ -\frac{1}{f} & 1 \end{pmatrix}, \quad (2.12)$$

for a thin lens with focal length f. On top of that, the determinant of every optical matrix, whether it describes a single element or a complex system, equals the ratio of the input and the output refractive index

$$Det(M) = AB - CD = \frac{n_0}{n_1}; \quad (2.13)$$

in particular this property will be exploited in the effective imaging range, since the fluorescence signal at first place travels through distilled water (n=1.33), for then being detected in air (n=1).

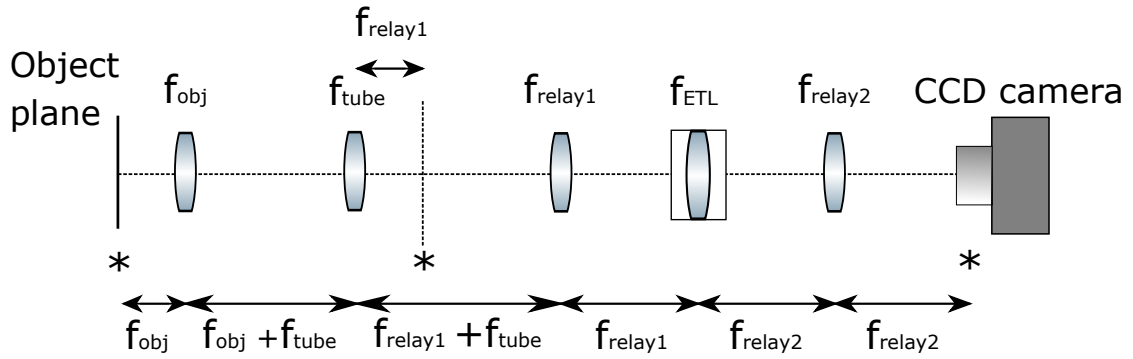


FIGURE 2.14: Detection schema where conjugated planes are highlighted. In this example schema, the two relays lenses are taken with equal focal length.

Let us now retrieve the maximum imaginable displacement from the centered position. This capability to image different planes of course is a property of the detection system, that has been already analyzed in section 2.2. Its schema is shown in Fig. 2.14. Whereas in Fig. 2.14 it is shown a situation where the two relay lenses have the same optical power, in the following calculation it will be considered a generic case where no assumption on the focal lengths is taken. As previously said, a complex optical system is represented by a matrix that is the product of the single elements matrices starting from the sensor and going backward; with this in mind, we start from the last optical element (i.e. the free propagation of length f_2) and we perform multiplication 2 by 2.

$$\begin{pmatrix} 1 & f_2 \\ 0 & 1 \end{pmatrix} \cdot \begin{pmatrix} 1 & 0 \\ -\frac{1}{f_2} & 1 \end{pmatrix} = \begin{pmatrix} 0 & f_2 \\ -\frac{1}{f_2} & 1 \end{pmatrix}, \quad (2.14)$$

for the last in air propagation and lens. Considering the second f_2 long propagation, we have an optical matrix that is equal to

$$\begin{pmatrix} 0 & f_2 \\ -\frac{1}{f_2} & 1 \end{pmatrix} \cdot \begin{pmatrix} 1 & f_2 \\ 0 & 1 \end{pmatrix} = \begin{pmatrix} 0 & f_2 \\ -\frac{1}{f_2} & 0 \end{pmatrix}. \quad (2.15)$$

We now encounter on the optical axis the elettrotunable lens, which is indicated as a thin lens with known focal length f_{etl}

$$\begin{pmatrix} 0 & f_2 \\ -\frac{1}{f_2} & 0 \end{pmatrix} \cdot \begin{pmatrix} 1 & 0 \\ -\frac{1}{f_{etl}} & 1 \end{pmatrix} = \begin{pmatrix} -\frac{f_2}{f_{etl}} & f_2 \\ -\frac{1}{f_2} & 0 \end{pmatrix} \quad (2.16)$$

$$\begin{pmatrix} -\frac{f_2}{f_{etl}} & f_2 \\ -\frac{1}{f_2} & 0 \end{pmatrix} \cdot \begin{pmatrix} 1 & f_1 \\ 0 & 1 \end{pmatrix} = \begin{pmatrix} -\frac{f_2}{f_{etl}} & -\frac{f_1 f_2}{f_{etl}} \\ -\frac{1}{f_2} & \frac{f_1}{f_2} \end{pmatrix}. \quad (2.17)$$

Keeping on doing the multiplication in the right order, in the end, the last matrix multiplication is the one between the subsystem not including the propagation from the sample to the objective and the latter. On top of that, this last in water propagation is not f_{obj} long but we have to take also into account a further Δz stretch, so that we have

$$\begin{aligned} & \begin{pmatrix} -\frac{f_2 f_t}{f_1 f_{obj}} & -\frac{f_1 f_2 f_{obj}}{f_t f_{etl}} - \frac{f_2 f_t}{f_1} \\ 0 & \frac{f_1 f_{obj}}{f_2 f_t} \end{pmatrix} \cdot \begin{pmatrix} 1 & f_{obj} + \Delta z \\ 0 & n \end{pmatrix} = \\ & = \begin{pmatrix} -\frac{f_2 f_t}{f_1 f_{obj}} & \frac{f_2 f_t}{f_1} (1 - n) - \frac{f_2 f_t}{f_1 f_{obj}} \Delta z + \frac{f_1 f_2 f_{obj}}{f_t f_{etl}} n \\ 0 & \frac{f_1 f_{obj}}{f_2 f_t} n \end{pmatrix}. \end{aligned} \quad (2.18)$$

with n being the propagation medium refractive index,

$$M_{total} = \begin{pmatrix} -\frac{f_2 f_t}{f_1 f_{obj}} & \frac{f_2 f_t}{f_1} (1 - n) - \frac{f_2 f_t}{f_1 f_{obj}} \Delta z + \frac{f_1 f_2 f_{obj}}{f_t f_{etl}} n \\ 0 & \frac{f_1 f_{obj}}{f_2 f_t} n \end{pmatrix}. \quad (2.19)$$

From 2.10 we have a relation between input and output rays

$$\begin{pmatrix} y_0 \\ \alpha_0 \end{pmatrix} = \begin{pmatrix} -\frac{f_2 f_t}{f_1 f_{obj}} & \frac{f_2 f_t}{f_1} (1 - n) - \frac{f_2 f_t}{f_1 f_{obj}} \Delta z + \frac{f_1 f_2 f_{obj}}{f_t f_{etl}} n \\ 0 & \frac{f_1 f_{obj}}{f_2 f_t} n \end{pmatrix} \cdot \begin{pmatrix} y_1 \\ \alpha_1 \end{pmatrix}, \quad (2.20)$$

so that a relation for magnification is obtained

$$y_1 = \frac{f_2 f_t}{f_1 f_{obj}} y_0 + \left(\frac{f_2 f_t}{f_1} (1 - n) - \frac{f_2 f_t}{f_1 f_{obj}} \Delta z + \frac{f_1 f_2 f_{obj}}{f_t f_{etl}} n \right) \alpha_0. \quad (2.21)$$

In order to have a constant magnification for different angular slopes of the light rays, which is obtained practically with the adaptive lens exactly in the weighted

λ	$\frac{n\lambda}{NA_{det}^2}$	$\frac{n}{M \cdot NA_{det}} e$	$\frac{\lambda}{2NA_{det}}$
440nm	$6.5\mu m$	$3.5\mu m$	$0.73\mu m$
500nm	$7.2\mu m$	$3.5\mu m$	$0.83\mu m$
660nm	$9.7\mu m$	$3.5\mu m$	$1.1\mu m$

TABLE 2.1: Different resolution of the system at different wavelengths. The two rightmost columns regard the two terms that sum to form the detection resolution, while the leftmost column shows the lateral resolution of the detection subsystem.

center of the 4f system, we equal the term multiplied by α_0 to 0. This leads to the following equality, which express Δz in function of all the other characteristic lengths of the system

$$\Delta z = -n \frac{f_1 f_2 f_{obj}}{f_{etl}} \cdot \left(\frac{f_{obj}}{f_t} \right)^2 \cdot \frac{f_1}{f_2}, \quad (2.22)$$

now considering $M = \frac{f_t}{f_{obj}}$ the magnification given by the coupled objective and tube lens, we finally obtain

$$\Delta z = -n \frac{f_1^2}{f_{etl}} \frac{1}{M^2}, \quad (2.23)$$

which is the scanning range also shown by [15]. A final remark is made on the role taken by the second relay lens: this lens in fact plays no role in the imaging range at all despite its value; the only elements that determine the overall Δz are in fact the effective magnification to the square of the system, the elettrotunable lens optical power and the first relay lens focal length to the square.

Finally, considering the optical elements used in this project ($f_1 = 100mm$ and $M = 10$) and the maximum and minimum focal length of the electrotunable lens, we have a total range of $648 \mu m$, whose experimental verification will be exploited in the last chapter.

2.3.2 Specifications of the developed system

In this final part of the chapter, the developed setup will be analyzed in terms of resolution, lateral and axial of each of its parts, taking into account the light sheet

shape as described in Ch 1. In table 2.1, they are calculated both the detection depth of field and the illumination lateral resolution for the two wavelengths used for excitation and brightfield respectively.

As shown in section 2.2, the setup implemented in this thesis work is such that the illumination optical axis and the detection optical axis are perpendicular to each other. This means that the axial resolution of the first overlaps with the field of view of the detection objective and that the illumination lateral resolution extends over the depth of field of the detection subsystem. Without any tunable lens enabling an extension of the detection depth of field, this latter is given by 2.7 which in the built setup takes a value of

$$DOF = \frac{n \cdot \lambda}{NA_{det}^2} + \frac{n}{M \cdot NA_{det}} e = 7.50\mu m + 3.55\mu m \simeq 10.1\mu m, \quad (2.24)$$

considering a detected wavelength of $\lambda = 530nm$. The use of an adaptive element such as the electrotunable lens extends this quantity remarkably up to a value of $648\mu m$, almost sixty times than the previous case.

Let us now consider the numerical apertures of the two paths constituting the setup, i.e. NA_{ill} for the excitation part and NA_{det} ; these two values alone determine most of the optical dimensions of the system. While on the one hand, for how it has been developed, the detection subsystem is such that its numerical aperture is fixed at a value of 0.3, on the other hand the illumination part has been slightly modified from the situation shown in 2.10: in fact before entering the objective, light has to travel through two elements, one slit vertical slit and one iris respectively. These two components have been included in the detection setup so that it is possible to the user to tune the illumination numerical aperture depending on the sample characteristics, therefore modified the light sheet thickness and persistence length, i.e. the spatial extension of the illumination beam.

Gaussian beams, as the one employed in the excitation path, exhibit a persistence length that is shown in eq. 1.70. Intuitively, to perform a good image acquisition, we want that the narrower zone of the beam is centred with the detection objective

and that it overlaps with the field of view of the latter, so that

$$2z_R = \frac{2n\lambda}{NA_{ill}^2} = FOV = e * N; \quad (2.25)$$

with z_R being the Rayleigh length of the beam, e the pixel size and N the number of pixel in one dimension, as it has been shown in eq. 1.72. For this project a camera is used with a single pixel $64\mu m^2$ large, meaning that due to its square shape, the parameter e in the formula 2.7 is $8\mu m$ and made by $1004*1002$ of this pixels. Considering the parameters of the setup, eq. 2.25 gives $NA_{ill} \simeq 0.038 < 0.3 = NA_{obj}$, justifying the presence of the vertical slit before the cylindrical lens. The constraint in 1.70 so is such that a $NA=0.04$ should be used, obtaining to a beam waist of $\frac{\lambda}{2NA_{ill}} = 5.8\mu m$. This long persistence length however may be too extended for small samples, which do not require such a wide FOV; on top of that small NA also affects the intensity of the fluorescent signal, which is critical. To this issue, let us consider the case where instead of taking $z_R = 0.4mm$ (i.e. the full detection FOV), z_R is as long as its half, $0.2mm$. With a Rayleigh length as such, a new NA_{ill} is obtained from $NA_{ill} = \sqrt{\frac{n\lambda}{z_R}} = 0.054$, leading to a beam waist of $4.1\mu m$, which is smaller than the one corresponding to a longer persistence length since higher divergence Gaussian beams imply smaller waist, but shorter persistence lengths. The latter situation, given the samples that are most likely to be analyzed, is how the developed system is expected to work, trading off lateral illumination resolution and illuminated FOV. Let us now calculate the lateral illumination resolution for the case in which maximum aperture is exploited. For a $NA=0.3$ (given by the illumination objective used in the setup), a beam waist of $0.7\mu m$ is achievable; again such a small value imply a Rayleigh length of $0.006mm$, which almost 70 times smaller that the situation where $NA=0.04$, and 35 times with respect to the case where $NA=0.054$. The quadratic dependence to the axial resolution to the NA of the illumination system is such that an improvement factor of 8 ($5.8\mu m/0.7\mu m$) in the beam waist implies a degradation of a factor of 70 in the persistence length of the beam, resulting in the best optical sectioning achievable, but with the smallest part of the sample illuminated.

To conclude the chapter, an analysis on how the light displacement is performed

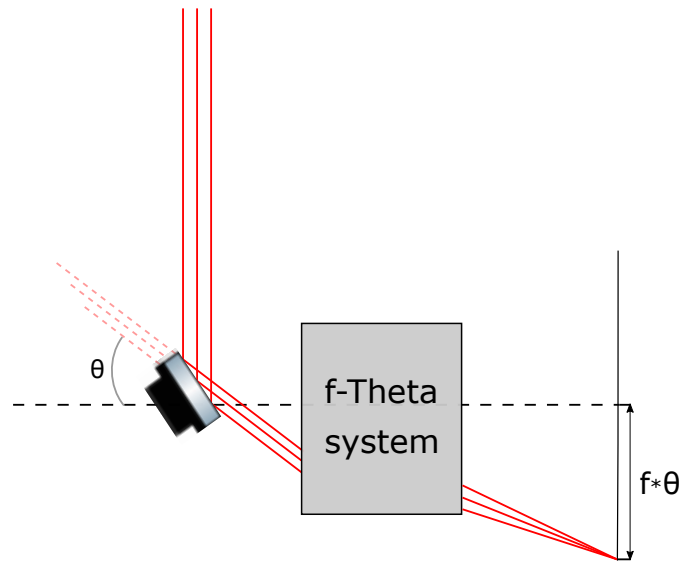


FIGURE 2.15: f-theta system. The off-axis displacement is given by the input slope of the light bundle and the focal length of the system.

at the sample plane is given. This is in fact crucial for the right functioning of the system. A spherical lens focuses light rays with different angular slopes in a surface locus which is not a plane orthogonal to the optical axis. Before the sample chamber, as it is described in section 2.2, it has been implemented a 4f telecentric system that, together with the illumination objective, forms a f-theta system. This family of systems are depicted in Fig. 2.15. F-theta systems are systems that allow to obtain flat image at the sample plane, with a off-axis displacement that is proportional to the focal length of the system and to the input angular slope of the rays. Once reflected by the motorized mirror let us suppose at rest position ($\theta = 0^\circ$), light travels through the f-theta system and impinges onto the sample on the illumination optical axis. When the mirror is rotated, i.e. $\theta \neq 0^\circ$, this implies, as shown in Fig. 2.15, that the light sheet is shifted onto the sample plane by a value of $f * \theta$. From experimental observations, the overall focal length of the f-theta system is $\simeq 14mm$, meaning that to be able to span the known depth of the detection field of $\simeq 650\mu m$, it will be necessary an angular displacement of

$$\theta = \frac{650 \cdot 10^{-6}}{14 \cdot 10^{-3}} * \frac{360^\circ}{2\pi} \simeq 3^\circ.$$

Chapter 3

Software and Acquisition

3.1 Introduction

In this chapter a fully explanation of the software developed to control the whole optical setup and its adaptive and programmable elements, such as a galvanometric mirror and an electrotunable lens, is given. This software in particular exploits a state machine structure, making it simpler to design and understand and therefore easier for the programmer to modify for further implementation. On top of that, the communication protocol used to exchange commands with the lens driver is presented. A final remark is made for what it concerns the correctness of the communication between the national instrument DAQ and the lens driver, for which a cyclic redundancy check code has been implemented.

3.2 Software Environment

LabVIEW (Laboratory Virtual Instrument Engineering Workbench) is a platform for system-design and development environment for a graphic programming language from National Instruments. The choice made is this particular language due to its flexibility in hardware interfacing [25] and its easy reading visual code Labview programming language, named G, is a dataflow programming language,

that means that G written programs are modeled as directional graphs showing the dataflow between different operations. How and when a graphical component is executed is determined by the structure of the block diagram (that's how the LabVIEW-source code can be referred to) on which the programmer connects different blocks (each one corresponding to a specific function) by simply drawing wires. Each of this wire propagates a variable and any block can be executed as soon as all its input variables happen to be available. Since it may occur that multiple block are ready to be executed at a given time, G is such that these blocks (or nodes) can be executed in parallel. Multi-processing and multi-threading hardware is actuated automatically by the built-in scheduler, which multiplexes the several operating system threads over the nodes ready to be executed [26]. On top of that, LabVIEW also integrates the possibility for the programmer to create user interfaces (named front panel). A LabVIEW program-subroutine is called virtual instruments (VIs). For what it has been said, each VI can be divided into three components: a block diagram, a front panel, and a connector panel. The last is used to represent a VI that has been called in another VI's block diagram. The front panel is built using control parameters and indicators. Control parameters are the inputs: they permit the user to supply information to the VI. Indicators are the outputs: they display or simply take the value of the results given by the VI for given inputs. The back panel, which is a block diagram, encloses the graphical source code. All of what is placed on the front panel will translated as terminal in the back panel. The back panel also contains structures and sub-blocks which perform operations on control parameters and supply data to indicators. The structures (like loop structures as well as case structures) and functions can be found in the Functions palette and can be easily placed by the user on the back panel.

3.2.1 Device interface

LabVIEW includes extensive support for interfacing to devices, instruments, cameras, and other devices. Users interface to hardware by either writing direct bus

commands (USB, GPIB, Serial) or using high-level, device-specific, drivers that provide native LabVIEW function nodes for controlling the device. Labview offers the user the possibility to download packages to ease the interface with wide usage hardware platforms such as NI-DAQs or Arduino, but to the aim of this project, these packages were not used since despite facilitating the coding, they critically slow the compiling stage and since speed is one of the crucial factor of the whole project, they were not considered.

3.2.2 Code Compiling

LabVIEW includes a compiler that produces native code for the CPU platform. The graphical code is translated into executable machine code by interpreting the syntax and by compiling. The LabVIEW syntax is strictly enforced during the editing process and compiled into the executable machine code when requested to run or upon saving. In the latter case, the executable and the source code are merged into a single file. The executable runs with the help of the LabVIEW run-time engine, which contains some precompiled code to perform common tasks that are defined by the G language. The run-time engine reduces compiling time and provides a consistent interface to various operating systems, graphic systems, hardware components, etc. The run-time environment makes the code portable across platforms. Generally, LabVIEW code can be slower than equivalent compiled C code, although the differences often lie more with program optimization than inherent execution speed.

3.3 Tools

3.3.1 Electotractable Lens: Optotune EL-16-40-TC

EL-16-40-TC is a adaptive lens made by a polymer that can change its shape by applying an electric current, so that with the change of shape its optical power is

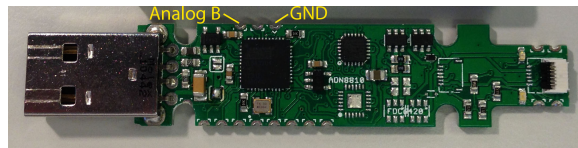


FIGURE 3.1: Lens driver without its cage.

controlled within milliseconds over a diopter range of -2 dpt to $+3$ dpt. A major attribute of this shape changing lens is the clear aperture of 16 mm.

Among the many available operation mode, an Analog signal reading is built into the firmware, through a wire connection with pin B (3.1), given that the analog voltage of the input signal lies between 0 V and 5 V. The ADC has a resolution of 10 bit and therefore the digital signal belongs to the interval 0,1023. It is also available a communication protocol in case a customized software is written, protocol that can be implemented using any programming language. For this project, Labview is used.

Connection

The Microcontroller used runs a virtual com port driver provided by Atmel. The connection settings are:

- 1) Parity: None
- 2) Stop Bits: One
- 3) Data Bits: 8
- 4) Baudrate: 115200 (others may also work since the port is virtual)

Handshake:

The handshake command is used to check if the hardware is ready and running. It can also be used as a reset function as it will reset the current to zero. As said before, several operating modes are available.

3.3.2 Galvanometric Mirror: Thorlabs GVS001

Galvanometric mirrors are tools widely employed in context such as laser etching, imaging, cofocal microscopy or light sheet microscopy. A galvanometer is a precision motor with a limited scan range, usually some degree, whose acceleration

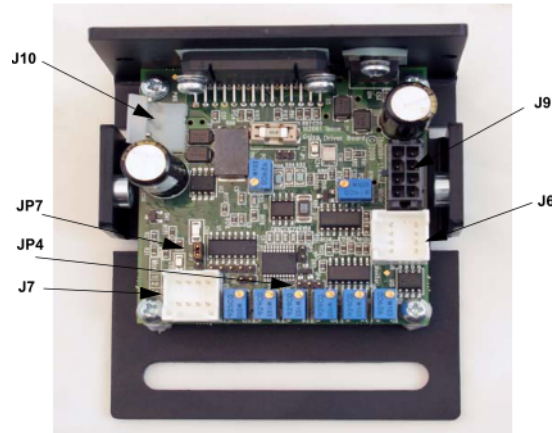


FIGURE 3.2: Galvanometric mirror driver without its cage. With arrows are highlighted the different driver components:

J10: power connections;

J9: 8 pins connector for diagnostics, here it is accessible the mirror position sensor;

J7: 8 command Input Connector Pin Identification;

J6: diagnostics Connector Pin Identification;

JP7: scaling factor selection port, here thanks to a jumper, the user can select among three different scaling factor.

is directly proportional to the current applied, through the driver, to the motor. By stopping the current abruptly, the motor comes to rest thanks to friction; by applying a reverse polarity current instead, motion of the motor shaft can be instantly blocked.

Different scaling factor from current to angular displacement can be chosen among $1V/^\circ$, $0.8V/^\circ$ or $0.5V/^\circ$ depending on the desired scanning range; to the aim of this project, $0.8V/^\circ$ conversion factor is selected by simply putting a jumper in the suitable port in the mirror driver, in particular in the port JP7 shown in Fig. 3.2. A scale factor of $0.8V/^\circ$ assures a mirror scanning range of $\pm 12,5^\circ$, corresponding to a $\pm 5V$ input. Typically, users will deploy a DAQ card with DAC analogue outputs in order to drive the servo drivers supplied with the galvanometric mirror. The minimum specifications for the DAC outputs are: bipolar $-10V$ to $10V$ DAC differential analogue output channels. DAC internal clock frequency higher than $20kS/s$, 16 Bit DAC resolution and low out impedance ($\leq 50 \Omega$). For the above mentioned required characteristics, it was decided to use a NI USB 6221, described in particular in the following section.

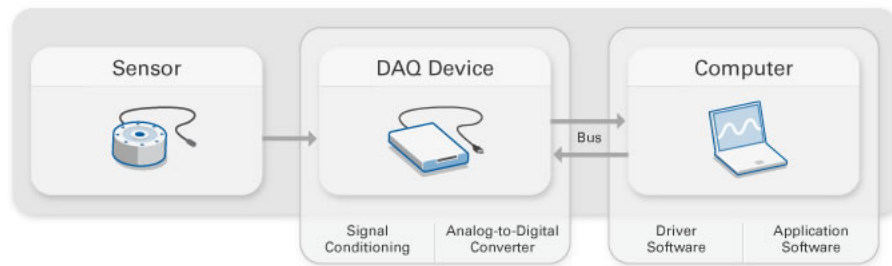


FIGURE 3.3: DAQ working scheme.

3.3.3 DAQ: National Instrument USB 6221

The generation of the analog signals and the together with the trigger signal are generated thanks to a programmable board produced by National Instrument called NI-USB 6221. DAQ hardware acts as an interface between the computer and the signals from the outside world. It functions as a system that digitizes the incoming analog signals so that the computer can interpret them. The three basic components of a DAQ device are: a signal conditioning circuit, an ADC (analog-to-digital converter), and a computer bus. Many DAQ devices include other functions for automating processes and measurement systems. For example, DACs generate analogue signals, digital I / O lines allow digital signal input and output and counters / timers count and generate digital pulses. In particular, NI USB-6221 offers up to 80 analog, 16 bits inputs at 250kS/s, 4 analog outputs with same resolution at 833kS/s and an internal 80MHz clock, which is critical for internal tasks synchronism. This board can be programmed in several languages, like C++, Matlab or Labview; due to the fact that both Labview and NI-USB 6221 are products of the National Instrument, they are easily interfaceable.

3.3.4 Electron Multiplier CCD: Luca-r

An Electron Multiplying Charge-Coupled Device is an image sensor capable of detecting single photon events without an image intensifier such as active multiplication tubes; this is achievable thanks to a built-in structure mounted into the chip. EMCCD cameras overcome the common constraint of obtaining high

sensitivity at high speed frame transfer. Traditional CCD cameras can offer high sensitivity, with readout noises in a single frame less than $10e^-$ but at an expense of long readout time. That is why they are usually referred to as 'slow scan' cameras. This readout constraint implicitly comes from the charge amplification mechanism into a CCD sensor. High speed operations is what is wanted to be achieved. In order to do this, the bandwidth of the charge amplifier has to be as wide as possible: since for the readout phase the noise scales with the operational bandwidth, fast amplifiers also suffer from higher noise. A slow scan CCD has relatively low bandwidth to lower noise and therefore can only be read out at low speeds usually less than some mega Hertz. EMCCD cameras by-pass this speed limit by amplifying the charge signal before the charge amplification stage and hence obtain sensitivity never met before at high speeds. With such a signal amplification, readout noise is no longer a limit on sensitivity. To the aim of this project, the Luca-r model EMCCD was used. The upper is an EMCCD with 1004×1002 pixels, each of them with a $8\mu m \times 8\mu m$ surface, digitized on a 14 bit level. This camera guarantees a maximum frame rate of 12 Hz, with a maximum read out rate of 13,5 MHz, with a readout noise of the above mentioned range (tens of electron at 13,5 MHz). The Luca-r can be easily control through a software called Andor Solis; this software offers optimized acquisition control and analysis functionality. With the help of Andor Solis, the user can control every parameter involved in the acquisition (acquisition time, EM gain), together with other parameters correlated with the collection of stacks of images and external triggered operations. External triggered operations is what this camera was used for: the software developed for this project in fact only deals with the generation of the trigger to send to the camera. Once the external trigger cable is connecting the signal provider (the NI DAQ) and the Luca-r, everything is set for the images acquisition, given that the right operation mode is selected in the Solis software. The selected acquisition mode was such that, after a trigger event, the camera takes as much images as desired, with a given exposure time (time for each image to be taken) and a given kinetic cycle (time to wait from one acquisition to the following). Together with the acquisition mode, a trigger mode has to be selected

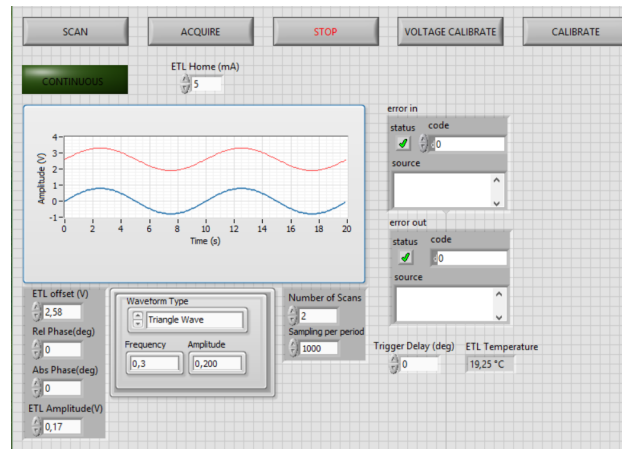


FIGURE 3.4: Software User Interface.

as well. "External start" trigger mode is chosen so that the system, after the TTL trigger pulse, will acquire accordingly to the acquisition parameter set in the acquisition mode dialog window.

3.4 Software

The aim of the software is to command the DAQ NI-6220 to produce two synchronized analog signals and a digital trigger to send to the ETL and Galvo driver and to the EMCCD respectively. In particular, in order to correctly image the illuminated plane, the synchronism between the motorized mirror and the adaptive lens is critical. The software, with the exception of some sub VI provided by the production holding, has been developed for this thesis project by candidate. In the picture is shown the user interface of the software, with the on fly adjustable parameters.

The software has been conceived as a nine states state machine summed in the figure 3.5, architecture suggested by [27].

The state machine architecture, as shown in [27], is an easy way of implementing case structure in both logic and visual programming, therefore at low or high level coding. Fig. 3.5 depicts the main point in the state machine software design. After the initialization protocol, which sets the hardware components ready to operate,

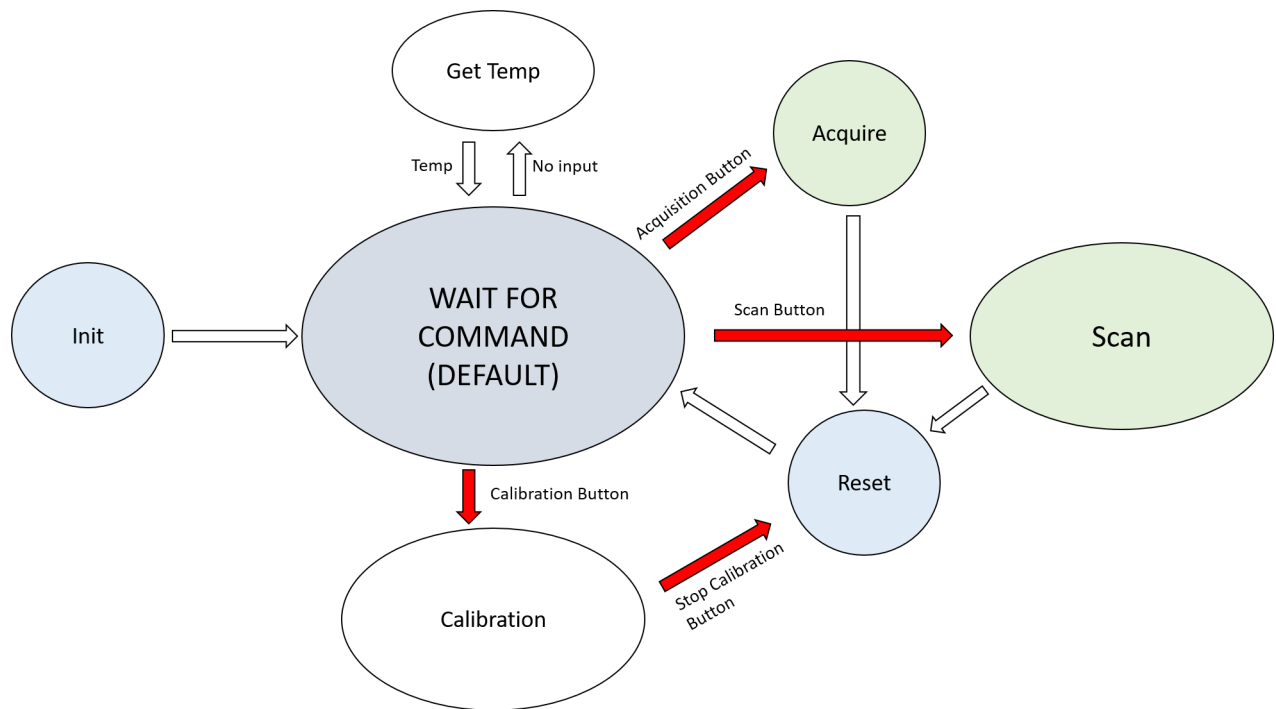


FIGURE 3.5: Machine state diagram. In red are highlighted the state transitions where an input from the user is required; in blue are marked the transition state fundamental for the right working of the whole software while in green are shown the imaging states. Finally in gray it can be found the default state "wait for command".

the machine goes to the "wait for command" state, also defined as default state, which continuously updates and ends to the "Get Temp" state if no input from the user is detected; to simply know the temperature of the lens a certain command string has to be sent to the lens driver, as it will be discussed in details in the next sections. Once an input is given (red arrows transition in Fig. 3.5, from the default state the machine goes to the state determined by the input itself, such as the single acquisition state, the scanning state or the calibration state. These last three software states imply a reset of the hardware components, resetting that is done right before going back to the default state, so that the whole procedure can be performed over and over again, until a "Stop" signal is given by pressing the namesake button, as shown in Fig. 3.4. In the following sections, all of these states will be analyzed in details, showing the corresponding Labview code.

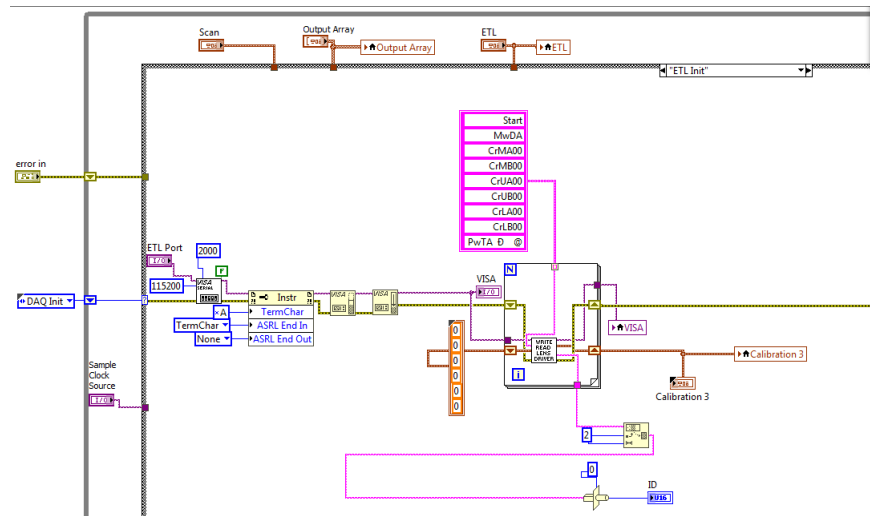


FIGURE 3.7: Electrotunable Lens initialization state.

Once the two tasks are rightly set, the two error signal eventually produced (the yellow wires in figure) are merged. Once having initialized the DAQ device, it is the time to consider the state that initializes the ETL driver as well. In the "ETL init" state, as displayed in Fig 3.7, the VISA communication parameters are set, such as baud rate and data bits, and calibrations command are sent to the lens driver, which is turned on and put at 0 dpt (having optical property as if it was no lens at all) thanks to the "write and read lens" sub VI. Once this task is performed, the PC can effectively communicate with the lens driver. For what it concerns this state, the communication consists in setting to the ETL driver the safe operation range, therefore upper and lower current bounds and the mode to operate in. This information exchange between the two parties (PC and ETL driver) happens to be hold in a proper protocol, determined by the driver characteristics. The "Write and read driver" sub VI takes as input an array of characters strings, each of them containing a well defined command. Let us now get in details with every string in the array shown in Fig. 3.7.

- MwDa: The first character "M" stands for "mode command" that together with the second character "w" writes a new frequency operation mode to the driver. The operation mode to be written, together with the channel to write the mode into are therefore specified by the third and the fourth character of the command string; for this particular case, the "D" frequency

mode is written into channel A of the driver. For this particular model of electro-tunable lens the channel specification is somehow useless, since only channel A is available. With "MwDA", for what has been said up to now, the driver receives the command to set a new operating mode into channel A, the D frequency mode. The driver is configured to operate in five frequency modes, each one represented by capital letter: "S", "Q", "T", "C" or "D". Respectively, they stand for sinusoidal, square, DC, triangular and controlled signal (it allows the driver to maintain the focal power of the connected lens). So finally, the string "MwDA", once received by the driver, set the channel A to be operating in DC mode. Furthermore, it has to be pointed out that the "write and read lens driver" also handles the feedback given by the driver itself, signaling if an error in communication occur.

- CrMA00 and CrMB00: Calibration commands tare started with a "C" character, this kind of commands are used to set and read calibration values and current limits. These values are stored in the EEPROM, a non-volatile memory, and are potentially kept there for years. Software current limits are set to protect the electro-tunable lens from overcurrent or to fix the maximum achievable focal power. Limits also apply in analog input mode, a mode that will be taken into consideration later. The second characters of the two strings analogously to the "w" character in the "MwDA" string, means a reading command. The next byte determines what value to set or read and in this case it is "M" for the maximum current calibration value (in [mA*100]). The next character simply selects the channel ("A"), and it is sent followed by two data bytes (16-bit integer). The upper limit default value is 29284 (292.84mA). The software current limits saved in the EEPROM are 12bit current value and can also be negative.
- CrUA00 and CrUB00: this calibration command sets the upper current limit (represented by the byte "U") for the channel A and B.
- CrLA00 and CrLB00: this calibration command sets the lower current limit (represented by the byte "L") for the channel A and B.

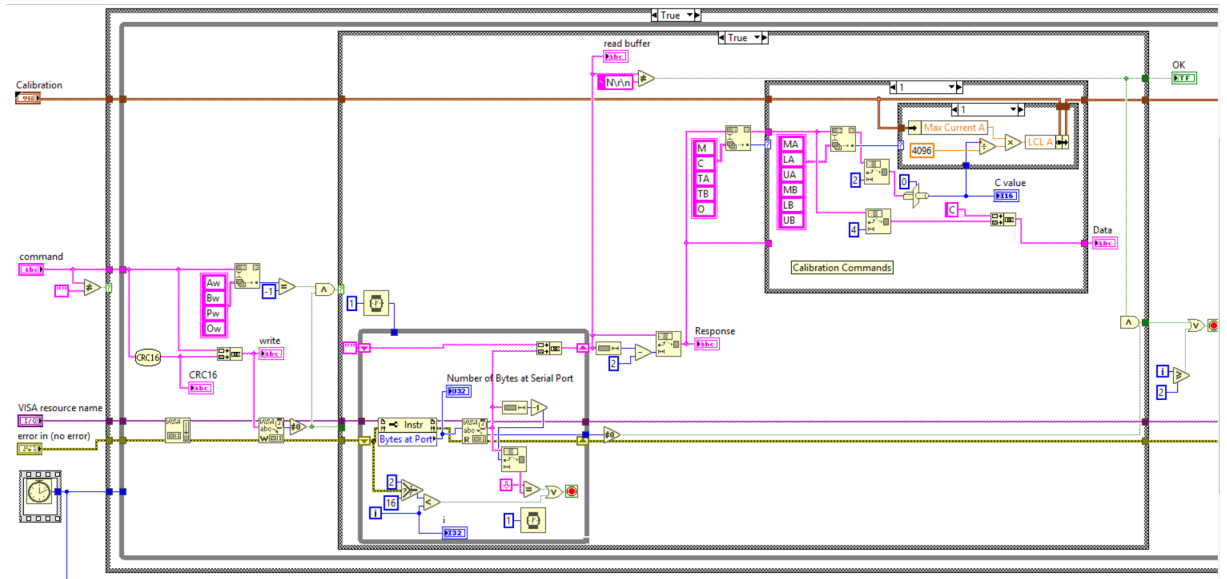


FIGURE 3.8: Write and read function. This sub VI allows communication with the lens driver.

- PwTA: this command has been inserted to set the right temperature limits to the driver, selectable by using "P" as first character of the string. Again, the second byte "w" stands for writing a temperature signal "T" to channel A, the command then includes 2 bytes for the desired temperature limits values (45 and 20 Celsius degrees here translated in the ASCII values 209, D and 64, @) and 2 dummy bytes.

Let us now take a look at the sub VI in Fig. 3.8. In the leften part of the program, a check for the correctness of the data communication is performed thanks to a cyclic redundancy check algorithm, that will be analyzed in the following section. Following the data flow, if the CRC confirms that the command strings have been successfully received by the driver, they can be written to the visa port. A Boolean check is made as a logic and between the state of the command writing and the validity of the input command string: if data have been transmitted properly and have effective validity, then in the following case structure the true case is accessed. Here a wait block of 1ms is inserted in the data flow to let the written commands be processed by the lens driver and to avoid reading before applying new values. In the lower left corner of the case structure it is placed a loop cycle with the goal of bitwise checking the returned data from the visa port for a total amount of

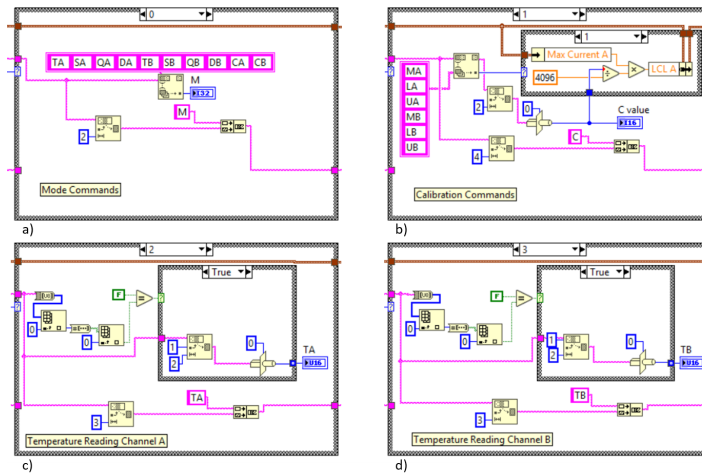


FIGURE 3.9: Different cases depending on the input command. a) Case corresponding to a mode setting command. b) Case corresponding to a calibration setting command. c) and d) Cases corresponding to the channel A and channel B reading command respectively.

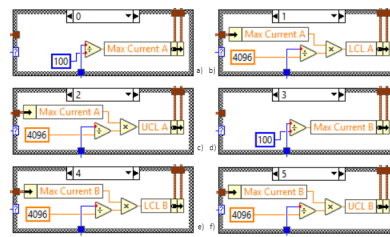


FIGURE 3.10: Six Different cases depending on the input command. It is shown how each type of command is two way degenerate due to the two channels firmware

16 bytes. Finally, after this all correctness checking procedure, on the top right corner a case structure is placed with a specific case to handle any of the available commands: Mode commands ("M"), Calibration commands ("C"), Channel A or B temperature ("TA", "TB" reading) and an error input "O", whose corresponding case is not displayed, as it does nothing to the input data of the case structure.

In Fig. 3.9 the different cases depending on the input command string are shown. While for the mode command the command itself is printed on the user interface (3.9, a)), for a calibration check a nested case structure is implemented to be capable to manage all of the eventual quantities that can be calibrated: maximum current, maximum and minimum temperature for the two channels A and B, for a total of six cases plus one case for invalid input (where again no operation is performed).

After having initialized the hardware parts, the program goes to the default state "wait for command" and if no input is given by the user, stays there indefinitely. From this state the user can choose among several states depending on what his goal is.

3.4.1.1 CRC algorithm

A cyclic redundancy check (CRC) is an error-detecting code commonly used in digital networks and storage devices to detect accidental changes to raw data. Blocks of data entering these systems get a short check value attached, based on the remainder of a polynomial division of their contents. On retrieval, the calculation is repeated and, in the event the check values do not match, corrective action can be taken against data corruption. CRCs are so called because the check (data verification) value is a redundancy (it simply expands the message with no information addition) and the algorithm is based on cyclic codes. CRCs are popular because they are simple to implement in binary hardware, and particularly good at detecting common errors. To compute an n-bit binary CRC, line the bits representing the input in a row, and position the (n + 1)-bit pattern representing the CRC's divisor (called a "polynomial") underneath the left-hand end of the row. In the following a CRC checksum implementation can be found for Labview, but it can be easily performed in other high level programming languages such as C++ or Matlab.

In this example, it is encoded a 14 bits of message with a 3-bit CRC, with a third degree polynomial $x^3 + x + 1$ that has four coefficients ($1x^3 + 0x^2 + 1x + 1$). The polynomial is written in binary, meaning that its coefficient can take only 0 or 1 as value; in particular the coefficients are 1, 0, 1 and 1. The result of the calculation is therefore 3 bits long.

Start with the message to be encoded:

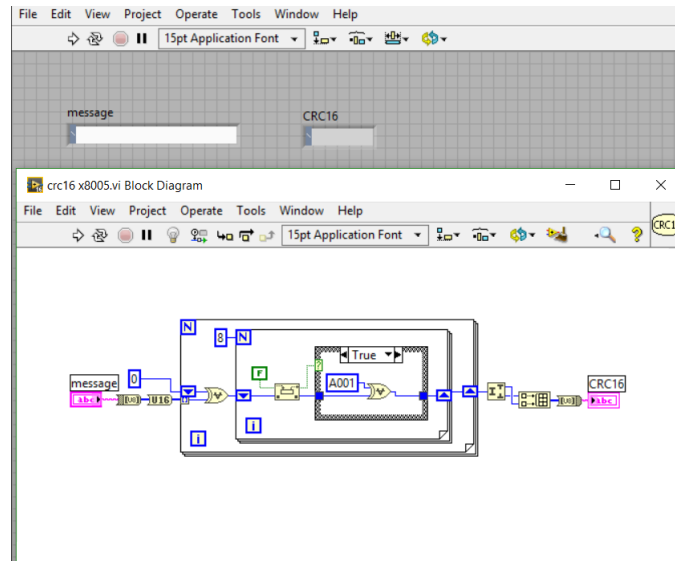


FIGURE 3.11: CRC checksum in Labview, with overlapped block diagram and user interface.

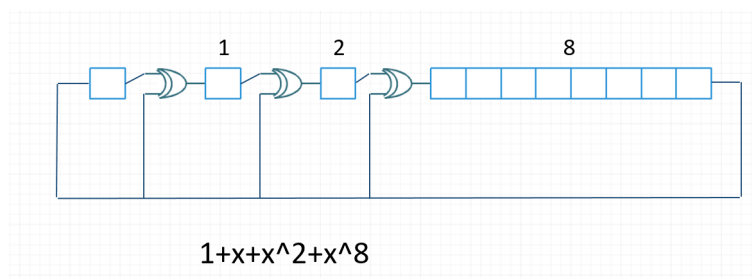


FIGURE 3.12: CRC checksum XOR circuit implementation for a polynomial divisor of $1 + x + x^2 + x^8$

11010011101100

This is first padded with zeros corresponding to the bit length n of the CRC. Here is the first calculation for computing a 3-bit CRC:

11010011101100 000 — input right padded by 3 bits

1011 — divisor (4 bits) = $x^3 + x + 1$

01100011101100 000 — result

The algorithm acts on the bits directly above the divisor in each step. The result for that iteration is the bitwise XOR (as shown in Fig.3.12) of the polynomial

divisor with the bits above it. The bits not above the divisor are simply copied directly below for that step. The divisor is then shifted one bit to the right, and the process is repeated until the divisor reaches the right-hand end of the input row. Here is the entire calculation:

```

11010011101100 000 — input right padded by 3 bits
1011 — divisor
01100011101100 000 — result (note the first four bits are the XOR with the divisor
beneath, the rest of the bits are unchanged)
1011 — divisor
00111011101100 000
1011
00010111101100 000
1011
00000001101100 000 — note that the divisor moves over to align with the next 1
in the dividend (since quotient for that step was zero)
1011 (in other words, it does not necessarily move one bit per iteration)
00000000110100 000
1011
00000000011000 000
1011 00000000001110 000
1011
00000000000101 000
101 1 —————
00000000000000 100 — remainder (3 bits).

```

Division algorithm stops here as dividend is equal to zero.

Since the leftmost divisor bit put to zero every input bit it touched, at the end of the process the only bits in the input row that can be nonzero are the n bits at the right-hand end of the row. These n bits are the remainder of the division step, and will also be the value of the CRC function.

The validity of a received message can easily be verified by performing the above calculation again, this time with the check value added instead of zeroes. The remainder should equal zero if there are no detectable errors.

11010011101100 100 — input with check value

1011 — divisor

01100011101100 100 — result

1011 — divisor

00111011101100 100

00000000001110 100

1011

00000000000101 100

101 1

————— 0 — remainder

3.4.2 Initialization and Calibration

Once in the "waiting for command" state, by simply selecting it front the front panel, the user has the possibility to:

- Independently setting the current in the electrotunable lens;
- Synchronously scanning the volume with both the light sheet and the ETL, with a TTL signal produced in order to trigger the EMCCD as soon as the first analog sample is written into the lens and the galvanometric mirror driver;
- Acquiring an image without scanning;
- Calibrating the system.

Calibration can be performed in two different ways: setting the voltage oscillation amplitude for the ETL while having the galvo in one of the three available positions, 0 or \pm Galvo Amplitude or setting the analog current.

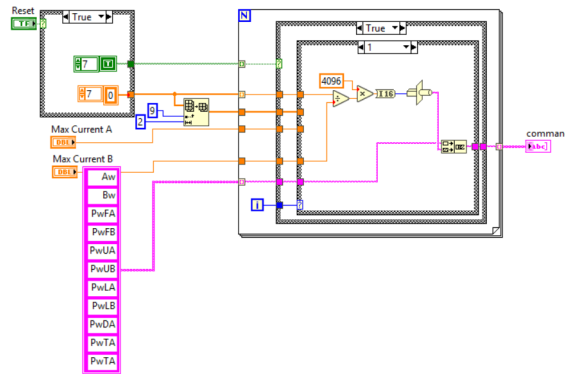


FIGURE 3.13: Set Current. This sub VI allows setting of a certain current value to the lens driver.

Since the analog mode of the lens driver only accepts analog current or voltage values and no optical power, it is easier (and much more reproducible!) for the user to set the voltage amplitude instead of the current, which tremendously suffer from temperature fluctuations.

3.4.2.1 ETL Analog

This state of the program has the goal of correctly configure the Lens Driver to convert an analog Voltage input into a valid current output to send to the electro-tunable lens. This is done thanks to the functions "Set current" and "Write and read lens". Whereas the "Write and read lens" sub Vi has already been analyzed, nothing has been said about the "Set current", displayed in Fig. 3.13. On the top left corner, a panel is placed to handle the user interface, outputting two arrays, one made by Boolean values (indicating whether or not a certain variable is displayed and therefore can be modified by the user) and one made by numerical entries given directly by the user; anyway, the user interface will not play any role in the context of the software as a whole. The center for loop takes as input the two arrayed mentioned before, two max current values and a string of commands, which are handled by the case structure displayed in Fig. 3.14. Here, except for the first two command strings, any other is of the kind "PwXA" or "PwXB". This kind of command string is a string for the setting of

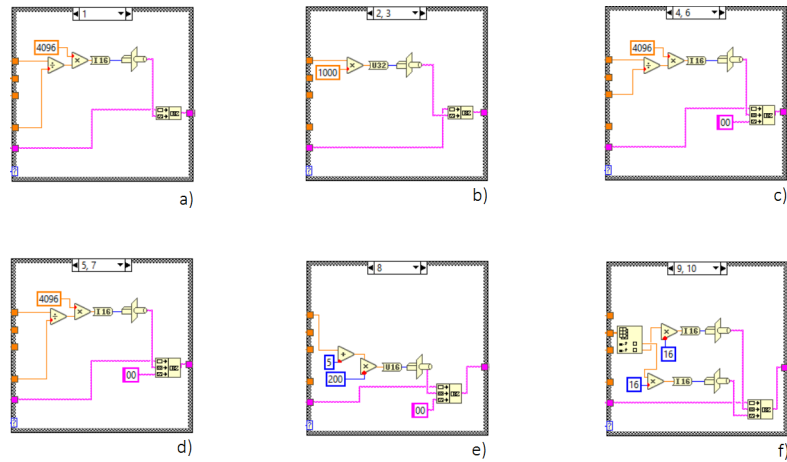


FIGURE 3.14: In this figure all the possible cases of different inputs are shown as different case structure panel. Again, some of them are two degenerate due to the two channels firmware.

the focal power ("Pw"). The expected variation in time of this optical power is then determined by the third character of the command string, as already said in the previous section, choosing among the symbols: "S", "Q", "T", "C" or "D". To sum up, for a setting focal power command, the PC has to send to the driver a string of the kind "PwDaxxYYLH", where xx is a signed 16bit integer, high byte sent first and YY are 16 dummy bits, as shown in Fig. 3.14 for c), d), e).

Now that every piece playing a role in "ETL analog" has been explained, let us go through the overall state. As it is displayed in Fig 3.15, the command MwAA is sent to the driver together with the output string of the "Set current" and with the temperature reading string "TA". Simply, "Set current" outputs the calibration values stored in the EEPROM mentioned in the section 3.4.1. The "MwAA" command string is such that once received by the driver, it sets the latter into the so called "Analog Mode", from which the name of the state "ETL Analog". Instead of the analog command mode, how can also select among several operation mode as for example the sinusoidal mode (identified by "MwSA"), triangular mode ("MwTA") and so on. The three command strings coming from "set Current Sub VI", "MwAA" and "TA" are then sent to the "Write and read" Sub VI that, in order, fetches the values stored in the EEPROM, set the driver to "Analog mode" and puts the lens to the values pointed out in the brown cluster on the left, finally reads the temperature of the lens and outputs it. After the procedure is completed

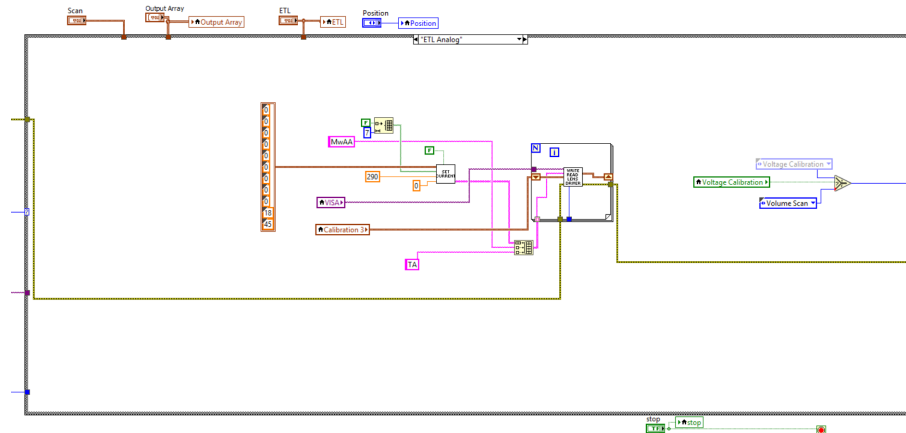


FIGURE 3.15: Block diagram of the state "ETL analog".

and the Lens driver is ready to receive an analog signal, depending on the user input, the "ETL Analog" can end up in two states: "Voltage Calibration" or "Volume Scan".

3.4.2.2 Voltage Calibration

This part of the software is fundamental for obtaining good images from the whole setup. The Voltage Calibration state aims to find the analog voltage value sent to the ETL that focuses the two scan extremes. As shown in Fig 3.16, while in this state the user can switch among three positions of the galvo mirror as said before and can on fly modify the voltage displacement from the ETL offset. The symmetry of the optical power is such that the "0" position has to be in focus for a voltage of ETL offset, while the other two have to be focused by the lens for a voltage signal equal to \pm Voltage Ch A. The state is base on a while loop at the center of Fig.3.16, that continuously performs the functions contained until an external input is given. Since here no acquisition is involved, the only task that is called is the analog, which aims to send the two voltage signals to both the galvanometric mirror and the electro-tunable lens, sending this signals from the ports *Dev1|ao0* and *Dev1|ao1*. Following the dataflow, before entering the while loop, the task is set to contain a continuous signal up to a time-out interval of 1000ms. Inside the loop, from the cluster composed by the values to control the mirror scans, the amplitude is taken and fed to a case structure that is controlled

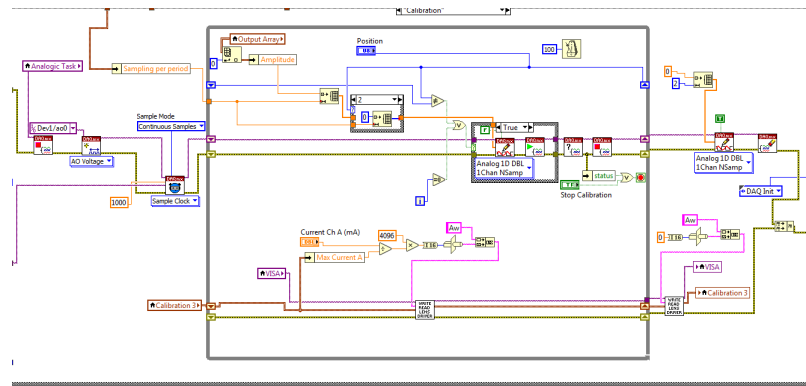


FIGURE 3.17: Block diagram of the state "Calibration".

3.4.2.3 Current Calibration

Together with the possibility to calibrate the system with an analog voltage signal, it was implemented also a "Current Calibration" state. The working principle is the same of the already seen "Voltage Calibration" but instead of a constant voltage, a constant current is sent to the ETL driver. As it is displayed in Fig. 3.17, the PC sends to the ETL driver the command string assigned to the current set commands. This commands are of the kind AwxxLH, where xx is a signed 16bit integer with a value between -4096 and 4096, and it is determined through the following formula $x_i = \frac{i_0}{i_c} * 4096$, with $i_c = 293mA$. In this case, the analog task is only set to contain samples to be sent to the galvanometric mirror, since the current signal generation is not up to the DAQ, but it is provided by the ETL driver itself. Once the user presses the Calibration button a second time, the data flow exits the while loop. Again, the analog task is filled with null samples such to put the galvanometric mirror to its centered position and a 0mA current command is sent to the driver.

This state allows the user to have a direct control on the optical power of the lens but it is strongly affected by temperature oscillation, so that it only has to be used in controlled situation when the ETL temperature is monitored.

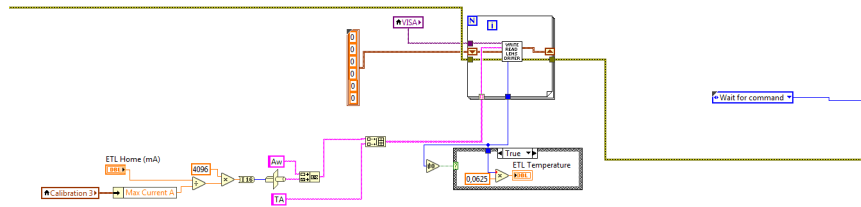


FIGURE 3.18: Block diagram of the state "ETL get Temperature and Restart".

3.4.2.4 ETL get Temperature and Restart

Due to the critical role that ETL temperature plays for its performances, a state is implemented to reset the lens focal power to a "ETL Home" value and to simultaneously measure the temperature. The lens temperature is measured thanks to an integrated sensor onto the driver board, model NXP SE97B. This sensor outputs a value that can be converted to a temperature with the formula $Temperature[^{\circ}C] = data * 0.0625[^{\circ}C]$. The temperature read command has as first character a "T" followed by the channel selection byte. The command is then completed with the 16bit CRC calculated over the two command bytes.

The variable "ETL Home (mA)" is read from the user panel, rescaled after the maximum current value which is read from the cluster names "Calibration 3" and that contains all of the value stored in the EEPROM, converted to a string value (displayed in pink in Fig. 3.18) and attached to the set current command string "Aw". Then another command string for temperature reading is concatenated to the "Awxx" command string, and sent to the "write and read lens driver" sub VI, that when fed with a "TA" string, outputs the data read from the NXP SE97B sensor. After an easy conversion, the temperature value is then shown to the user interface under the name of "ETL Temperature", Fig. 3.4.

The case "Wait for Command", if no inputs are given, ends in the "ETL get Temperature and Restart" state, that in turn ends in the default case, updating the displayed ETL temperature with a refresh time equal to the time taken by the PC to go through the first case and back to the temperature reading stage.

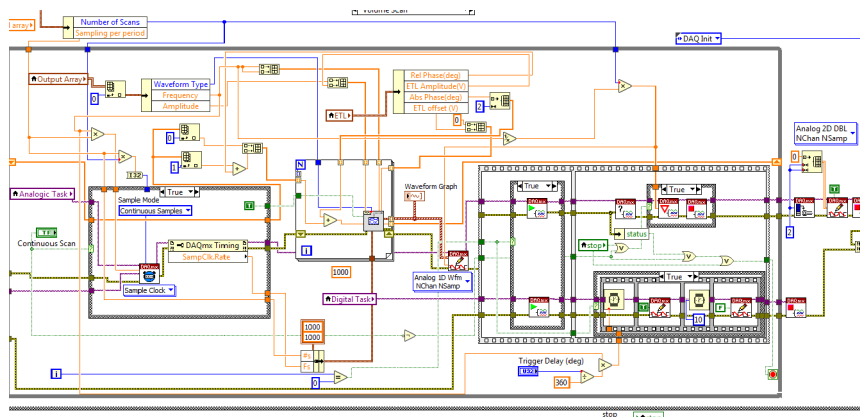


FIGURE 3.19: Block diagram of the state "Volume Scan".

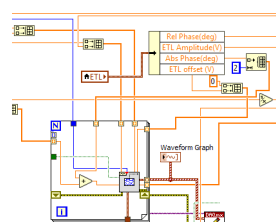


FIGURE 3.20: Block diagram particular of the state "Volume Scan" regarding the samples generation for the analog DAQ task.

3.4.3 Scan and Imaging

3.4.3.1 Volume scan

The state described in this section represents the heart of the program itself. It is indeed the state where the simultaneous scanning of both the ETL and the light sheet is performed, together with a synchronized TTL trigger signal for the EMCCD sensor. Every action described in the following is contained in a while loop, allowing "on fly" modification of the scanning parameters.

As input, this case needs first of all the analog and the digital task in order to control the lens driver, the galvo mirror and the sensor respectively; on top of that it also needs other parameters that have to be given by the user after the calibration (ETL offset and amplitude) and according his or her measure settings (number of scans, absolute and relative phase of the two analog signals). The parameters that respectively determine the ETL oscillations and the galvanometric mirror scans are retrieved from two clusters on the upper side of the box, as displayed

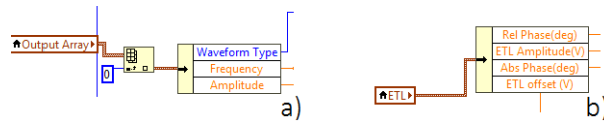


FIGURE 3.21: Block diagram particular of the state "Volume Scan" regarding the parameters retrieval for the generation of both signals.

in Fig. 3.21. This way of recalling a value from a saved cluster make it easier for the developer to retrieve certain values. After having set the clock parameters properly once finite or continuous scan is chosen, the analog task is written with two wave forms that can differ in amplitude, phase and offset but maintain the same shape and frequency. As the reader may imagine, the shape of the signal can be chosen among the following: triangular, sinusoidal, saw tooth or square. The for loop assigned to the samples generation is shown in Fig. 3.16 and it only consist of two iterations per while cycle: the first mirror signal, the second for the ETL's. As well as the scanning parameters were retrieved from two clusters, so the sampling parameters such as number of samples and sampling frequency are directly obtained from the task wire thanks to the "DAQmx Timing property node", with the latter being a formal way of inquiring the task of a certain preset property. Once it has been generated, the waveforms are displayed to the user through a waveform graph, to check if everything as been generated as liked. At this point everything is in shape to start the two tasks. The two tasks are started together thanks to the so called "flat sequence" provided by Labview. The digital trigger sent to the camera is also shown in 3.19; it is performed in the most straightforward way possible: a true level constant voltage followed by a false level constant voltage after a time decided by the user (10ms in Fig. 3.19). At the same time, a check stage is implemented such that an eventual stop order given is seen and performed, terminating the signal generation after the data buffer is emptied. In Fig. 3.22 it is displayed how an eventual delay between the scanning and the acquisition is handled by the software. Once the scanning is over and so is the while loop, the digital task is cleared whereas the analog task is set such that both the Galvo mirror and the electrotunable lens are driven back to their 0 positions and are for their part cleared.



FIGURE 3.22: Block diagram particular of the state "Volume Scan" regarding the delay mechanism between the generation of the analog signals and the digital trigger to be sent to the EMCCD.

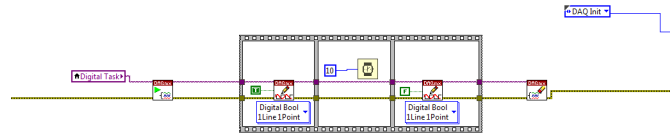


FIGURE 3.23: Block diagram of the state "Static Acquisition".

3.4.3.2 Static Acquisition

This state has been implemented with the goal of allowing the user to send a single trigger signal to the imaging sensor. Such a state can be helpful especially when the system is being optically characterized with the means of tools such as fluorescent beads: these objects in fact may need a static situation due to the fact that they are usually employed in an aqueous solution. The trigger is performed as already described in section 3.4.3.1 as it is shown in Fig. 3.23.

3.5 State Machine full Analysis

3.5.1 Classification

In this section it will be exploited a full analysis of the state machine presented in the previous sections.

This state machine belongs to the family of Moore's machines, since its outputs do not depend on the current inputs but only on the current state of the machine. For this work, the machine has to be intended as the ensemble of the PC and the DAQ so that we can consider as inputs the virtual buttons of the Labview Software as displayed in Fig. 3.4, and as outputs the three different signals that

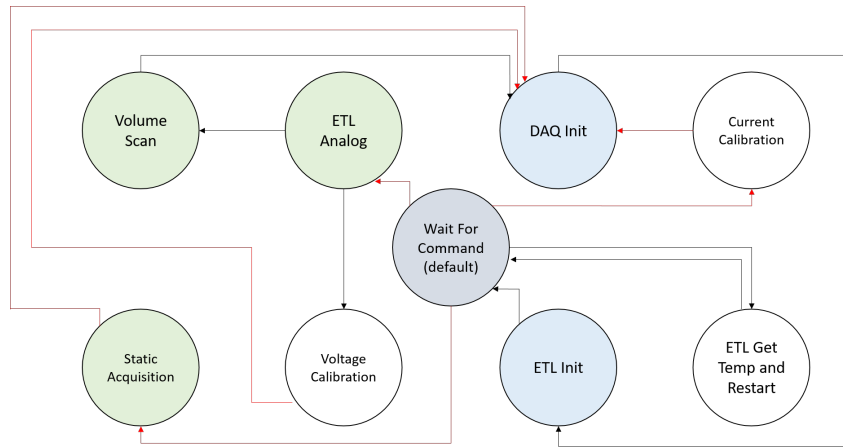


FIGURE 3.24: Complete State Transition Diagram.

State	Binary Encoding			
	S ₁	S ₂	S ₃	S ₄
Wait for Command	0	0	0	1
ETL Analog	0	0	1	0
Volume Scan	0	0	1	1
Static Acquisition	0	1	0	0
Current Calibration	0	1	0	1
Voltage Calibration	0	1	1	0
ETL get Temp and Restart	0	1	1	1
DAQ Init	1	0	0	0
ETL Init	1	0	0	1

FIGURE 3.25: Binary state encoding

the DAQ will be programmed to produce, together with a Temperature output to be displayed to be at user disposal.

In Fig. 3.24 it is displayed the state transition diagram with every possible state displayed. In this Figure, the red arrows point out the need for a particular input to be received for that transition to occur.

As clock to time all of the operations dictated by the software, it has been used the internal clock of the programmable DAQ, with a frequency of 80MHz (uncertainty of 50 ppm).

3.5.2 Encoding

In the following subsection are shown in figure the encodings that encrypt the state machine depicted in this project, according to the procedure shown in [27]. Since the machine consist of nine total states, 4 bits are needed for a complete binary encoding; those nine states are also the reason why one-hot technique was

Current State				Output Table			
S ₃	S ₂	S ₁	S ₀	Analog Output 1	Analog Output 2	Digital Output	T displayed
0	0	0	1	0	0	0	0
0	0	1	0	0	0	0	0
0	0	1	1	1	1	1	0
0	1	0	0	0	0	1	0
0	1	0	1	1	1	0	0
0	1	1	0	1	1	0	0
0	1	1	1	1	1	0	1
1	0	0	0	0	0	0	0
1	0	0	1	0	0	0	0

FIGURE 3.26: Output Table with state encoding

States Transitions Diagram											
Current State				Inputs				Next State			
S ₃	S ₂	S ₁	S ₀	SCAN	ACQUIRE	VOL. CALIBRATE	CALIBRATE	STOP	S ₃	S ₂	S ₁
0	0	0	1	0	0	0	1	0	0	1	0
0	0	0	1	0	0	1	0	0	0	0	1
0	0	0	1	0	1	0	0	0	0	0	1
0	0	0	1	1	0	0	0	0	0	0	1
0	0	0	1	0	0	0	0	0	0	1	1
0	0	1	0	X	X	0	X	0	0	0	1
0	0	1	0	X	X	1	X	0	0	1	1
0	0	1	1	X	X	X	X	1	1	0	0
0	1	0	0	X	X	X	X	0	1	0	0
0	1	0	1	X	X	X	X	1	1	0	0
0	1	1	0	X	X	X	X	1	1	0	0
0	1	1	1	X	X	X	X	X	0	0	0
1	0	0	0	X	X	X	X	X	1	0	0
1	0	0	1	X	X	X	X	X	0	0	0

FIGURE 3.27: Moore state transition with state encoding.

not exploited in this work, due to its greater complexity with respect to binary encoding.

The three output signals mentioned in the previous section are: one analog signal to command the lens driver, that lays in the range of 0-5V due to the driver specifications, a second analog signal laying between -10 and +10V (with a scaling factor 0.8 V /°) for an angular maximum span interval of ±12.5° and one digital TTL trigger to be sent to the EMCCD to trigger acquisition synchronously with the scanning of the galvanometric mirror. In Fig. 3.26 it is highlighted the output encoding for each state, already represented in binary according to Fig. 3.25.

Together with figure 3.24, these last tables gives a fully binary representation of the software, i.e. of the state machine. Starting from the table in 3.27, it is in fact possible to design an analogous, fully working alternative state machine set up, by implying only Boolean piece of logic as shown in [27]. To conclude with, this last paragraph gives an overall view of what the designed software is, thanks to a unique mapping of the relation between inputs and outputs.

Chapter 4

Calibration and Measurements

In this final chapter, after a short introduction about sampling requirements in a light detection system, will be presented images representative of each stage in the system development. In fact, the system was assembled in a way such that at each intermediate step tests were made on its optical performance; these steps were:

- assembling of the only detection path, to test for ETL influences on the overall magnification of the system and to test for software capability of giving the wanted output signal;
- analysis of the system overall magnification, fulfilling of Nyquist sampling theorem and lateral and axial resolution of the system, performed also with fluorescent samples;
- final setup test (as the one shown in Ch 2), with dynamical employ of both the motorized mirror and the lens, with optical targets and living, fluorescent samples.

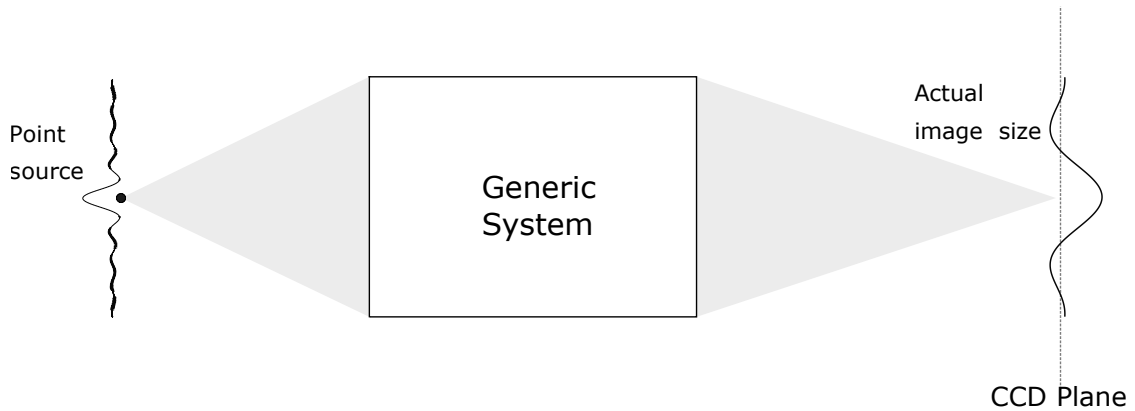


FIGURE 4.1: Image acquisition onto a CCD sensor

4.1 Sampling Theory

When speaking of data acquisition the most important thing to know is how to perform sampling properly. So in telecommunication as in optics, when a signal is sampled (no matter if a bit string or an image on a CCD), some constraints have to be respected in order to be able, once collected all the information, to reconstruct the input signal correctly. This constraint takes name after Harry Nyquist and it states that a continuous input signal can be entirely reconstructed by a set of equally spaced samples, if the sampling happens to be at more than twice f_{max} , with the latter being the highest frequency component of the signal to be sampled.

Let us now consider the simplest case for image acquisition as depicted in Fig. 4.1. As previously highlighted, the system resolution is affected by the numerical aperture of the light collection optics; however this is not the only factor to be taken into account. In fact, the detection plane is not composed by a single detector but it is made by a 2D array of pixels with a finite dimension; intuitively, error for image reconstruction may show up for pixels that are too large or for a sample too close to the sensor. For a point source, the resolution limit given by Abbe's condition is

$$\Delta\rho = 0.5 \frac{\lambda}{NA} \quad (4.1)$$

but taking into account what it is stated by Nyquist theorem, the condition for correct image reconstruction suggests that the minimum pixel size (e), should be

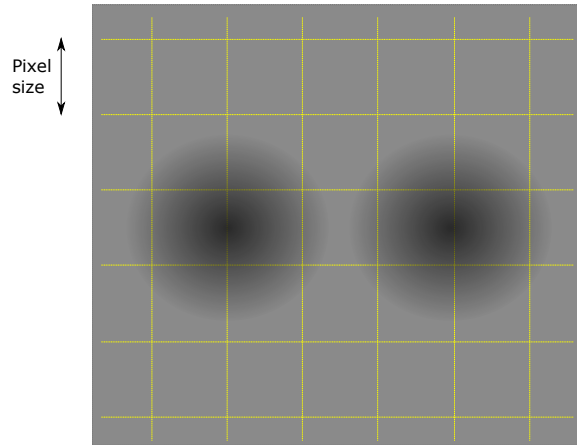


FIGURE 4.2: Image of two point sources onto a pixelated sensor.

at least half of this value, i.e.

$$e < 0.25 \frac{\lambda}{NA}. \quad (4.2)$$

Having an image spreading for more than two pixels in any direction is said oversampling, whereas having less than pixels illuminated by the seeing disc is said undersampling. While oversampling is usually acceptable to grant for the right acquisition also in the pixel diagonal, an exaggerated pixel density results in a useless reduction of the field of view. On the other hand, undersampling is no way to be desired, since it means that the data acquired by the sensor is missing the higher spatial frequencies of the real image transmitted by the imaging system [4.2](#).

In this project an EMCCD with a total of 1004x1002 pixels has been used, with each pixel size of 8 μm ; this, together with a system magnification of 10, grants a corrected sampling of a light emitting fluorophore at the sample plane [\[29\]](#).

4.2 System Calibration Tools

In order to investigate the system resolution, at different stages of the project images were taken. To do this, a resolution chart (1951 USAF test chart in [Fig. 4.3](#)) was used, together with a micrometer ([Fig. 4.4](#)). The first consists in a pattern of light absorbing bars, grouped by three (the so called Ronchi rulings)

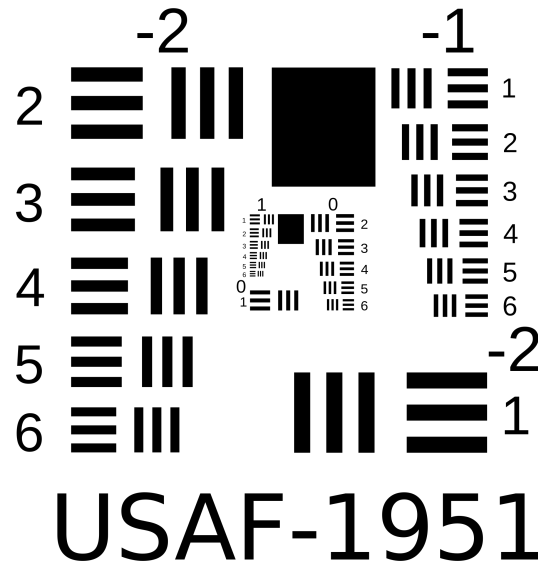


FIGURE 4.3: USAF-1951 resolution target. In this project it was used the positive target, for transmission imaging.

with a decreasing dimension from the outer to the inner regions. Bars go from a maximum dimensions of 2mm to a minimum of 0.55 μm . The whole target is made by six groups of bars and three layers. A simple way to determine the system resolution is the following:

$$Resolution(lp/mm) = 2^{\frac{Group+(element-1)}{6}}, \quad (4.3)$$

where lp stands for line pair, each group is made by six elements, from 1 to 6, and goes from one layer side to the other, where with layer is intended one of the three level of bars dimensions.

The micrometer instead is a glass printed pattern, with dimensions 25mm x 75mm, which shows a ruler pattern with each bar 1mm long and separated from the adjacent by a 10 μm distance (Fig. 4.4).

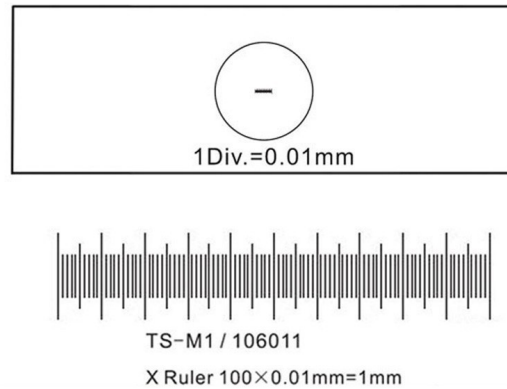


FIGURE 4.4: Micrometric ruler. This tool has been lately used to characterized the system.

4.3 System Calibration: Positioning and Stability test

In first place, data has been taken to investigate if and how the position of the electro-tunable lens along the optical detection axis affects imaging capability. In fact a bad positioning of this adaptable element results in a varying magnification at the CCD plane, therefore being such that a good scanning would be impossible to perform. At this stage only the bright field illumination was used, to make it easier to identify magnification variation for different optical power of the ETL. So different images were taken at different illumination apertures and at different focal lengths of the electro-tunable lens; the results are shown in Fig. 4.5, where different optical power images are placed side by side. From this straightforward analysis, it has been noticed how the ETL was in an acceptable position such that the overall magnification of the detection system remained practically unchanged for different focal power of the lens. In particular in Fig. 4.5 are shown the most representative cases of optical power for the ETL: 0 dpt for case a), -2 dpt for case b), 1.5 dpt for case c) and 3 dpt for case d); these values has been considered as the most explanatory due to the overall focal range of the lens, from -2 to +3 dpt. In this first configuration of the system, where only the bright field illumination

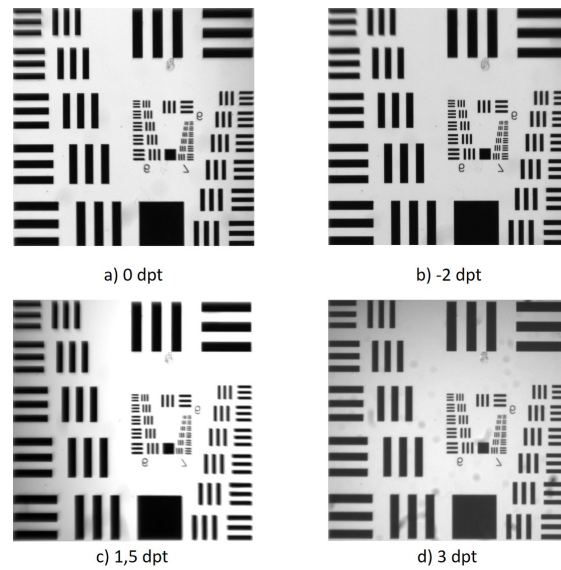


FIGURE 4.5: Magnification test for different optical power of the electro-tunable lens.

and the detection are used, the optical elements used are such that the magnification is yet constant, but with a value of 6,4 instead of 10 as it is for the complete system. At this development stage in fact it was only to be investigated the ETL properties in affecting the detection path characteristics, so that the actual value of the magnification is irrelevant, as long as it is constant.

Once verified that, if put in the weighted middle of the 4f system, the electro-tunable lens does not affect the magnification of the detection path for different focal lengths, stability tests were performed to inspect the capacity of the element in holding a well determined optical power in time. Thanks to the software described in the previous chapter, the lens was set at -2 dpt, then images were taken at intervals of 20 minutes each; in Fig. 4.6 a), b), c), are shown images taken by the system at 3 time instants each of them separated one hour from the previous; again, even if along with time the lens slowly changes its focal power (towards its rest position), this drift is easily acceptable since SPIM is characterized by an high speed image acquisition; moreover this changing in optical power has not been noticed in a situation where the lens is turned on and off multiple times over a long lasting time interval, which is a situation most likely to happen during a

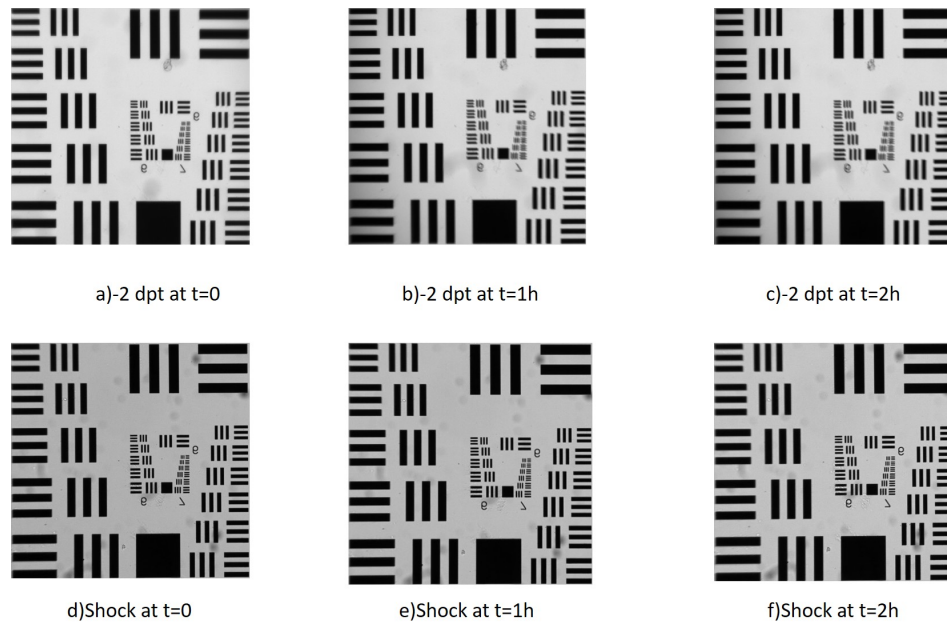


FIGURE 4.6: Stability test for the electro-tunable optical power in time. Pictures a) b) c) follows the time evolution of the system at time intervals of one hour; pictures d) e) f) shows how the ETL reacts to focal power changes (from 3 dpt to -2, the maximum excursus available), at time interval of one hour.

measurement session.

Finally, tests were performed to see how a rapid change in focal power, ideally a step shock, affects again the plane imaged onto the sensor. This is indeed important in a scanning technique since the focal power of the lens is continuously changing depending on the DAQ board analog signal. The situation is shown in Fig. 4.6 d), e), f). Here the lens is kept at a focal power of -2 dpt, set to 3 dpt and then driven back to the former value in the shortest time achievable according to the software and the DAQ characteristics. The shock test has been performed again several times while in Fig. 4.6 they are only shown the first, the middle and the last shock ($t=0$, $t=1$ hour, $t=2$ hours respectively). From this analysis it is remarkable the fact that the plane of the target is better in focus (no drift is present) with respect to the previous situation where no shock was induced at all; this is probably given by the feedback optical power sensor present in the ETL, which are activated once a change in the lens optical properties occurs.

At this stage, the system performed an overall magnification of 6.67; due to the

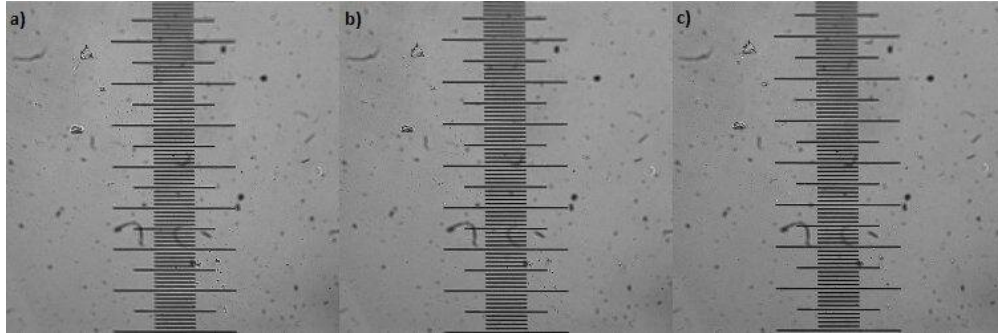


FIGURE 4.7: Micrometer focused at different distances on the optical axis. Each image correspond to a different optical power value of the ETL, in particular to a) 3dpt, b) 0dpt and c) -2dpt

fact that the first relay lens in the detection path had a focal length $f_{R1}=150\text{mm}$ (AC254-150-A-ML), so that the 4f system, together with the imaging objective and the tube lens, contributed with a magnification of the object plane of $M = 10 * \frac{100\text{mm}}{150\text{mm}} \simeq 6.67$.

4.4 System Calibration: Magnification and Scanning range

After placing the right lens as first relay lens (AC254-100-A-ML), further tests were done to check for the magnification and for the theoretical scanning range derived in chapter 2. In particular, the magnification has been quantified thanks to a micrometric ruler as the one displayed in Fig. 4.4 and its dimensions: in fact, given that each bar of the micrometer is spaced from the adjacents by $10 \mu\text{m}$ of transparent glass and that the dimension of each pixel is $8 \mu\text{m}$, a total magnification of a ten factor should give rise to an image where 80 bars of the micrometer are shown.

The images taken to quantify to total magnification are shown in Fig. 4.7. Here the two scanning range extremes together with the rest position of the ETL focal power have been exploited. As previously said, a 10X magnification is wanted so that 80 bars of the micrometer must be imaged by the camera and from the comparison of the target acquired in different positions we can see once again how

the magnification is constant and equal to $M=10,12$ ($80/79*10$) since only 79 bars are detected by the CCD.

Once calculated this value, with a similar approach it has been quantified the overall scanning range of the detection system. From Ch 2, we recall the formula

$$\Delta z = -n \frac{f_1^2}{f_{etl}} \frac{1}{M^2}; \quad (4.4)$$

this relation gives rise to a total theoretical scanning range of $648.5 \mu m$ for $M=10$, while for an effective magnification of 10,12 it decreases down to $633.21 \mu m$. Starting from its resting position, first it has been measured, with the means of the translation stage, the maximum excursion allowed with a negative and then with a positive focal length of the electro-tunable lens. Thanks to such a measurement, it has been retrieved, respectively, a range of $\delta z_{-2dpt} = 428.1 \mu m$ and $\delta z_{3dpt} = -220.5 \mu m$, giving a total scanning range of $\Delta z = 648.6 \mu m$, in good agreement with the theory.

4.5 In vivo Measurements

Imaging with the presented setup has been exploited thanks to fluorescent samples, marked with different fluorophores. The two molecules used to genetically mark the samples employed to characterize the developed setup are called GFP (Green Fluorescent Protein), whose emission happens to be at 509 nm [23] and CFP (Cyan Fluorescent Molecule), whose emission finds its peak at 490 nm [22]. Since the excitation laser emits radiation centered at 442 nm, filters have to be used to separate excitation light and fluorescence signal, depending on the sample analyzed. On top of that, the setup does not give the possibility to change excitation light, so that this is optimized only according to one of the two fluorophores used for imaging, in particular 442 nm is the wavelength at which corresponds a maximum in absorption for CFP, while for GFP excitation a non optimum excitation will inevitably lead to a situation where the fluorescence signal is not

maximized.

The two living specimen analyzed in this thesis work are *Zebrafish* (*Danio Rerio*) and *Arabidopsis Thaliana*, the former being marked with a Green Fluorescent Protein, while the latter with a CFP. Every Zebrafish sample was genetically engineered such to express GFP only in the endothelium (a type of epithelium forming the interface between circulating blood and the rest of the organism), while on the other hand the CFP in the *Arabidopsis Thaliana* samples was expressed in the cytosol, the liquid substance that can be found inside plant cells, and occupies about the 70% of its volume [30].

4.5.1 Optical Sectioning

In this section images of a GFP marked Zebrafish will be presented, a model organism for the investigation of vertebrate developmental analysis, to show the optical sectioning capability of the developed system. The samples presented in the following have been taken with different magnifications, at different stages of the optical setup development. In Fig. 4.8 it is presented stack of planes acquired of the upper part of a fish, from which it is taken Fig. 4.9. This stack of images has been taken at a point where the setup was not presenting a $M=10$ but $M=6.4$, nevertheless, good optical sectioning is presented, such that the blood vessels of the fish can be easily distinguished between one another.

In Fig. 4.10, a single plane image is shown, belonging to the lower part of a living zebrafish but at a final setup magnification (10X). Even if from different samples of the same species, the two samples have been imaged with a different acquisition parameters set.

The plane shown in Fig. 4.10 is as well as the one shown in Fig. 4.9 part of a stack of a hundred frames. From these two stacks of images, Maximum Intensity Projection are obtained (4.12 and 4.13 respectively). In a maximum intensity projection, from a stack of images it is retrieved a single one that is built from the pixels which show maximum signal intensity among all the slices acquired.

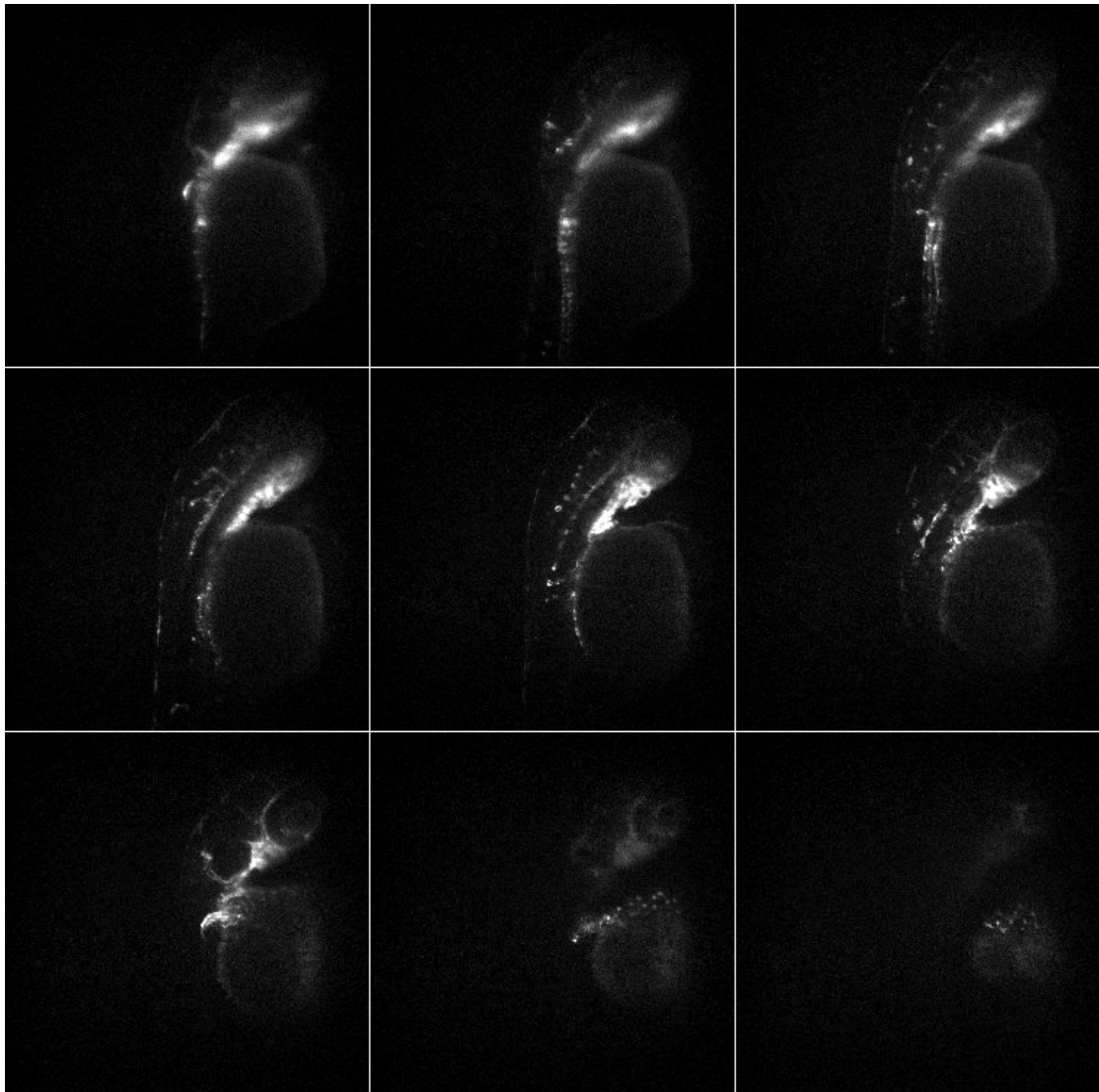


FIGURE 4.8: Image stack of the upper part of a zebrafish. The stack has been made by acquiring 100 planes at a magnification factor of 6.4. In this figure are presented 9 equally spaced planes.

The quality of this projections is affected by several factors, like the scanning speed, the CCD time acquisition for each plane, the good synchronism between illuminated and the focused plane and many other, as depicted in Ch 3. For each sample and often even for different part of the same, it have been set different acquisition parameters in order to optimize the image quality and possibly to limit the photodamaging of the sample.

The two scans, whose projections are shown in Fig. 4.12 and 4.13, have been respectively acquired with the acquisition parameters shown in tables 4.1 and 4.2, for a total acquisition time of 20 and 50s respectively. This long total acquisition

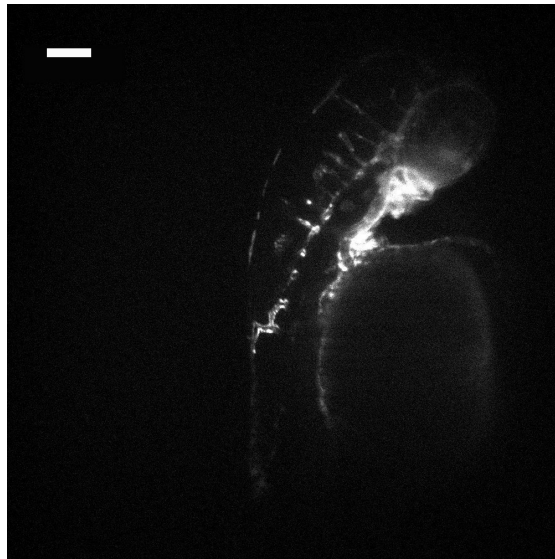


FIGURE 4.9: Single plane of the head of a zebrafish. In the top left corner a white bar scale representing $100 \mu m$ is shown.

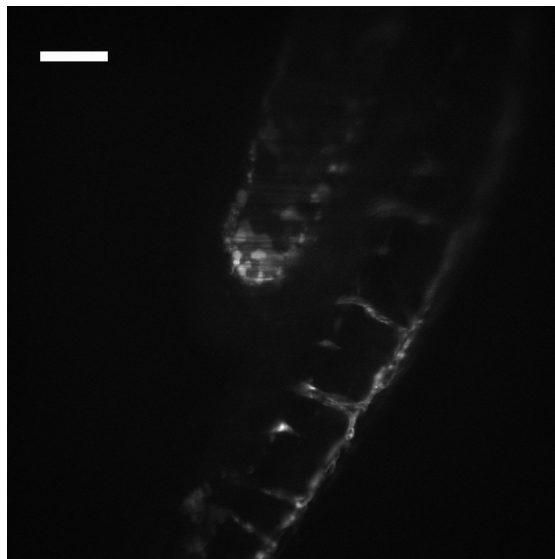


FIGURE 4.10: Single plane of the tail of a zebrafish. In the top left corner a white bar scale representing $100 \mu m$ is shown.

time it is due to both the slow characteristics of the camera used and the low intensity of the fluorescence signal.

The two images palettes faithfully represent the optical sectioning capability of the developed setup. In both of them, the first region of the sample to be excited by laser radiation and therefore to fluoresce is the region that is at a greater distance from the EMCCD. This means that before impinging onto the camera pixels, fluorescence signal has to travel through the remaining part of the sample (which is

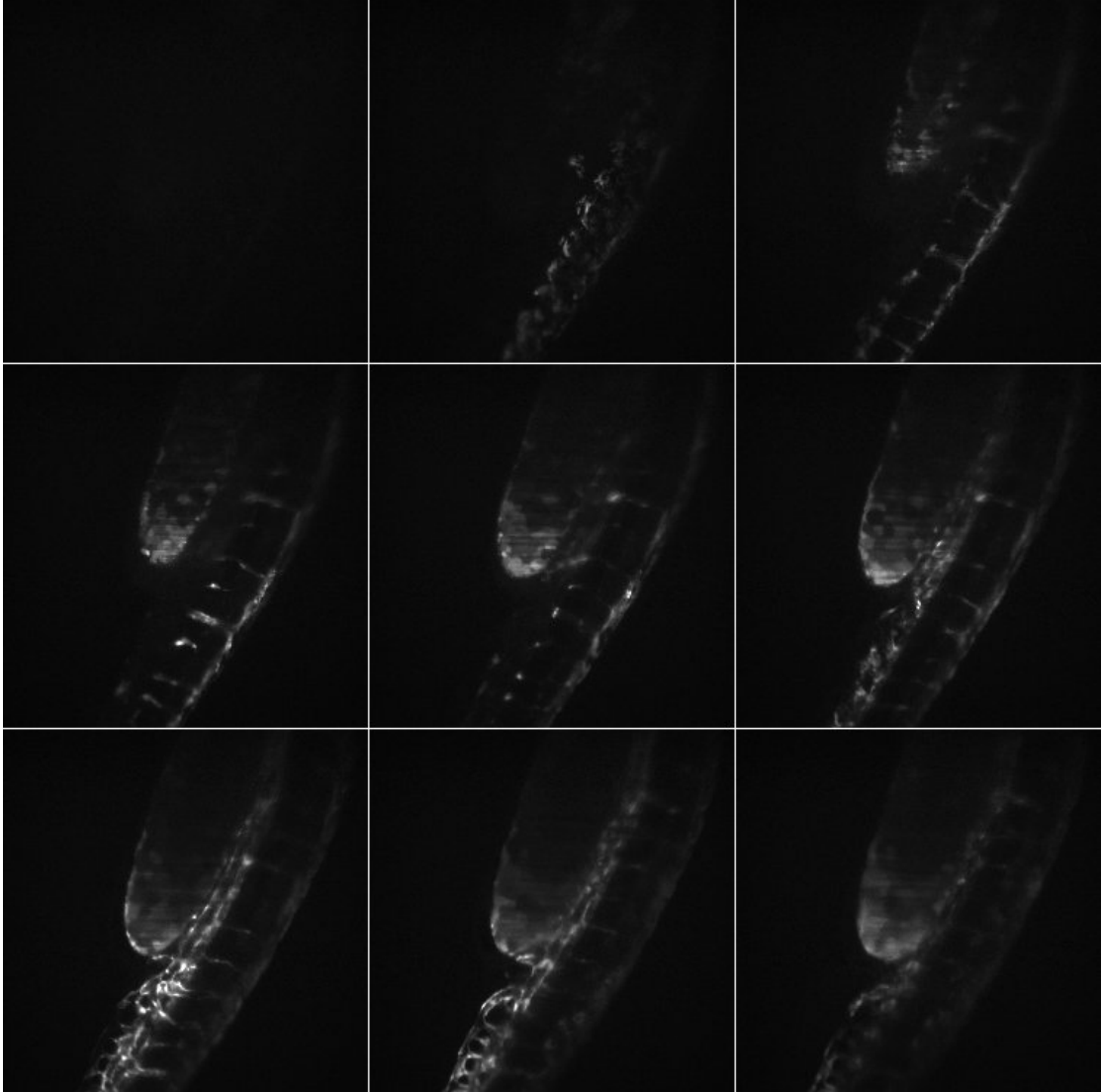


FIGURE 4.11: Image stack of the lower part of a zebrafish. The stack has been made by acquiring 100 planes at a magnification factor of 10. In this figure are presented 9 equally spaced planes.

ETL	Galvanometric Mirror	CCD	Scan
Amplitude=0.43 V	Amplitude=0.5V	$t_{exposition} = 0.2s$	f=0.025 Hz
Offset=2.61 V	waveform=sawtooth	$EMCCD_{gain}=100$	Absolute Phase=180°

TABLE 4.1: Different Parameters for the acquisition of the zebrafish head.

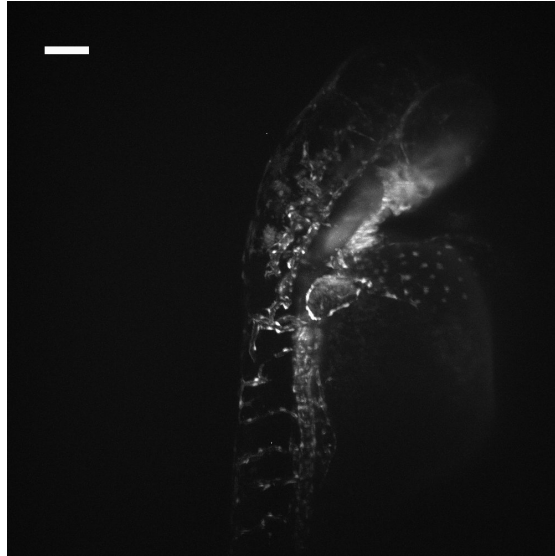


FIGURE 4.12: Maximum intensity projection of the head of a zebrafish. In the top left corner a white bar scale representing $100 \mu m$ is shown.

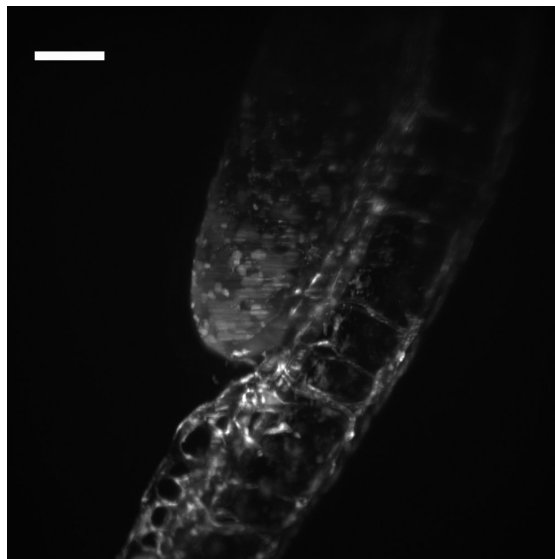


FIGURE 4.13: Maximum intensity projection of the tail of a zebrafish. In the top left corner a white bar scale representing $100 \mu m$ is shown.

not excited), being absorbed and scattered and therefore deteriorating the optical sectioning capability. As the scanning goes on, the voltage signal with which the motorized mirror is driven, increases, so that the mirror rotates. This rotation is such that, thanks to the f-theta system, the light sheet is moved towards the CCD sensor, giving a better sectioning as the light has to travel through a smaller part of the sample. It is impossible to obtain the same optical sectioning quality over the whole sample due to the absorption and scattering characteristics of the

ETL	Galvanometric Mirror	CCD	Scan
Amplitude=0.25 V	Amplitude=0.15 V	$t_{exposition} = 0.5s$	f=0.05 Hz
Offset=2.59V	waveform=sawtooth	$EMCCD_{gain}=20$	Absolute Phase=180°

TABLE 4.2: Different Parameters for the acquisition of the zebrafish tail.

sample itself. However, since the presented setup has been developed such that only three of the four sides of the sample chamber are occupied by illumination or detection objective, a further improvement could be that of introducing a symmetric illumination path, so that the specimen part which is the outermost from the excitation light source is excited by another light sheet, retrieving same thickness of the latter also on the other half of the sample. In fact light absorption and scattering is not only happening for the fluorescence signal but also for the excitation light, so that the leftmost part of the planes shown (the part that is facing the light source) is more defined with respect to the rightmost part of the specimen.

To conclude with, a remark on the illumination NA for the two stacks is hereby presented. The acquisition shown in Fig. 4.8 has been performed with a fully illumination NA, giving as a result the smallest Gaussian beam waist possible, $w_0 = \frac{\lambda}{2*NA_{ill}} = 0.7\mu m$, but also a very short Rayleigh length, $z_R = 0.006mm$. On the other hand, the stack in Fig. 4.11 has been acquired following the constraint of a persistence length of the illumination beam equal to half of the optimum value, where $2z_R = 0.4mm$, resulting in a reduced $NA_{ill} = 0.05$, as suggested in 2.3.2.

4.5.2 Axial Resolution

In this section it will be considered the capability of the system to distinguish two close objects in the optical detection axis. The concept of axial resolution of a system has already been presented in section 2.1.4. From eq. 2.24, we have retrieved the axial resolution of the detection system working with a signal at $\lambda = 500nm$; taking into account also the discretization of the sensor, a resolution of about $5\mu m$ is theoretically achieved. To confirm this, samples of Arabidopsis Thaliana are taken into exam. This specimen in fact is well suitable for this

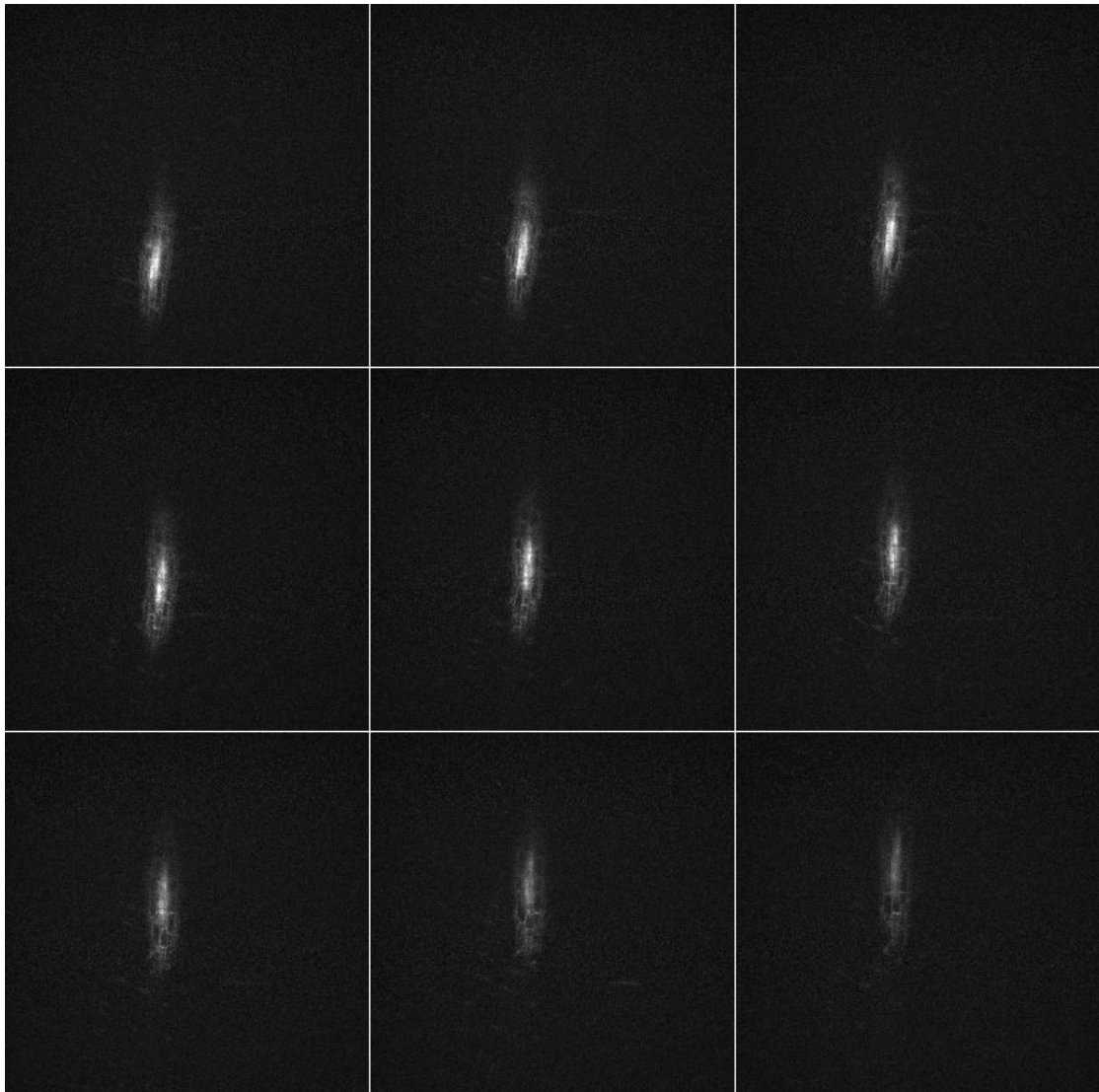


FIGURE 4.14: Image stack of the bust of an Arabidopsis Thaliana. The stack has been made by acquiring 50 planes at the same magnification factor. In this figure are presented 9 equally spaced planes.

kind of analysis since it has been extensively studied with different microscopy approaches such as confocal [31], or light sheet [32]. The main reasons for this interest are that Arabidopsis is highly transparent, radially symmetric, of small size (the root is typically $100 - 150\mu\text{m}$ in diameter) and presents slow growth rate (few millimeters/day) [33].

From the stack in Fig. 4.14, volumetric information is collected thanks to a tool for 3D imaging implemented in ImageJ, an open source image processing program which allow to orthogonally project the lateral scans. The obtained orthogonal view is shown in Fig. 4.15. This image shows how the system is able to distinguish

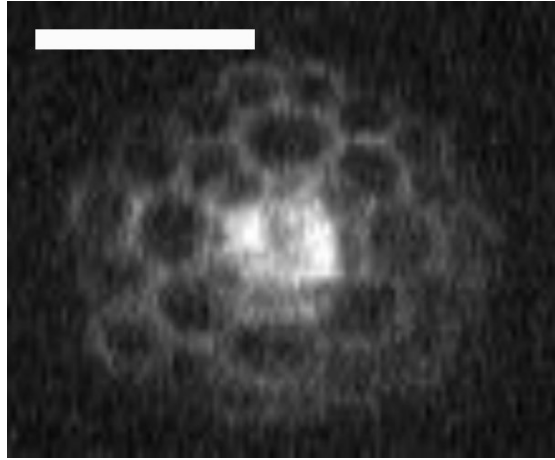


FIGURE 4.15: Orthogonal projection of the bust of an Arabidopsis Thaliana. In the top left corner a white bar scale representing $100\mu m$ is shown.

ETL	Galvanometric Mirror	CCD	Scan
Amplitude=0.43V	Amplitude=0.4V	$t_{exposition} = 0.1s$	f=0.1Hz
Offset=2.7V	waveform=sawtooth	$EMCCD_{gain}=80$	Absolute Phase= 180°

TABLE 4.3: Parameters for the acquisition of the Arabidopsis Thaliana.

between two adjacent cells, whose dimension are known to vary from 10 to 30 μm [34].

As it has already been discussed in the previous paragraph, it emerges that, with the laser beam firstly impinging onto the leftmost part of the sample, the image quality downgrade in the other half of the specimen.

A final remark is made on the acquisition parameter for the stack in 4.14. In table 4.3 it is shown the voltage maximum amplitude with which the motorized mirror is driven, i.e. 0.4V. From sections 2.3.2 and 3.3.2, a voltage signal of 0.4V, with the proper scaling factor ($0.8V/^\circ$) corresponds to an angular displacement of 1° , that is translated by the f-theta system in an axial displacement (with respect to the detection axis) of around $244\mu m$, according to the plant dimension.

4.6 Conclusions

Selective plane illumination microscopy (SPIM) is a microscopy technique that exploits high-resolution fluorescence imaging for in-vivo specimens. The working

principle of SPIM is that of selectively exciting fluorescence onto a thin sheet placed in the focal plane of the detection objective. The benefits of this technique include good optical sectioning, low photodamage effects and improved axial resolution compared with multi- and single-photon confocal microscopy [11].

In the thesis work presented, a complete SPIM setup has been developed, starting from its optical design. After this, thanks to the concepts introduced in the first, theoretical chapter, the characteristics of the setup are calculated, in order to quantify its optical sectioning capability and its lateral and axial resolution. With respect to a standard light sheet microscope, the setup developed performs the scanning of the sample not by mechanical translation of the latter, but through optical and mechanical adaptive elements such as an electro-tunable lens and a galvanometric mirror. These two programmable elements, together with the detection sensor (EMCCD) are controlled thanks to the developed software presented in ch 3, which allows the adaptation the scanning parameters, like scanning speed and amplitude, to the analyzed sample. Finally, tests for magnification invariance and optical stability were made, together with *in vivo* measurements from which they can be inferred the optical sectioning and the resolutions of the system, for a comparison with the theoretical values shown in chapter 2. The setup implemented shows optical properties that are in good agreement with what it has been calculated in chapter 2, confirming excellent sectioning and good axial resolution. On top of that good hints for further improvements of the setup can be inferred from the collected images, that suffer from the inhomogeneous illumination caused by sample absorption and scattering. The first of these improvements could be that of implementing a second, symmetrical illumination path to maintain same light sheet thickness over the two halves of the sample.

Bibliography

- [1] Jerome Mertz. *Introduction to optical microscopy*, volume 138. Roberts, 2010.
- [2] Albert Einstein. On the quantum mechanics of radiation. *Physikalische Zeitschrift*, 18:121–128, 1917.
- [3] Benjamin Fain and Peter W Milonni. Classical stimulated emission. *JOSA B*, 4(1):78–85, 1987.
- [4] Donald A McQuarrie and JDS Physical Chemistry. *A Molecular Approach*. University Science Books: USA, 1997.
- [5] Joseph W Goodman. *Introduction to Fourier optics*. Roberts and Company Publishers, 2005.
- [6] Wade T Cathey. Comparison of single-lens and two-lens coherent imaging of complex distributions. *JOSA*, 56(8):1015–1017, 1966.
- [7] Jan Huisken, Jim Swoger, Filippo Del Bene, Joachim Wittbrodt, and Ernst HK Stelzer. Optical sectioning deep inside live embryos by selective plane illumination microscopy. *Science*, 305(5686):1007–1009, 2004.
- [8] Thomas A Planchon, Liang Gao, Daniel E Milkie, Michael W Davidson, James A Galbraith, Catherine G Galbraith, and Eric Betzig. Rapid three-dimensional isotropic imaging of living cells using bessel beam plane illumination. *Nature methods*, 8(5):417, 2011.
- [9] Alex Costa, Alessia Candeo, Luca Fieramonti, Gianluca Valentini, and Andrea Bassi. Calcium dynamics in root cells of arabidopsis thaliana visualized with selective plane illumination microscopy. *PLoS One*, 8(10):e75646, 2013.

-
- [10] D Kromm, T Thumberger, and J Wittbrodt. An eye on light-sheet microscopy. *Methods in cell biology*, 133:105–123, 2016.
- [11] Christoph J Engelbrecht and Ernst H Stelzer. Resolution enhancement in a light-sheet-based microscope (spim). *Optics letters*, 31(10):1477–1479, 2006.
- [12] Philipp J Keller, Annette D Schmidt, Joachim Wittbrodt, and Ernst HK Stelzer. Reconstruction of zebrafish early embryonic development by scanned light sheet microscopy. *science*, 322(5904):1065–1069, 2008.
- [13] Liang Gao, Lin Shao, Christopher D Higgins, John S Poulton, Mark Peifer, Michael W Davidson, Xufeng Wu, Bob Goldstein, and Eric Betzig. Noninvasive imaging beyond the diffraction limit of 3d dynamics in thickly fluorescent specimens. *Cell*, 151(6):1370–1385, 2012.
- [14] Mike Friedrich, Qiang Gan, Vladimir Ermolayev, and Gregory S Harms. Sted-spim: stimulated emission depletion improves sheet illumination microscopy resolution. *Biophysical journal*, 100(8):L43–L45, 2011.
- [15] Florian O Fahrbach, Fabian F Voigt, Benjamin Schmid, Fritjof Helmchen, and Jan Huisken. Rapid 3d light-sheet microscopy with a tunable lens. *Optics express*, 21(18):21010–21026, 2013.
- [16] Raju Tomer, Matthew Lovett-Barron, Isaac Kauvar, Aaron Andalman, Vanessa M Burns, Sethuraman Sankaran, Logan Grosenick, Michael Broxton, Samuel Yang, and Karl Deisseroth. Sped light sheet microscopy: fast mapping of biological system structure and function. *Cell*, 163(7):1796–1806, 2015.
- [17] Edward D Huber. Bright field illumination system, October 20 1998. US Patent 5,825,495.
- [18] Max Born and Emil Wolf. *Principles of optics: electromagnetic theory of propagation, interference and diffraction of light*. Elsevier, 2013.
- [19] Jan Huisken and Didier YR Stainier. Selective plane illumination microscopy techniques in developmental biology. *Development*, 136(12):1963–1975, 2009.

- [20] Paul J Scherz, Jan Huisken, Pankaj Sahai-Hernandez, and Didier YR Stainier. High-speed imaging of developing heart valves reveals interplay of morphogenesis and function. *Development*, 135(6):1179–1187, 2008.
- [21] Johnathon R Walls, John G Sled, James Sharpe, and R Mark Henkelman. Resolution improvement in emission optical projection tomography. *Physics in medicine and biology*, 52(10):2775, 2007.
- [22] Mark A Rizzo, Gerald H Springer, Butch Granada, and David W Piston. An improved cyan fluorescent protein variant useful for fret. *Nature biotechnology*, 22(4):445–449, 2004.
- [23] Martin Chalfie. Green fluorescent protein. *Photochemistry and photobiology*, 62(4):651–656, 1995.
- [24] Frank L Pedrotti and Leno S Pedrotti. Introduction to optics 2nd edition. *Introduction to Optics 2nd Edition by Frank L. Pedrotti, SJ, Leno S. Pedrotti New Jersey: Prentice Hall, 1993*, 1993.
- [25] Daniel H Morse, Arlyn J Antolak, Graham S Bench, and Mark L Roberts. A flexible labviewTM-based data acquisition and analysis system for scanning microscopy. *Nuclear Instruments and Methods in Physics Research Section B: Beam Interactions with Materials and Atoms*, 158(1):146–152, 1999.
- [26] Jeffrey Travis and Jim Kring. *LabVIEW for everyone: graphical programming made easy and fun*. Prentice-Hall, 2007.
- [27] David Harris and Sarah Harris. *Digital design and computer architecture*. Morgan Kaufmann, 2010.
- [28] Deborah E Bryant and Audrey F Harvey. Daq configuration system and method for configuring channels in a data acquisition device, June 9 1998. US Patent 5,764,546.
- [29] Abdul J Jerri. The shannon sampling theorem—its various extensions and applications: A tutorial review. *Proceedings of the IEEE*, 65(11):1565–1596, 1977.

-
- [30] Katherine Luby-Phelps. Cytoarchitecture and physical properties of cytoplasm: volume, viscosity, diffusion, intracellular surface area. *International review of cytology*, 192:189–221, 1999.
- [31] Kay Schneitz, Martin Hülskamp, and Robert E Pruitt. Wild-type ovule development in arabidopsis thaliana: a light microscope study of cleared whole-mount tissue. *The Plant Journal*, 7(5):731–749, 1995.
- [32] Giovanni Sena, Zak Frentz, Kenneth D Birnbaum, and Stanislas Leibler. Quantitation of cellular dynamics in growing arabidopsis roots with light sheet microscopy. *PLoS One*, 6(6):e21303, 2011.
- [33] WA Rensink and C Robin Buell. Arabidopsis to rice. applying knowledge from a weed to enhance our understanding of a crop species. *Plant Physiology*, 135(2):622–629, 2004.
- [34] Gerrit TS Beemster, Kristof De Vusser, Evelien De Tavernier, Kirsten De Bock, and Dirk Inzé. Variation in growth rate between arabidopsis ecotypes is correlated with cell division and a-type cyclin-dependent kinase activity. *Plant Physiology*, 129(2):854–864, 2002.